DEVELOPMENT OF ADVANCED PHOTOCATALYSIS AND MEMBRANES FOR WASTEWATER TREATMENT

A Dissertation

by

WEI DENG

Submitted to the Office of Graduate and Professional Studies of
Texas A&M University
in partial fulfillment of the requirements for the degree of

DOCTOR OF PHILOSOPHY

Chair of Committee,	Ying Li
Co-Chair of Committee,	Xingmao Ma
Committee Members,	Choongho Yu
	Matt Pharr
Head of Department,	Andreas A. Polycarpou

August 2019

Major Subject: Mechanical Engineering

ABSTRACT

Inadequate access to clean water is a pressing problem across the world, which calls out enormous research efforts to develop efficient and economic solutions to the safe reuse of wastewater. In this dissertation, heterogeneous photocatalysis, superwetting membranes, and photocatalytic superwetting membranes have been studied for the removing organic pollutants, separating immiscible oil/water mixtures, and treating of oil/water emulsions, respectively. Specifically, four research works are included. (1) A sulfite-promoted photodegradation process was developed. It was found that the degradation rate of methyl orange (MO) could be greatly enhanced by sulfite and scavenging study suggested that sulfite radicals generated by the reactions of sulfite with holes or hydroxyl radicals were the reactive species. The developed approach was demonstrated as a general approach as it was successfully applied to various pollutants and photocatalysts. (2) To evaluate the adsorption-photocatalysis synergy, mesoporous TiO_2 (amorphous)-BiOBr microspheres were facilely synthesized as the model photocatalysts. Homogeneously distributed TiO_2 in BiOBr microplates tailored the crystallite size of BiOBr, and consequently surface area (22 to 155 m^2/g) and adsorption capacity (16 to 54 mg/g of MO) of the composites. Developed kinetic modeling that combined adsorption with photocatalysis aided elucidating the synergy and quantitatively evaluating the composites. Though high adsorption promoted MO photodegradation, we found adverse effects on photocatalysis that could be caused by high levels of MO adsorption as revealed by cycling tests. (3) Uniform and smooth TiO_2 films were conformally coated on stainless steel mesh (SSM) via a biomineralization approach that is environmentally benign, facile, and scalable. The TiO_2-coating made the meshes superhydrophilic and underwater superoleophobic. The coated meshes could separate immiscible oil/water mixtures solely driven by gravity with high flux (~3×10^4 $Lm^{-2}h^{-1}$), high separation efficiency (~ 99.999%),

and excellent anti-fouling capability. The meshes also had great chemical, mechanical and thermal durability. (4) Photocatalytic and superhydrophilic PVDF-BiOBr composite membranes were fabricated by a facile and scalable phase-inversion method. The composite membranes showed photocatalysis-enhanced anti-fouling capability for treating oil/water emulsions. In summary, rational engineering of the photocatalytic reactions, photocatalysts, and membrane surface wettability were studied and could help advance the development of photocatalysis and membrane technology in wastewater treatment.

DEDICATION

To my dearest parents and my sister, your support and encouragement have been inspiring me to pursue my dreams.

To my cute nephews, your innocence and smile always cheer me up.

To my lovely girlfriend, Di Sun, you've been making this journey full of joy.

ACKNOWLEDGEMENTS

I would like to thank my committee chair, Dr. Ying Li. He gave me the opportunity and support to conduct this research work at Texas A&M University. I want to thank him for giving me a lot of valuable suggestions and helping me with my career planning.

I would like to thank D.Xingmao Ma for being my committee co-chair. I would also like to thank my committee members, Dr. Matt Pharr and Dr. Choongho Yu, for their guidance and support throughout the course of this research. I want to thank Dr. Bill Batchelor for giving me a lot of great suggestions and comments for my manuscripts. I also want to thank. Ahmed Abdel-Wahab and Dr. Hongcai Zhou.

I want to thank my colleague Dr. Huilei Zhao, Dr. Fuping Pan, and Dr. Guiying Rao for giving me great suggestions on writing and design of experiments. I want to thank my colleagues Dr. Chao Li and Xuhui Feng for helping me with my experiments. I want to thank Dr. Peng Zhang and Dr. Bahngmi Jung for the collaborations. I also want to thank Dr. Xianmei Xiang, Tianzhu Fan, Yang Gang, Zichen Du, Chongjie Gao, Tyler Scott, and the department faculty and staff for making my time at Texas A&M University a great experience.

CONTRIBUTORS AND FUNDING SOURCES

Contributors

This work was supervised by a dissertation committee consisting of Professor Ying Li (advisor), Professor Matt Pharr and Professor Choongho Yu of the Department of Mechanical Engineering and Professor Xingmao Ma of the Department of Civil Engineering.

The kinetic modeling in Chapter 4 was developed by Professor Bill Batchelor. The TEM analyses and photoluminescence spectra depicted in Chapter 4, as well as the Tafel polarization plots in Chapter 5 were conducted with help from Dr. Fuping Pan. The N_2 adsorption-desorption analyses in Chapter 3 and 4 were conducted by Dr. Peng Zhang.

All other work conducted for the dissertation was completed by the student independently.

Funding Sources

This work was also made possible by the Qatar National Research Fund under its National Priorities Research Program (award number NPRP 8-1406-2-605) and funding from Texas A&M Energy Institute. Its contents are solely the responsibility of the authors and do not necessarily represent the official views of the Qatar National Research Fund or Texas A&M Energy Institute. The use of the Texas A&M University Materials Characterization Facility is also acknowledged.

NOMENCLATURE

BiOBr	Bismuth Oxybromide
BiOCl	Bismuth Oxychloride
BiOI	Bismuth Oxyiodide
Bi_2O_3	Bismuth Oxide
P25	A commercially available TiO_2 nanopowder
PEI	Polyethylenimine
PVDF	Polyvinylidene Fluoride
SSM	Stainless Steel Mesh
Ti-BALDH	Titanium(IV)bis(ammonium lactato)dihydroxide
TiO_2	Titanium Dioxide
TSSM	TiO_2-Coated Stainless Steel Mesh

TABLE OF CONTENTS

Page

LIST OF FIGURES

Page

LIST OF TABLES

Page

CHAPTER 1

INTRODUCTION AND LITERATURE REVIEW[1]

1.1 Water scarcity and wastewater treatment

Inadequate access to clean water is becoming one of the most prevalent problems that beset people throughout the world and threaten the sustainable development of human society. In the annual risk report of 2015, the World Economic Forum has listed water crises as the largest global risk in terms of potential impact.[1] Nearly a third of the global population (~2 billion people) lived under conditions of severe scarcity of clean drinking water at least 1 month of the year during 2015.[2] Moreover, countless people died and were sickened from diseases and contaminations associated with unsafe drinking water.[3-5] In addition, water scarcity occurring globally also strongly affects industry and agriculture that produce essential products to improve the quality of human being lives, because in many processes, like food and beverage manufacturing, as well as microchip fabrication, high-purity water is a crucial prerequisite (Figure 1).[6]

Safe reuse of wastewater can provide clean water supply and mitigate the water scarcity problem because tremendous amounts of wastewater has been generated from industries, such as the production of textile, petrochemicals and oil/gas (Figure 1). Wastewater also comes from municipal usage, natural disasters and accidents-caused oil spills and chemicals leakage, as well

[1] Part of this chapter is reprinted with permission from "Visible-light-driven photocatalytic degradation of organic water pollutants promoted by sulfite addition" by Deng, Wei, Huilei Zhao, Fuping Pan, Xuhui Feng, Bahngmi Jung, Ahmed Abdel-Wahab, Bill Batchelor, and Ying Li, 2017. Environmental science & technology 51(22), 13372-13379. Part of this chapter is also reprinted with permission from from "Mesoporous TiO2–BiOBr microspheres with tailorable adsorption capacities for photodegradation of organic water pollutants: probing adsorption–photocatalysis synergy by combining experiments and kinetic modeling" by Deng, Wei, Fuping Pan, Bill Batchelor, Bahngmi Jung, Peng Zhang, Ahmed Abdel-Wahab, Hongcai Zhou, and Ying Li, 2019. Environmental Science: Water Research & Technology, 5, 769-781. Copyright [2019] by Royal Society of Chemistry.

as pesticides-polluted water in agriculture. Due to the increasing industry development and population growth, water problems are expected to get worse in the coming decades, along with the increasing production of wastewater. This makes scientific research and technology development of advanced water treatment methods indispensable to increase water supplies through the safe reuse of wastewater. It should be noted that clean water in this context is defined as water of quality that meets the requirements for the desired applications while wastewater does not.

The composition of wastewater is complex and could vary significantly depending on the source of the pollutants. Typically, the pollutants in wastewater range from pathogens to trace chemicals and salts, as shown in Figure 2, including but are not limited to: pathogenic microorganisms, suspended and dissolved solids, heavy metals, oils, foulants, anions, pesticides, organic compounds (dyes, volatile organic compounds (VOCs), pharmaceuticals, personal care products (PCPs)), and salts. [7] To achieve the removal of multiple pollutants, different processes are required because of their different physicochemical properties. The treatment level generally increases with institutional and socioeconomic capacity. Basic treatment often uses coagulation/precipitation/flotation to remove colloidal and other suspended matter, followed by chemical or UV/Ozone disinfection. High level treatment methods relies on more advanced technologies, such as adsorption, membrane filtration, and catalytic oxidation, to remove carcinogenic and endocrine disrupting chemicals that are resistant to traditional treatment processes, as well as other contaminants including VOCs, PCPs and cyanotoxins.[7]

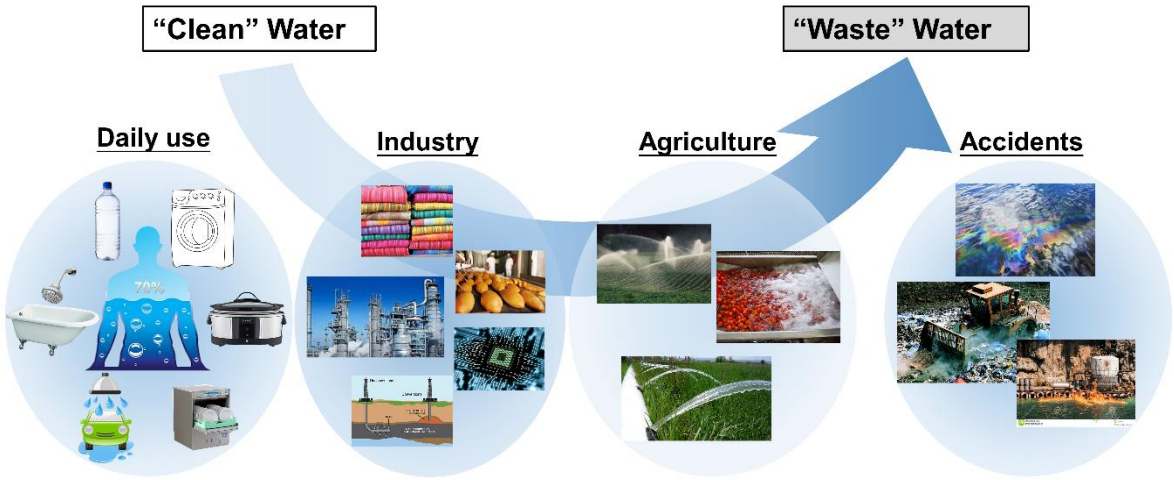

Figure 1. Water usage and pathways of "waste" water generation.

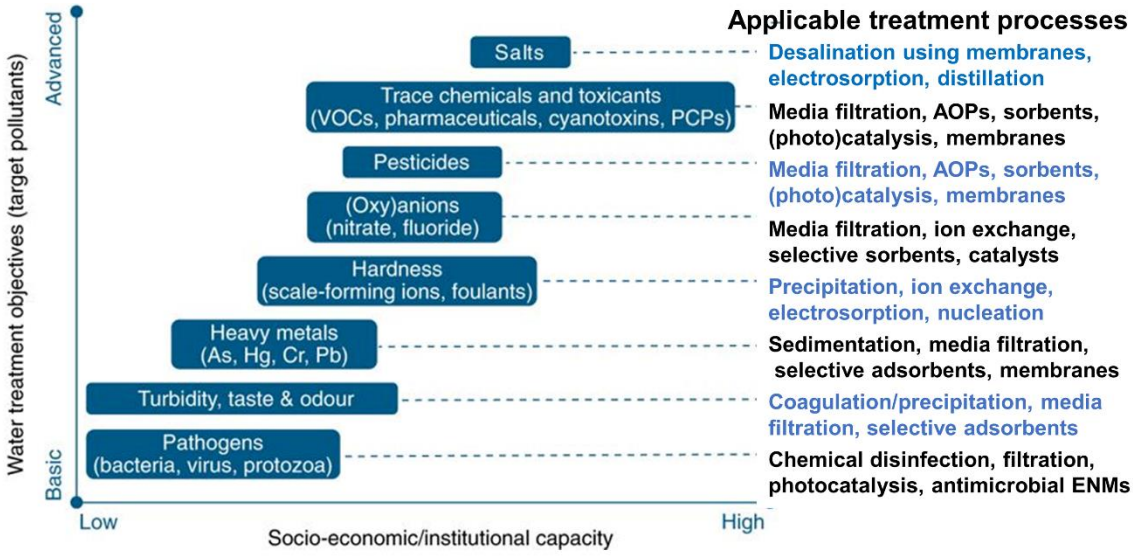

Figure 2. Water treatment priorities and processes. Adapted from Ref [7] with permission.

The complex nature of wastewater requires the integration of multiple processes, which also explores the synergistic effects to overcome certain inherent limitations of single treatment methods. For example, filtration membranes suffer from severe fouling caused by organic

pollutants, which can be readily remedied by advanced oxidation processes (AOPs). Meanwhile, guided by the "fit-for purpose" strategy, it should be target-oriented when choosing the treatment methods for multiple-process systems, so that to ensure the removal of the target constituents but not waste the treatment capacity on non-problematic constituents, which is conducive to lower treatment costs. [7] In the scope of this dissertation, my research study focuses on the removal of organic pollutants, like dyes and phenol, and oils, using photocatalysis and superwetting membranes. Detailed background introduction and literature review on the studied research fields will be given in the following sections.

1.2 Photocatalytic Degradation of Organic Pollutants in Wastewater

Many organic pollutants can cause chronic toxicity, ranging from disruption of fertility to cancer. For example, azo-dyes such as methyl orange (MO) are highly mutagenic and carcinogenic.[8] Moreover, organic pollutants can cause severe fouling on membranes that are used in filtration and desalination processes. Therefore, removal of organic pollutants from wastewater is highly demanded. Currently well-developed techniques for organic pollutants removal include adsorption,[9] biodegradation,[10] chlorination,[11] Fenton reaction,[12] ozonation,[13] combined coagulation/flocculation using sludge,[14] and electrochemical oxidation.[15] However, these techniques suffer from high input demands of chemicals and energy, as well as the generation of undesirable by-products that may cause secondary-pollutions. Consequently, research efforts are in great need to develop techniques that can achieve destruction of organic pollutants at lower cost and with less energy, while at the same time minimizing the use of chemicals and impact on the environment.

Heterogeneous photocatalysis is a promising process for wastewater remediation. Since the photocatalytic process can be solely driven by light, the availability of free and inexhaustible solar energy endows this technique with great potential as a low-cost, environment-friendly and sustainable treatment technology. The fundamental of photocatalysis lies on the production of reactive species on photocatalyst surface upon absorbing photon energy (Figure 3). These reactive species, such as electron-hole pairs, superoxide radicals and hydroxyl radicals, have reductive or oxidative capability and can degrade organic pollutants in the solution phase and adsorbed phase. Through multiple degradation pathways, the pollutants are converted to intermediates and finally innocuous CO_2, H_2O and other products.

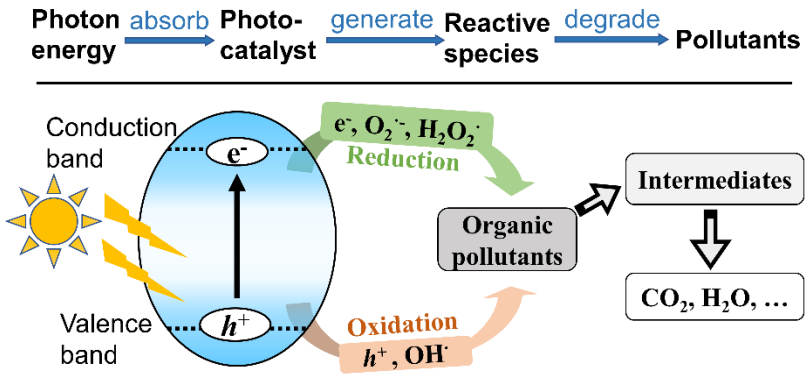

Figure 3. Schematic illustration of the heterogeneous photodegradation process.

As the model photocatalysis system, TiO_2/UV has been extensively studied for removing various organic compounds in water.[16] The successful demonstration of this model system stimulated great research efforts on photocatalytic water treatment. Current research on subject mainly focuses on the following five directions (Figure 4). First, researchers are devoted to developing new photocatalysts, visible-light-responsive TiO_2-based photocatalysts[17],

heterostructured photocatalysts with facilitated charge separation and improved degradation efficiency,[18] and novel photoactive materials.[19-21] The second direction emphasizes the synergistic benefits of integrating photocatalytic reactions with other treatment methods. For example, photo-assisted Fenton process,[22] electrochemically assisted photocatalysis,[23] integration of photocatalysis and membrane distillation,[24] and coupled photocatalysis-ozonation[25] have been studied. The third direction focuses on the development of innovative photocatalytic membrane reactors to avoid post-separation of the photocatalysts from the treated water but also achieve high efficiency.[26, 27] The fourth direction aims to demonstrate the feasibility of applying photocatalysis in the treatment of real wastewater.[28-30] Fundamental studies on the underlying mechanisms associated with the photodegradation process are also necessary. These studies include reactive species generation,[31, 32] adsorption-catalysis synergy,[33, 34] band structure engineering,[35] electron-hole separation,[36] degradation pathways,[37, 38] and reaction conditions.[39] These mechanism studies helped understand the photodegradation process and advance the design of photocatalysts and reactors. My research in this direction focuses on the first two, that are, manipulating reactive species and studying adsorption-photocatalysis synergy. More in-depth introduction will be given in Chapter 3.

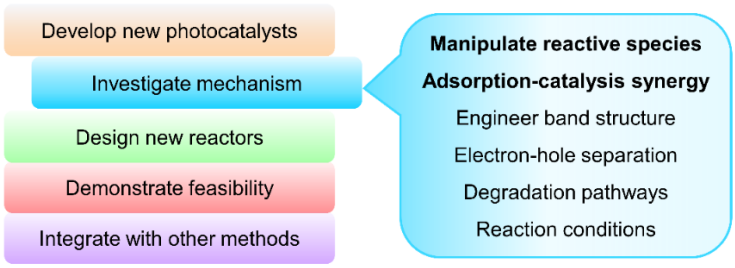

Figure 4. Focused research directions of photocatalysis for water treatment and areas of mechanism investigation.

1.3 Membrane with Special Wettability for Oil/water Separation

Oil is a widely existed pollutant in wastewater, especially in oil/gas production industry and oil spilled areas. Oil is also a type of organic pollutants, but separation is a more fitting approach than destruction to treat oily wastewater. This is because oils can be collected as chemicals for further use and separation is usually faster and less challenging than destruction. Hence, water separation accounts for an important step of water treatment. Membrane technology is attractive for oil/water separation as it works without chemicals addition, with low energy requirement and undemanding operations and it can achieve high separation efficiency and speed if the wettability of the membranes is well designed.[40] Typically, surfaces of membranes for oil/water separation are categorized to two types: hydrophilic/oleophobic surfaces that are permeable to water but impervious to oils (Figure 5), and oleophilic/hydrophobic surfaces that are permeable to oils but impervious to water. By achieving an appropriate combination of surface energy and surface roughness, desirable surface wettability can be procured.[41] Therefore, surface modification of membranes is deemed a fundamental but powerful approach to engineer surface wettability of membranes.[42]

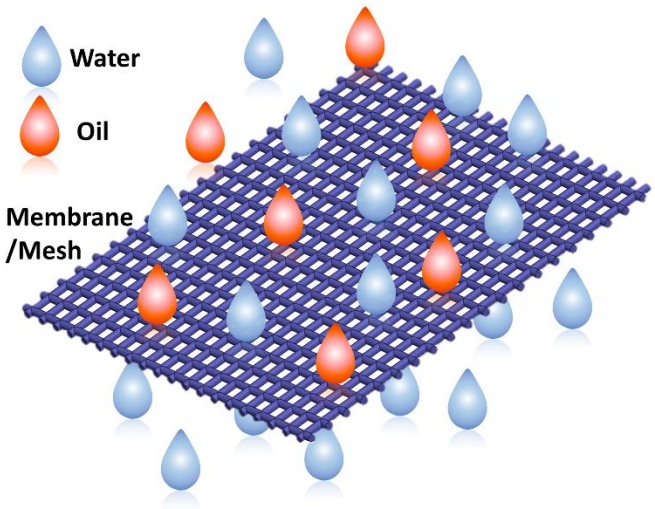

Figure 5. Schematic illustration of oil/water separation using hydrophilic and oleophobic membrane/mesh.

Applying coatings on porous membranes are widely used to modify the membrane surfaces. Stainless steel mesh (SSM), as a porous metallic membrane, is genuinely promising for oil/water separation upon coated with suitable surface materials, because SSM is low-cost, robust, flexible, and resistant to mechanical wear and chemical corrosion. A wide range of materials have been studied as coating materials on SSM to engineer the surface wettability,[43-62] however, these reported surface coatings require complex coating procedures or precursor preparation processes. Therefore, considering the massive amount of oily wastewater and its complex compositions and properties, the coating methods should be simple, facile, inexpensive and scalable, meanwhile, the coating materials should be durable to preserve surface wettability under harsh conditions with chemical corrosion and mechanical wear. Research on coating materials and methods are still in great need to fulfil these goals.

1.4 Photocatalytic-Superwetting Membranes for Oil/Water Emulsions Treatment

Comparing immiscible oil/water mixtures, emulsions are more challenging to treat, mainly because the small size of oil droplets requires the membranes with smaller pore size at a cost of flux reduction. In addition, oil-fouling occurs during separating oil/water emulsions even though the membranes are superoleophobic. This is because oil droplets are "soft-particles" that maybe mechanically trapped in the pores. Polymer membranes (such as PVDF) with high porosity and obtainable small pore size are suitable for treating oil/water emulsions. Moreover, polymer membranes have relatively good mechanical and chemical durability and are available for large scale fabrication. Nevertheless, pristine PVDF membranes are usually hydrophobic and have to be modified to achieve superhydrophilicity and oleophobicity. In addition, ways to mitigating oil-fouling on membranes are also necessary to enable long-term use without additional cleaning/recovery actions.

CHAPTER 2

MATERIAL CHARACTERIZATION TECHNIQUES

This chapter summarizes the material characterization techniques used in this dissertation.

X-ray diffraction (XRD) was performed on a D8 Advance diffractometer (Bruker-AXS, Karlsruhe, Germany) using Cu Kα irradiation at 40 kV and 40 mA. XRD patterns from 10° to 80° 2θ were recorded at room temperature. The step increment was set as 0.05° 2θ and the counting time per step was 1s. The surface morphology was obtained by an ultra-high resolution field-emission scanning electron microscope (FE-SEM, JEOL JSM7500F, Japan) equipped with a cold cathode UHV field emission conical anode gun. Fourier-transform infrared spectroscopy (FTIR) was performed on a Nicolet iS50 FT-IR spectrometer (Thermo Scientific) equipped with a liquid nitrogen cooled HgCdTe detector. UV–vis diffuse reflectance spectra were measured on a Hitachi U4100 UV–vis-NIR Spectrophotometer (Japan) with Praying Mantis accessory. Micromeritics ASAP 2420 physisorption analyzer was used to determine the Brunauer–Emmett–Teller (BET) surface area at liquid nitrogen temperature (77.3 K). Prior to measurement, the BiOBr powder was degassed in vacuum at 100 °C for 12 hr. X-ray photoelectron spectroscopy (XPS) was performed using Omicron's DAR 400 with Mg X-ray source. Tafel polarization curves were obtained on a three-electrode electrochemical cell. A Pt flake and an Ag/AgCl (3 M KCl) were used as the counter electrode and reference electrode. A 0.6 M NaCl aqueous solution was used as electrolyte and corrosion medium. Prior to each electrochemical test, the SSM and TSSM (14 mm ×14 mm) samples were immersed in a corrosive medium (0.6 M NaCl aqueous solution) for 30 min to obtain a steady electrochemical state. The sweep rate of the potential was 2 mV s−1. The concentrations of MO and RhB were analyzed on a UV−Vis spectrophotometer (UV-2600, Shimadzu) at the wavelengths of 464 nm and 554 nm. The concentration of phenol was measured by a high-pressure

liquid chromatography (HPLC-2030C, Shimadzu) equipped with a reversed phase C18 column (Kinetex, model# 00F-4601-E0). A mixture of acetonitrile and deionized water, flowing at a rate of 1.0 mL/min, was used as the mobile phase.

CHAPTER 3

SULFITE-PROMOTED PHOTODEGRADATION OF ORGANIC WATER POLLUTANTS[2]

3.1 Background and Hypothesis

Photo-induced electron-hole pairs can readily react with oxygen and water to produce superoxide radicals and hydroxyl radicals. With suitable redox potentials, other compounds can also react with electron-hole pairs and produce corresponding reactive species, so providing such compounds provides a way to manipulating reactive species involved in photocatalysis and possibly enhancing contaminant degradation. Based on this strategy, several chemicals have been reported to be able to help generate reactive species and enhance photodegradation efficiency. Emad et al. reported that the addition of H_2O_2 could promote the production of hydroxyl radicals and consequently the photocatalytic degradation of antibiotics by the TiO_2/UV system.[63] Hazime et al. found that $K_2S_2O_8$ could also help generate hydroxyl radicals and degrade imazalil by UV-illuminated TiO_2 nanoparticles.[32] However, the addition of H_2O_2 and $K_2S_2O_8$ led cost increase, which stimulates the research to explore other low-cost chemicals that can enhance photodegradation efficiency. The sulfite radical is an example of an active species that possess reducing and oxidizing capabilities which can be applied to effectively degrade organics such as phenol, chlorpromazine, olefin, and polyunsaturated fatty acid.[64-68] Sulfite radicals are usually created upon the photolysis of sulfite anions under middle UV light or via sulfite anions reacting

[2] Part of this chapter is reprinted with permission from "Visible-light-driven photocatalytic degradation of organic water pollutants promoted by sulfite addition" by Deng, Wei, Huilei Zhao, Fuping Pan, Xuhui Feng, Bahngmi Jung, Ahmed Abdel-Wahab, Bill Batchelor, and Ying Li, 2017. Environmental science & technology 51(22), 13372-13379. Part of this chapter is also reprinted with permission from "Response to Comment on “Visible-Light-Driven Photocatalytic Degradation of Organic Water Pollutants Promoted by Sulfite Addition" by Deng, Wei, Huilei Zhao, Fuping Pan, Xuhui Feng, Bahngmi Jung, Ahmed Abdel-Wahab, Bill Batchelor, and Ying Li, 2018. Environmental science & technology 52(3), 1677-1678. Copyright [2019] by American Chemical Society.

with transition metal ions and other radicals like hydroxyl radicals.[69-72] Since sulfur dioxide is a major air pollutant and sulfite is a product from flue-gas desulfurization process, it is an attractive idea to convert sulfite waste into useful sulfite radicals through a photocatalytic process and to enhance photodegradation of organic water pollutants (Figure 6a).[73, 74]

3.2 Experiment Details

BiOBr microspheres were synthesized through a facile method at room temperature.[75] Typically, bismuth nitrate (3 mmol, 1.47 g) was dissolved in a mixed solution of deionized water (8.5 mL) and acetic acid (4.5 mL), followed by 15 min magnetic stirring to obtain a clear and transparent solution. Then KBr solution (3 mmol, 0.357 g in 10 mL deionized water) was added into the above solution under rigorous stirring and the mixture was stirred for another 30 min to ensure complete precipitation. The precipitate was collected by centrifuging and washed thoroughly with ethanol and deionized water for six times. The final product was dried at 80 °C in a vacuum furnace overnight. BiOI was synthesized using the same manner described above with KI as the iodine source. Bi_2O_3 was obtained by annealing the synthesized BiOBr sample in air at 550 °C for 2 hr.

Sodium sulfite (Na_2SO_3) was used as the sulfite source. Various target organics and photocatalyst were investigated to demonstrate the versatility of the developed approach: tested target organics included Methyl orange (MO), Rhodamine B (RhB) and phenol; tested photocatalysts included bismuth oxybromide (BiOBr), bismuth oxyiodide (BiOI), bismuth oxide (Bi_2O_3), and commercial titanium oxide (P25). Visible light ($\lambda \geqslant 400$ nm) was used for BiOBr, BiOI, and Bi_2O_3, and simulated sunlight for P25. The experimental setup is illustrated in Figure

6b, where a suspension of photocatalyst, sodium sulfite and organic pollutants is illuminated and stirred. For every certain time, the concentration of the pollutant in the suspension is measured to obtain the time-resolved concentration change of pollutants under illumination measured. Batches of experiments with varied sulfite doses, different photocatalysts and pollutants were conducted to investigate the effects of sulfite dose and demonstrate the versatility of the sulfite-promoted photodegradation.

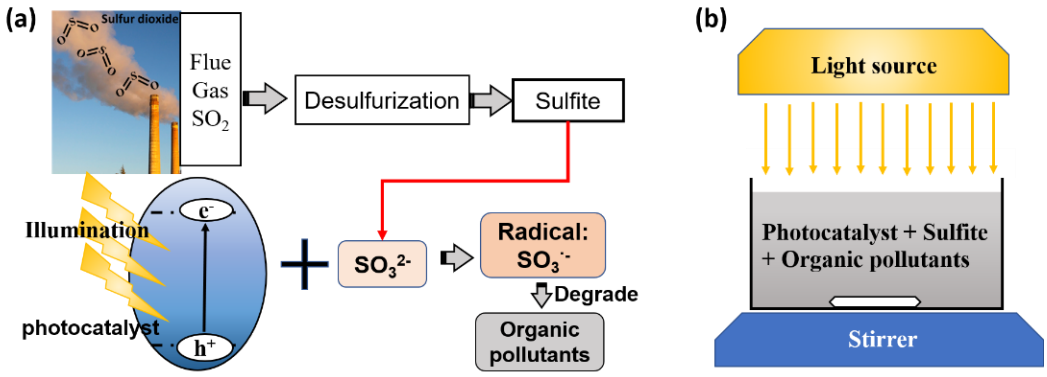

Figure 6. Schematic diagram of (a) introducing sulfite into photodegradation to simultaneous treatment air pollutant (sulfur dioxide) and water organic pollutants, (b) laboratory setup for proof-of-concept studies.

3.3 Characterization Results of the Photocatalyst: BiOBr

The main photocatalyst used in this study is BiOBr. The XRD pattern of the prepared BiOBr sample is shown in Figure 7a, which indicates high crystallinity of the sample with diffraction peaks well indexed to the tetragonal structure of BiOBr (JCPDS File No. 73-2061).[76] The bandgap is estimated to be 2.82 eV from the inset in Figure 7b, and the calcuated conduction band and valence band positions are 0.27 V and 3.09 V vs NHE, respectively. The morphology of

the prepared BiOBr sample is shown in Figure 7c and d. The BiOBr sample has a 3D hierarchical micro-spherical structure with an average diameter of 6 µm and it is constructed by densely stacked thin microplates originating from the layered structure of the bismuth oxyhalide. The microspheres are interconnected to form larger aggregates, which make them easy to collect after water treatment due to their large sizes. The space between the microplates within the microspheres can promote light trapping and thus enhance the photocatalytic performance.[77] In addition, N_2 adsorption-desorption analysis shows that BiOBr has a H3 type hysteresis loop that is typically shown by aggregates of plate-like particles, according to the IUPAC classification.[78] The BET surface area of the BiOBr sample is calculated to be 4.71 m^2/g (Figure 8).

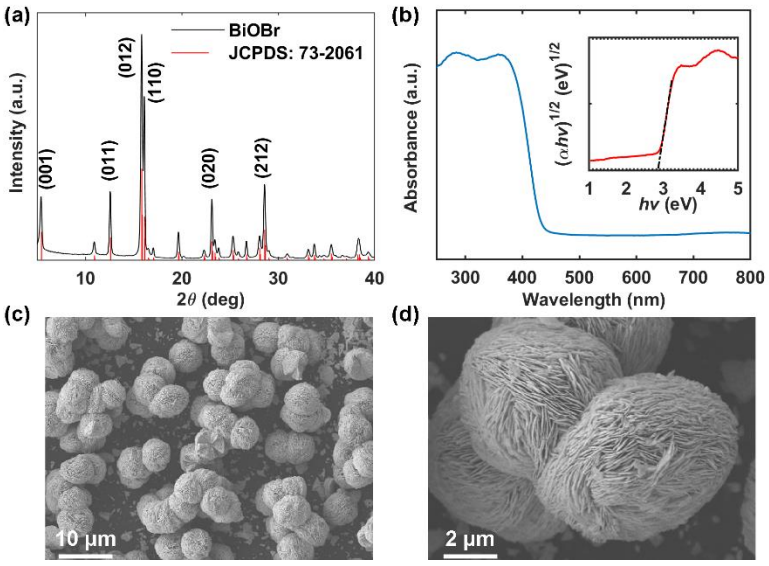

Figure 7. (a) XRD patterns, (b) UV-vis diffuse reflectance (the inset gives the band gap that is 2.82eV) and (c, d) SEM images of the synthesized BiOBr microspheres.

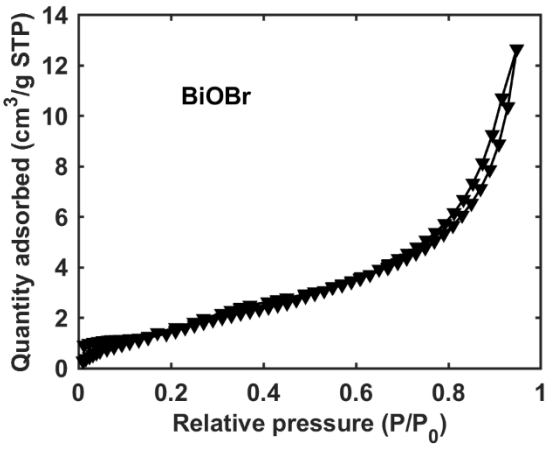

Figure 8. Nitrogen adsorption–desorption isotherms of the BiOBr sample.

3.4 Photocatalytic Degradation of Organic Pollutants Assisted by Sulfite

The photodegradation of MO under visible light was used as a probe to evaluate the performance of BiOBr microspheres and the enhancement brought by sulfite (Figure 9). In the absence of sulfite, only 25% of MO was degraded by BiOBr under visible light irradiation for 30 min, while 70% removal was achieved with the addition of 5 mM sulfite (Figure 9a). The enhancement was more evident at high sulfite concentrations, where 90% and 96% removals were observed with 10 mM and 20 mM sulfite, respectively. Since 10 mM sulfite alone without catalyst yielded negligible degradation of MO, it is confirmed that sulfite participated in the photocatalytic degradation process. The apparent pseudo-first-order rate constants were calculated by regression using a linearized, first-order decay model ($-\ln(C/C_0) = kt$, Figure 9b), where C_0 is the initial concentration of MO, *C* is the concentration after irradiation for a certain time *t*, and *k* is the rate constant. As displayed in Figure 9c, the rate constant increased by about 10, 20, and 29 times upon the addition of 5, 10, and 20 mM sulfite, respectively. The improvement greatly depended on the

concentration of sulfite, implying that the increase in the rate constant should be ascribed to sulfite. It was noted that the rate constant increased linearly with the sulfite concentration when sulfite was less than 10 mM but the rate of improvement was less prominent at a higher sulfite concentration, implying that the rate of production of photo-induced electrons and holes is the rate limiting factor at high sulfite concentrations. As shown in Figure 9d, rapid decrease at the wavelength of 464 nm was achieved in the UV-vis absorption band of MO solution under visible light in the presence of BiOBr and 10 mM sulfite. Neither a shift of the absorption band nor an emergence of new absorption band was observed, indicating that MO was degraded and no other chromophoric molecules were produced. Besides high photoactivity, long term durability of the photocatalyst is also required for practical water treatment applications. Figure 10 indicates that there was no significant change in degradation efficiency after four cycles, demonstrating that BiOBr has high stability in the developed sulfite-assisted photocatalytic process.

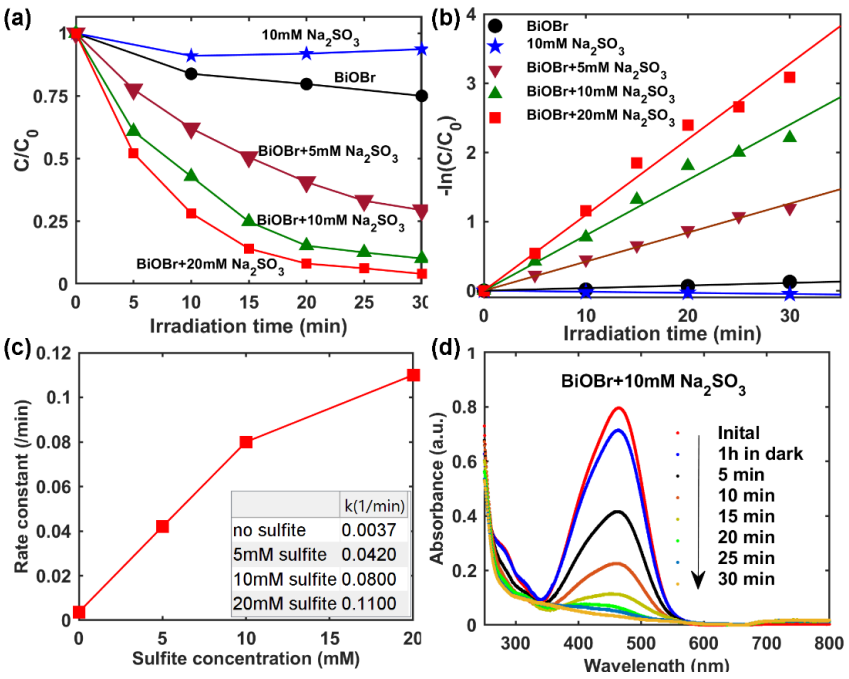

Figure 9. (a) Photocatalytic activities of BiOBr for the degradation of MO under visible light with/without Na_2SO_3, and (b) kinetic fitting. (c) The dependence of MO degradation rate constant on sulfite concentration. (d) Time resolved UV-vis absorption of MO solution under visible light with BiOBr and 10 mM Na_2SO_3. The initial concentration of MO was 10 ppm and the loading of BiOBr was 0.5 g/L.

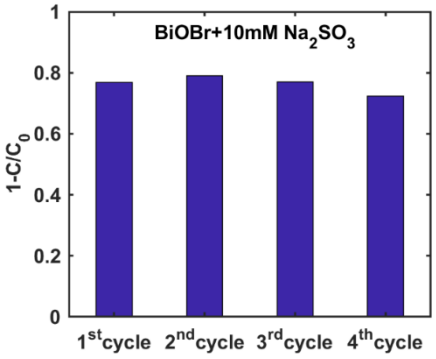

Figure 10. Cycling test of BiOBr for the degradation of 10 ppm MO under visible light with 0.5 g/L BiOBr and 10 mM Na_2SO_3. Irradiation time for each cycle was 15 min.

In addition to MO, RhB and phenol were also tested as target compounds to generalize the effect of sulfite on photocatalysis by BiOBr. In the absence of sulfite, the degradation of RhB was relatively slow (Figure 11a) and the gradual blue shifts of the absorption band were attributed to the removal of ethyl groups.[79] After 30 min irradiation, RhB molecules were fully de-ethylated to the core structure of rhodamine and a new absorption band at 506 nm appeared.[79] Interestingly, in the presence of 10 mM sulfite (Figure 11b), the absorption band of RhB at 554 nm decreased without a blue shift, implying a direct destruction of the core rhodamine structure. However, the addition of sulfite didn't improve the mineralization of RhB (Figure 11c), rather, sulfite might scavenge holes and hydroxyl radicals that are believed to be essential of mineralization.[79] This implies that the developed approach functions as an efficient method for decolorization of wastewater. Further study on the approach may offer improvement in terms of mineralization. The photodegradation of phenol, a persistent water pollutant, was also examined to confirm the function of sulfite. The degradation of phenol was also studied, and the results show that without sulfite there was only 5% photodegradation of phenol, while the addition of 20 mM sulfite resulted in 78% photodegradation after visible light irradiation for 30 min (Figure 12a). All these results on MO, RhB, and phenol degradation show that adding sulfite is a powerful approach that can significantly enhance visible-light-driven photocatalysis using BiOBr as the model catalyst.

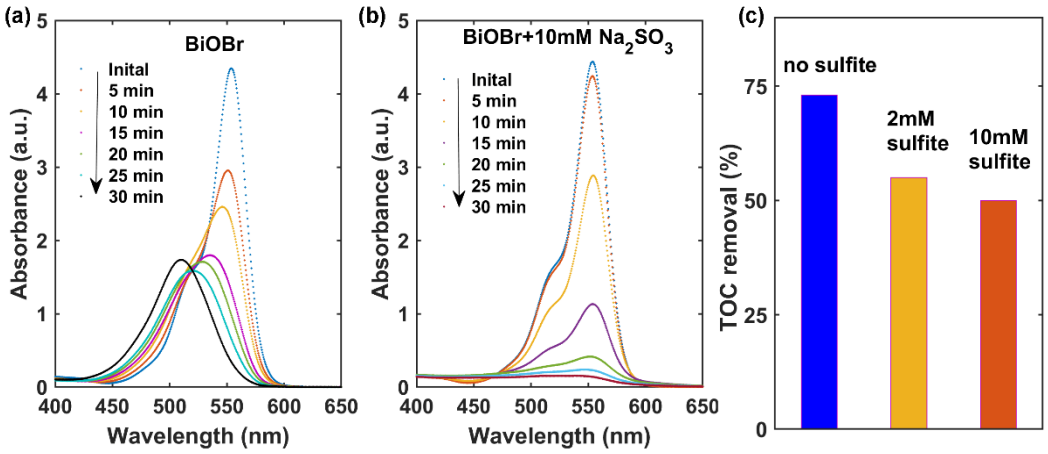

Figure 11. Time resolved UV-vis absorption of RhB solution with BiOBr under visible light (a) in the absence and (b) presence of 10 mM Na_2SO_3. (c) TOC removal of RhB after 1 hr simulated sunlight irradiation.

We have further demonstrated that sulfite-enhanced photocatalysis could be achieved with several other photocatalysts besides BiOBr (Figure 12b and c). The kinetics of MO degradation illustrated in Figure S3 show that the photocatalytic activities of Bi_2O_3, BiOI and P25 in the presence of 10 mM sulfite far exceeded those in the absence of sulfite. Specifically, MO photodegradation by Bi_2O_3 under 30 min visible light irradiation was increased from 16% without sulfite to 92% with sulfite; the degradation by BiOI under 30 min visible light irradiation was increased from 40% without sulfite to 86% with sulfite; and the degradation by P25 under 15 min simulated sunlight irradiation was increased from 39% without sulfite to 92% with sulfite.

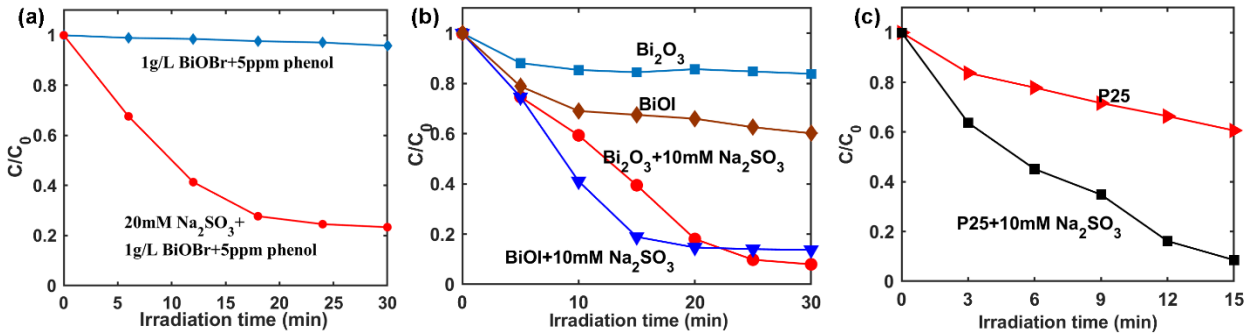

Figure 12. (a) photocatalytic activities of BiOBr for the degradation of phenol under visible light irradiation with/without 20 mM Na_2SO_3. (b) photocatalytic activities of Bi_2O_3 and BiOI for the degradation of MO under visible light with/without 10 mM Na_2SO_3. The initial concentration of MO was 10 ppm and the loading of Bi_2O_3 and BiOI was 0.5 g/L. (b) Photocatalytic activities of P25 for the degradation of MO under simulated sunlight with/without 10 mM Na_2SO_3. The initial concentration of MO was 40 ppm and the loading of P25 was 0.2 g/L.

Moreover, we compared Na_2SO_3 with other oxidants, like H_2O_2 and $K_2S_2O_8$, in terms of their contributions to photocatalysis (Figure 13). H_2O_2 increased the photodegradation because it could improve the quantum efficiency of the formation of superoxide radicals and hydroxyl radicals,[80] while the increase was much smaller than that promoted by Na_2SO_3. On the other hand, $K_2S_2O_8$ didn't contribute to the photocatalysis but it could directly oxide MO as peroxydisulfate is a powerful oxidizing agent with a oxidizing potential of 2.01 V.[81] Therefore, comparing to H_2O_2 and $K_2S_2O_8$, Na_2SO_3 is more promising to enhance the photodegradation of organic pollutants.

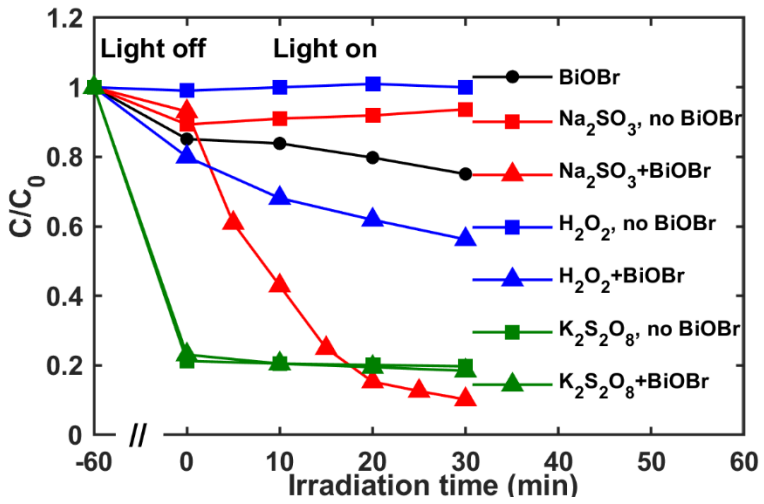

Figure 13. Photodegradation of MO under visible light for comparison of 10 mM Na_2SO_3, H_2O_2 and $K_2S_2O_8$. The initial concentration of MO was 10 ppm and the loading of BiOBr was 0.5 g/L.

3.5 Mechanism Study of Sulfite-enhanced Photocatalysis

Understanding the mechanism of sulfite-enhanced photocatalysis, including the roles of sulfite, types of reactive species, and possible formation pathways of the reactive species will help extend this novel approach to broader photocatalytic applications. The mechanism was investigated using the BiOBr/MO/sulfite system by addressing the following three questions. Does the addition of sulfite promote oxidization or reduction of MO? What are the reactive species and how are they generated from sulfite and the photocatalyst? Are other active species like oxygen important to sulfite-assisted photodegradation?

Na_2SO_3 and Na_2S have been widely used as sacrificial agents for photoelectrochemical hydrogen generation due to their hole-scavenging capability.[82] Thus, if sulfite-enhanced photocatalysis was mainly due to the effect of hole scavenging and promoting the availability of electrons for reduction reactions, other scavengers like EDTA and Na_2S should play the same role.

However, as indicated in Figure 14, both EDTA and Na_2S almost completely inhibited the photodegradation of MO by BiOBr. Therefore, it appears that holes played an important role during MO degradation and hole scavenging was not the main function of sulfite.

We believe that the active species responsible for increased MO degradation is the sulfite radical ($SO_3^{\bullet-}$) as it could react with organics via addition to carbon-carbon double bond and H atom abstraction.[68] To exclude the contributions of other possible active species involved in the photodegradation process, scavenging experiments of aqueous electron, $SO_4^{\bullet-}/SO_5^{\bullet-}$, and oxygen were also conducted. The possibility of aqueous electrons reacting with MO was studied using nitrate as an electron scavenger. Figure 14 shows that the addition of 20 mM nitrate to 10 mM sulfite solution did not have significant effect on MO photodegradation compared to that without nitrate. This result indicates that aqueous electrons did not make a substantial contribution to the sulfite-assisted enhancement in photocatalysis. To probe other sulfite related active species, such as $SO_4^{\bullet-}$ and $SO_5^{\bullet-}$, that may be produced by reactions of $SO_3^{\bullet-}$ with oxygen via a free radical chain mechanism,[83] experiments under anaerobic conditions in a sealed cell were conducted, and the results in Figure 14 show that sulfite greatly improved MO degradation at about the same level in the absence of oxygen as in the presence of oxygen. Therefore, sulfite radical itself was responsible for MO degradation, rather its reaction products with oxygen.

There are two possible pathways for the formation of $SO_3^{\bullet-}$. In the first pathway, sulfite anions are oxidized by photo-induced holes directly. This is feasible, since the redox potential of $SO_3^{\bullet-}/SO_3^{2-}$ couple is 0.75 V (vs NHE, at pH=7),[84] which is much lower than the VB position of BiOBr (3.09 V):

$$h_{VB}^{+} + SO_3^{2-} \rightarrow SO_3^{\bullet -} \quad (1)$$

The second pathway to produce sulfite radicals is through reaction of sulfite anions with hydroxyl radicals ($^{\bullet}OH$)[85]. This reaction is also feasible, because the redox potential of $^{\bullet}OH/OH^{-}$ (2.18 V vs NHE, at pH=7)[86] is higher than that of $SO_3^{\bullet -}/SO_3^{2-}$ (0.75 V):

$$h_{VB}^{+} + H_2O \rightarrow {}^{\bullet}OH + H^{+} \quad (2)$$

$$^{\bullet}OH + SO_3^{2-} \rightarrow SO_3^{\bullet -} + OH^{-} \quad (3)$$

To confirm that photo-induced holes contributed to the formation of sulfite radicals via the tow pathways as illustrated by Eqs (1)(2)(3), active species trapping experiments were conducted in the presence of 10 mM sulfite with isopropyl alcohol (IPA) used as a scavenger for holes and hydroxyl radicals (Figure 14). In the BiOBr/MO/sulfite suspension, the addition of IPA significantly inhibited the degradation of MO, especially when the concentration of IPA was 330 mM. This supports the hypothesis that the sulfite radical is the active agent and is produced by reaction with holes or hydroxyl radicals. Nevertheless, it is possible that the effect of IPA is not as a hydroxyl radical scavenger, but that it reacts with $SO_3^{\bullet -}$ or with sulfite/bisulfite and thus impeded the degradation of MO. To investigate this, the UV-vis absorption band of SO_3^{2-} (200 to 260 nm) was monitored in the BiOBr/MO system under visible light irradiation to indicate the dependence of sulfite consumption rate on IPA addition. Figure 15a shows that without adding sulfite there was no absorbance band from 200 to 260 nm, while a clear absorption band appeared upon the addition of sulfite and the absorbance decreased with time (Figure 15b), indicating the consumption of sulfite upon illumination. When IPA was added at a concentration of 15 mM

(Figure 15c) or at 330 mM (Figure 15d), the rate of sulfite loss slowed down, and it is particularly significant at 330 mM IPA. This result suggests that IPA did not react with sulfite/bisulfite or sulfite radicals but rather competed with sulfite for holes or hydroxyl radicals. It further supports the hypothesis that sulfite radicals were generated by sulfite/bisulfite anions reacting with holes or hydroxyl radicals following Eqs (1)(2)(3).

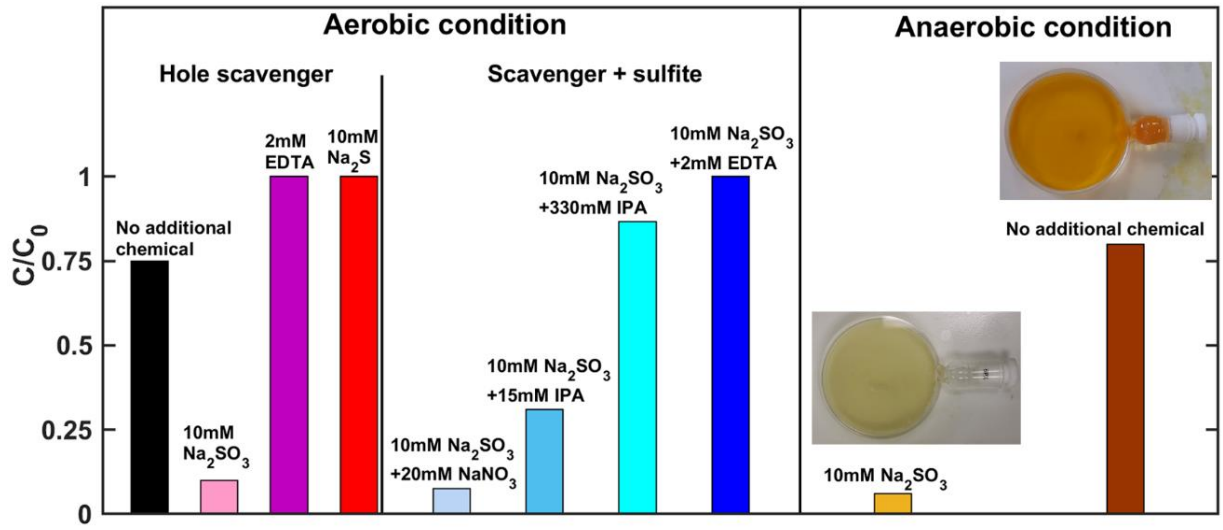

Figure 14. MO concentration percentages left after 30 min visible light irradiation in the absence or presence of various scavengers under aerobic or anaerobic conditions. The initial concentration of MO was 10 ppm and the loading of BiOBr was 0.5 g/L.

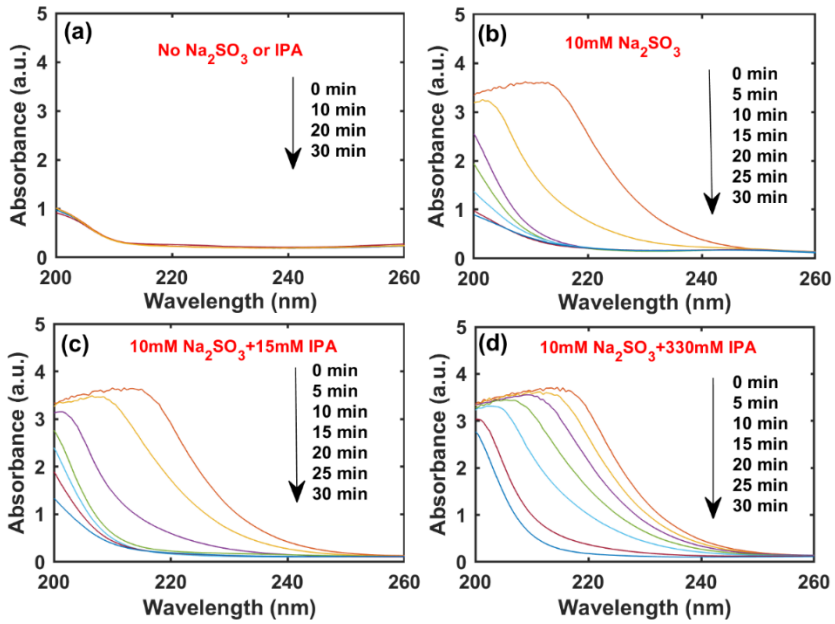

Figure 15. The UV-vis absorption band changes of SO_3^{2-}/HSO_3^- in the BiOBr/MO suspensions under visible light irradiation.

We have further evaluated our BiOBr/sulfite/MO system under truly aerobic condition by purging it with a stream of 100 ml/min air, and we have compared the MO degradation kinetics with and without air purging. As displayed in Figure 16a, it is obvious that air purging retards the degradation of MO, another evidence that $SO_4^{\bullet-}$ and $SO_5^{\bullet-}$ should not be the major reactive species in our BiOBr/sulfite/MO system. We also monitored the sulfite concentration in the system and we indeed observed faster sulfite depletion with air purging (Figure 16b and c). This result agrees with literature that sulfite can be scavenged by oxygen. However, in our reaction system, even under truly aerobic conditions $SO_3^{\bullet-}$ is still the major reactive species as evidenced by the experimental result that a more aerobic system led to less MO degradation. Some explanations are given below. Firstly, Sulfite radicals generated in our system is caused by reaction of photo-

generated holes reacting with sulfite; hence, as long as photo-illumination continues, the generation of sulfite radicals is non-stopping as long as there is sulfite present, and the hole generation should be the rate-limiting step for $SO_3^{\bullet-}$ generation. The air purging may have depleted sulfite so fast (Figure 16c) that little sulfite is left to react with photo-generated holes to form $SO_3^{\bullet-}$, thus impeding the MO degradation. Secondly, even though oxygen can react with $SO_3^{\bullet-}$ to produce $SO_5^{\bullet-}$, the generated $SO_5^{\bullet-}$ could react with SO_3^{2-} and produce SO_5^{2-} and $SO_3^{\bullet-}$, which is called chain reaction that can regenerate $SO_3^{\bullet-}$.[4] Thirdly, because of the strong oxidizing capability of $SO_4^{\bullet-}$ and $SO_5^{\bullet-}$, they are prone to react with photo-generated electrons and it is possible they are scavenged by electrons before reacting with MO. All the above discussion and the expeirmental results (Figure 16) support the conclusion that in a truly aerobic system involving BiOBr/sulfite/MO under photo-illumination, $SO_3^{\bullet-}$, not $SO_4^{\bullet-}$ or $SO_5^{\bullet-}$, is the major reactive species for MO degradation.

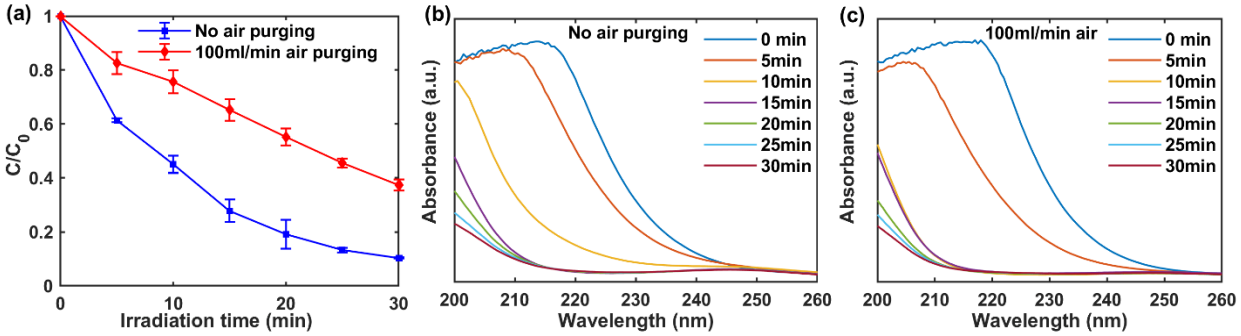

Figure 16. (a) Photodegradation kinetics of MO without and with 100 ml/min air purging under visible light irradiation, and the UV-vis absorption band changes of SO_3^{2-}/HSO_3^- in the MO solutions (b) without and (c) with air purging. The initial concentration of MO, sulfite and BiOBr were 10 ppm, 10 mM and 0.5 g/L, respectively. HCl was added to adjust the initial pH to 7.5.

All these results support the hypothesis that the sulfite radical is the main active species in degrading MO in the sulfite-promoted photodegradation process. These sulfite radicals are derived from sulfite/bisulfite anions reacting with holes or hydroxyl radicals. The overall process is illustrated in Figure 17. It should be noted that although holes and hydroxyl radicals can attack MO molecules directly,[16] they make little contribution to the degradation of MO compared to sulfite radicals when sulfite is present, since the degradation rate is slow without sulfite whereas significant enhancement of degradation is obtained upon the addition of sulfite. Furthermore, the concentration of sulfite (10 mM) was much higher than that of MO (0.03 mM), so it is more likely for holes and hydroxyl radicals to react with sulfite anions than with MO.

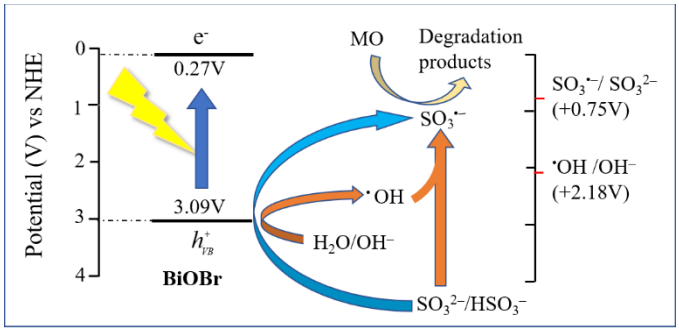

Figure 17. The proposed pathways of sulfite radicals formation and MO photodegradation under visible light using BiOBr.

However, it is unknown that how the organics are degraded, i.e., what are the degradation pathways. Recently, few studies using chromatography and mass spectroscopy techniques, like LC-MS and GC-MS, have analyzed the sulfite-promoted photodegradation intermediates of MO and suggested the photodegradation pathways.[87-89] These studies proposed that high oxidative $SO_3^{\cdot-}$ and $OH^{\cdot}$ could destroy the N=N bonds, methyl bonds, and ethanediamine groups and also

make aromatic substitution of one of the benzene rings with hydroxyl groups.[87] The analysis on the intermediates also showed that the sulfite group was added into the organics and the intermediates, suggesting that the sulfite radicals mainly oxidize (take electrons from) the organics to produce reactive organic species that are unstable or easy to react with other species, consequently, the organics, including the target pollutant and intermediates, are converted to molecules of lower molecular weights. Further study is still in need to prove this mechanism conclusively.

3.6 Conclusion

In summary, we have developed a sulfite-enhanced visible-light-driven photodegradation process using BiOBr/methyl orange (MO) as the model photocatalyst/pollutant system. We found that the degradation rate of MO was greatly enhanced by sulfite, and the enhancement increased with the concentration of sulfite. The degradation rate constant was improved by twenty-nine times in the presence of 20 mM sulfite. Studies using hole scavengers suggest that sulfite radicals generated by the reactions of sulfite (sulfite anions or bisulfite anions) with holes or hydroxyl radicals are the active species for MO photodegradation using BiOBr under visible light. The sulfite-assisted photocatalysis approach has also been successfully demonstrated in the photodegradation of RhB and phenol. The developed method implies the potential of introducing external active species to improve photodegradation of organic pollutants.

CHAPTER 4

PROBE ADSORPTION-PHOTOCATALYSIS SYNERGY BY COMBINING EXPERIMENTS AND KINETIC MODELING[3]

4.1 Background and Hypothesis

Adsorption of organic pollutants onto the surface of photocatalysts is important for the photodegradation process [90] and a wide range of photocatalysts with high adsorption capacity have been developed and achieved high photodegradation efficiency, benefiting from the adsorption-photocatalysis synergy.[33, 34, 91-100] However, the majority of these photocatalysts are not appropriate to serve as model photocatalyst to thoroughly investigate the synergy because of the following reasons: 1) adsorption sites and photoactive sites are associated with different components and the increased distance between these sites undermines the synergistic effect between adsorption and photocatalysis; [34, 91-95] 2) nanosized photocatalysts, though have high adsorption due to large surface area and have the same sites for both adsorption and photocatalysis, do not have tailorable adsorption capacity and suffer from difficult recollection after use;[33] 3) the content of photoactive component in the composites is low because of the adsorption is determined by the non-photoactive matrix.[96] In this context, it is beneficial to develop a series of model photocatalysts that have the adsorption sites and photocatalysis sites on the main component, microstructured morphology, and adsorption capacity that can be easily tailored to study the adsorption-photocatalysis synergy.

---

[3] Part of this chapter is reprinted with permission from "Mesoporous TiO_2–BiOBr microspheres with tailorable adsorption capacities for photodegradation of organic water pollutants: probing adsorption–photocatalysis synergy by combining experiments and kinetic modeling" by Deng, Wei, Fuping Pan, Bill Batchelor, Bahngmi Jung, Peng Zhang, Ahmed Abdel-Wahab, Hongcai Zhou, and Ying Li, 2019. Environmental Science: Water Research & Technology, 5, 769-781. Copyright [2019] by Royal Society of Chemistry.

In addition to experiments, kinetic modeling is a powerful tool to study the adsorption-photocatalysis synergy and quantitatively evaluate the performance of photocatalysts with high adsorption capacity. Nevertheless, a simple pseudo first-order model, $\ln(C/C_0) = -k_{pfo}t$, is widely used for evaluating high adsorption photocatalysts.[95-100] This approach considers only the amount of organic pollutants in solution but not the amount adsorbed on the photocatalyst surface. As such, it will be inaccurate whenever the amount of adsorbed pollutant is a substantial fraction of the total. More comprehensive kinetic modeling methods are developed but are not applied to elucidate the synergy or quantitatively study the appropriate model photocatalysts.[101-106] Moreover, research efforts have been mainly focused on demonstrating photodegradation promotion brought by high levels of adsorption, adverse effects of adsorption, such as accumulation of recalcitrant degradation intermediates on the photocatalyst surface and diminished recyclability of the photocatalysts, have received much less attention. Therefore, combination of developing comprehensive kinetic model and designing appropriate model photocatalysts, as well as investigation on adverse effects of high adsorption, are in need to gain a deeper understanding of the synergy and help advance solar-driven photodegradation of organic wastewater pollutants.

In this study, we synthesized mesoporous TiO_2(amorphous)-BiOBr microspheres via a facile one-pot solvothermal method. This approach produced photocatalysts with tailorable surface areas and adsorption capabilities that were used as model photocatalysts to explore the adsorption-photocatalysis synergy. We further performed kinetic modeling that considered adsorption and photocatalytic reactions in order to elucidate the synergy and extract the values of rate constants from experimental data to quantitatively evaluate the photocatalysts. The adverse effects of high levels of adsorption were also investigated.[107]

4.2 Experiment Details

TiO_2-BiOBr microspheres were synthesized through a facile one-pot solvothermal method. Typically, bismuth nitrate pentahydrate (2 mmol, 0.98 g) was dissolved in 30 ml ethylene glycol, followed by the addition of certain amount of TBOT as the titanium precursor. Then CTAB (2 mmol, 0.729 g) was added into the above solution under rigorous stirring, and the mixture was stirred for another 30 min. The solution was transferred into a 50-ml Teflon-lined reactor and heated at 160 ºC for 12 h. After cooling down to room temperature, the precipitate was collected and washed thoroughly with ethanol and deionized water. The final product was dried at 80 °C in a vacuum furnace overnight. Amorphous TiO_2 was synthesized using the same process except no bismuth nitrate was added to the solution. The TiO_2-BiOBr samples were labeled as TBB-x, where x is the atomic ratio of TBOT to bismuth nitrate in the precursor solutions.

The extent of MO adsorption onto the photocatalysts was measured in experiments with 10 mg photocatalysts dispersed in 100 ml of a 10 mg/L MO solution under magnetic stirring. MO concentrations in the adsorbed phase at different times were calculated by dividing the difference between the initial and measured solution concentrations of MO by the photocatalyst loading. The adsorption isotherms were obtained from results of equilibrium adsorption experiments conducted using 0.25 g/L of TBB-0.6 and a range of doses of MO (5, 10, 20, 30, 40 50, 70, 100 mg/L). After the solutions were stirred for 1 hr, the MO concentrations in solution were then measured and the concentrations in the adsorbed-phase were calculated. The photoactivities of the samples were evaluated via kinetic experiments on the photodegradation of MO, RhB and phenol under simulated sunlight provided by a 150 W solar simulator (Oriel Sol1A, Newport). Typically, 7.5

mg photocatalyst was dispersed in 50 ml MO or RhB solution at 15 mg/L. While for phenol degradation, 12 mg photocatalyst was dispersed in 40 ml of a 10 mg/L phenol solution. pH values of the solutions were close to neutral without further adjustment. Prior to irradiation, the suspension was stirred in dark for 1 hr to ensure adsorption equilibrium. To conduct the cycling tests, the spent photocatalysts after the initial test were collected, washed with water, dried and used for the second test.

4.3 Characterization Results of the TiO_2-BiOBr Microspheres

XRD patterns of the BiOBr and TiO_2-BiOBr samples are shown in Figure 18a. All diffraction peaks are well indexed to the tetragonal structure of BiOBr (JCPDS File No. 73-2061),[76] but no characteristic peak of crystalline TiO_2 is observed, indicating that TiO_2 is in amorphous phase. The synthesized pure BiOBr has high crystallinity as determined by the sharp diffraction peaks with high intensity, while TiO_2-BiOBr samples possess weakened crystallinity shown by the broadened and low-intensity diffraction peaks. The principal peaks near 32 º could be deconvoluted to two major peaks that are indexed to (012) and (110) facets of BiOBr phase. The full width at half maximum (FWHM) of the (110) peaks are calculated and shown in Figure 18b, where the composites were found to have larger FWHM than pure BiOBr. The smaller crystallites would result in larger surface areas and would be more efficient in transferring charge carriers (electrons and holes) in bulk to the crystallite surfaces. Possible doping of Ti atoms may introduce defects into BiOBr crystal structures, which also affects crystallinity. Significant peak shifts to large 2 theta angles are also observed in magnified XRD spectra (Figure 18b), suggesting the doping of Ti and chemical interactions between TiO_2 and BiOBr.[96] In addition, some

indicative peaks of BiOBr, such as (001), (011), (012), (112), (014) and (121), are very weak or not visible in the patterns of TiO_2-BiOBr samples, probably because TBOT impedes the growth of these facets or the facet coupling between BiOBr and TiO_2 makes these facets less detectable.[108]

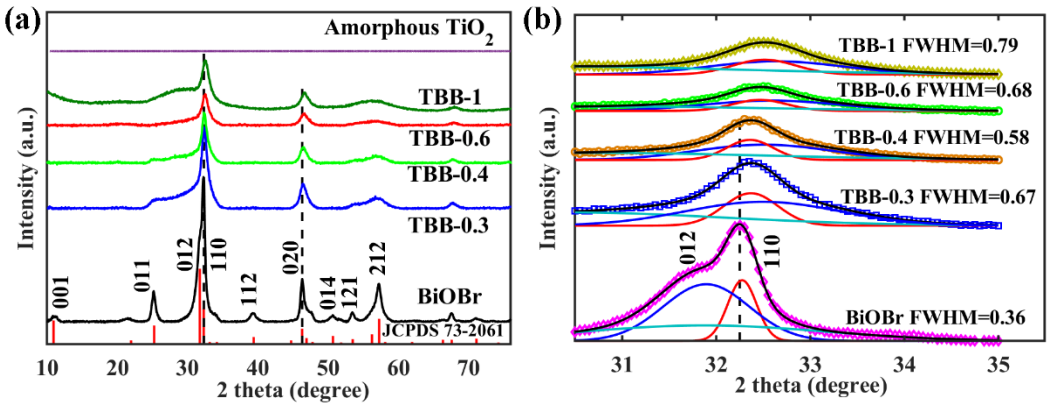

Figure 18. (a) XRD spectra and (b) magnified spectra of the samples.

The morphology of the samples is presented by SEM images (Figure 19). Pure BiOBr has a three-dimensional hierarchical microsphere structure with an average diameter of about 3 μm. The microspheres are constructed by stacked thin microplates, as clearly shown in Figure 19a. TiO_2-BiOBr samples also have similar microsphere structure, implying TBOT does not change the formation route of BiOBr, that is, the growth of BiOBr microplates followed by self-assembly to microspheres[73, 74, 109]. Compared with BiOBr, TiO_2-BiOBr samples have more perfect spherical structure, indicating TBOT possibly also functions as a potential surfactant that could modify microstructures in the synthesis of BiOBr. Microplates in TiO_2-BiOBr samples are more densely stacked but have less sharp edges. This becomes more obvious as TiO_2 content increases and is most likely the result of decreased crystallinity of BiOBr. EDS mapping images of TBB-0.6

microspheres confirmed that elements Bi, O, Br and Ti are distributed homogeneously within individual microspheres (Figure 20). In addition, there are no exotic TiO_2 nanoparticles, clusters or nanowires observed in TBB-0.3, 0.4, 0.6 and 1, suggesting that amorphous TiO_2 is uniformly distributed in BiOBr microplates. TBB-2 has aggregates coated on the microsphere surface (Figure 2g) and we found that TBB-2 had almost the same adsorption capacity and photodegradation performance as TBB-1, therefore, TBB-2 was not included in the following sections. It is interesting to note that solvothermal treatment of TBOT and CTAB mixture solutions without adding bismuth nitrate yielded large irregular-shaped amorphous TiO_2 blocks that were not observed in the TiO_2-BiOBr composites (Figure 2h). This suggests that during the synthesis process of TiO_2-BiOBr composites, BiOBr crystallites formed first and confined the formation of amorphous TiO_2 to the space between BiOBr crystallites inside the microplates. At the same time, amorphous TiO_2 inhibited the growth of BiOBr crytallites and led to the formation of smaller BiOBr crystallites. This nondestructive incorporation of TiO_2 into BiOBr enables not only uniform distribution of TiO_2 in BiOBr, but also the retainment of the microsphere structure of BiOBr. This results in increased interfacial area between TiO_2 and BiOBr, easy collection of the photocatalysts after use, and improved light trapping due to multiple reflections among the microplates.

TEM analyses were performed on BiOBr and TBB-0.6 to investigate the morphology and crystal structure. The BiOBr sample has clear lattice fringes and high crystallinity (Figure 21a, b). The inter-planar lattice spacings of 0.278, 0.281 and 0.351 nm are attributed to the (110), (012) and (012) planes of BiOBr, respectively. Compared to BiOBr, TBB-0.6 has less clear lattice fringes because of the lower crystallinity and smaller crystallites (Figure 21c, d). The spacings in TBB-0.6 are attributed to the (110) planes of BiOBr phase but are slightly smaller than 0.278 nm, which is in accord with the XRD spectra. Areas with no clear lattice structure are also observed

between BiOBr crystallites and highlighted in Figure 3d with dashed lines. These areas are possibly amorphous TiO_2 as discussed in the XRD analysis. Therefore, it is high likely that amorphous TiO_2 formed between BiOBr crystallites. As a result, the size of BiOBr crystallites in TBB-0.6 (about 5 to 10 nm) is much smaller than that in pure BiOBr (about 20 to 40 nm).

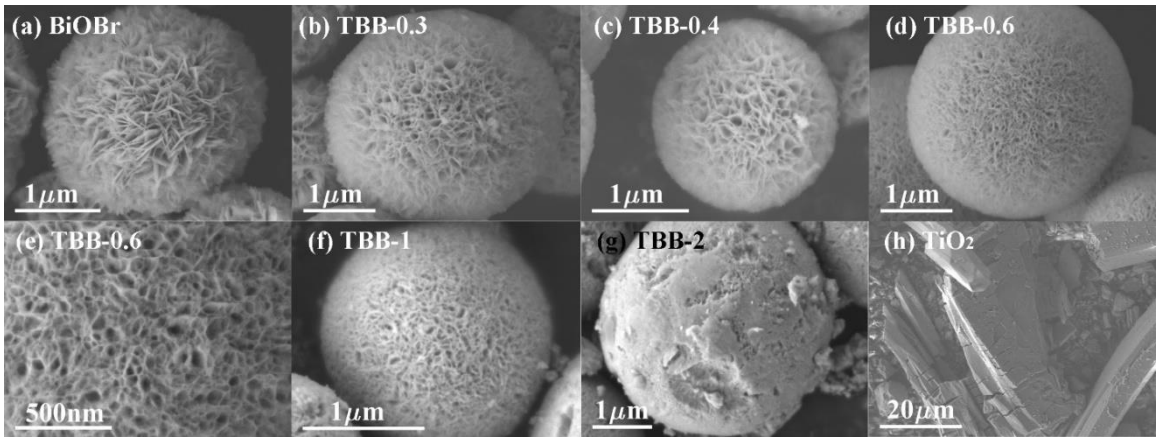

Figure 19. SEM images of (a) BiOBr, (b) TBB-0.3, (c) TBB-0.4, (d, e) TBB-0.6, (f) TBB-1, (g) TBB-2, and (h) amorphous TiO_2.

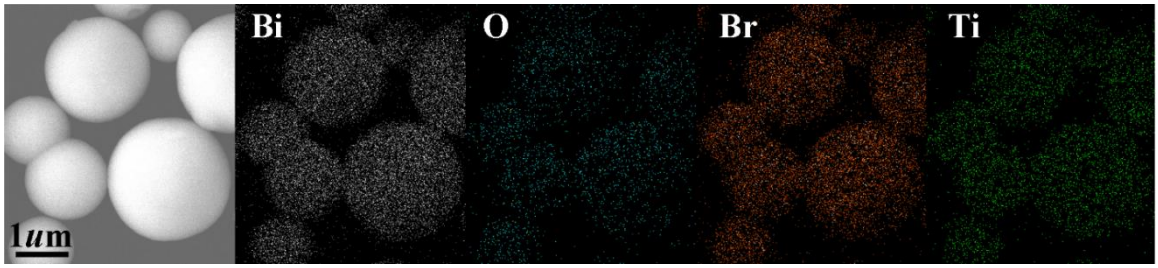

Figure 20. SEM and EDS mapping images of TBB-0.6. The images show uniform distribution of the elements.

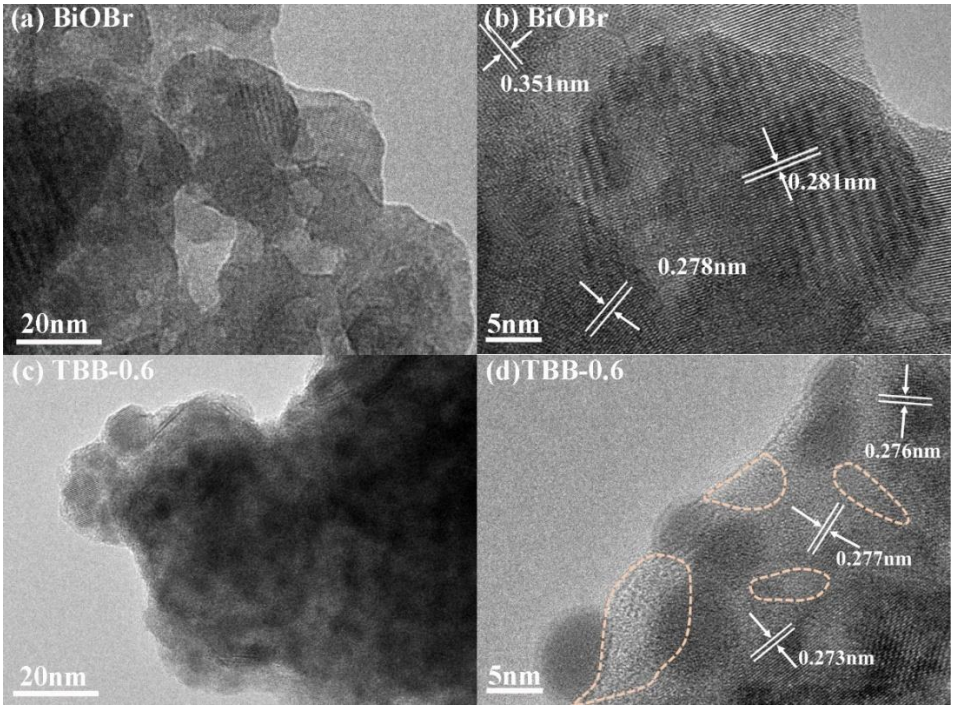

Figure 21. TEM and HRTEM images of (a, b) BiOBr and (c, d) TBB-0.6.

The surface compositions and chemical states of the samples were investigated by XPS. The survey spectra (Figure 22a) confirm the existence of Bi, O, Br and C in all samples and Ti in TiO_2-BiOBr samples. The Bi 4f spectra of BiOBr (Figure 22b) can be resolved into two spin orbit components at binding energies of 159.4 eV and 164.8 eV that are attributed to Bi $4f_{7/2}$ and Bi $4f_{5/2}$, respectively. This indicates that the chemical state of bismuth in the sample is Bi^{3+}. Significant peak shifts of bismuth to lower binding energies are observed in TiO_2-BiOBr samples possibly because of the strong interactions between TiO_2 and BiOBr.[32] suggesting the intimate contact between TiO_2 and BiOBr. The spectra ranging from 450 eV to 470 eV (Figure 22c) of the TiO_2-BiOBr composites can be deconvoluted into three components. For example, the spectrum of TBB-0.3 is deconvoluted to Ti $2p_{3/2}$ and Ti $2p_{1/2}$ at binding energies of 458 eV and 464.9 eV, as well as a peak for Bi $4d_{3/2}$ at 465.4 eV. The peak of Bi $4d_{5/2}$ is located around 440 eV and is

shown in Figure 4a. Therefore, it is affirmed that titanium exists in the samples and as TiO_2, since no evidence of Ti^{3+} is presented. As the concentration of TBOT in the precursors increases from TBB-0.3 to TBB-1, the areas of Ti 2p peaks become larger and the peaks shift to lower binding energies, corresponding to higher TiO_2 contents and stronger chemical interactions between TiO_2 and BiOBr. The atomic ratios of Ti to Bi in the samples calculated from XPS spectra and SEM-EDX are compared with the ratios in synthesis precursors in Figure 22d. The measured ratios from XPS are slightly higher than measured from SEM-EDX, indicating that the composites probably have slightly higher TiO_2 contents on the surface of the microspheres, but the difference is not significant and the distribution of TiO_2 is relatively uniform.

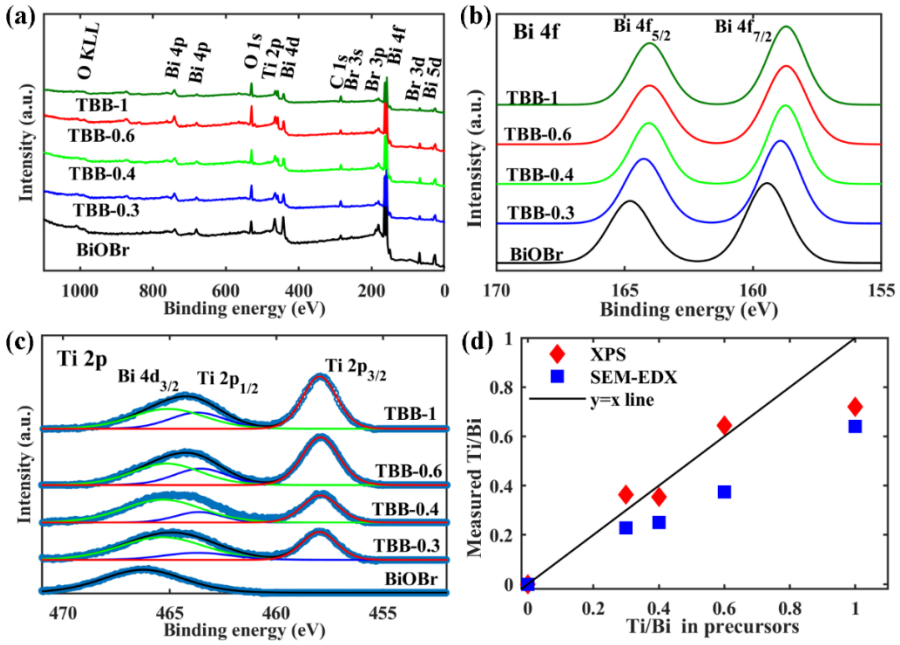

Figure 22. XPS spectra of the samples: (a) survey, (b) Bi 4f and (c) Ti 2p, as well as (d) atomic ratios of Ti to Bi measured from XPS and SEM-EDX compared with the ratio in the synthesis precursors; a 1:1 line (y=x) was also added in (d) for comparison. Bi $4d_{3/2}$ overlaps with Ti $2p_{1/2}$ around 465 eV, which is clearly shown in (c) but not in (a).

Nitrogen adsorption–desorption isotherms of BiOBr and TiO_2-BiOBr microspheres show typical type-IV curves that indicate the mesoporous nature of the samples (Figure 19a). BiOBr has a H3 type hysteresis loop that is typically shown by aggregates of plate-like particles, according to the IUPAC classification.[78] The existence of such particles is confirmed by the SEM images (Figure 19) that show that all samples are microspheres formed by aggregation of microplates. TiO_2-BiOBr samples have predominant H2 type hysteresis loops and keep the feature of the H3 type. The broader H2 type hysteresis loops associated with capillary condensation are attributed to a narrow range of uniform mesopores. As exhibited in Figure 23b, BiOBr and TiO_2-BiOBr composites have similar major mesopore width around 3.6 nm determined by Barrett-Joyner-Halenda (BJH) method.[78] Though large spaces exist between the microplates that have sizes ranging from tens to hundreds of nanometers (Figure 19), it is believed that mesopores with widths around 3.6 nm should exist inside the microplates, possibly between BiOBr crystallites. Figure 23c shows that TiO_2-BiOBr microspheres possess remarkably increased specific BET surface areas and pore volumes compared to BiOBr. A 6-fold increase of specific surface area is achieved for TBB-1, compared to BiOBr. The introduction of TBOT probably reduces the crystallite size of BiOBr and increases the number of mesopores between the crystallites, which explains why TiO_2-BiOBr samples show the same mesopore width as BiOBr but have much larger pore volumes and surface areas. Therefore, the surface areas of the composites could be facilely tailored by the amount of TiO_2.

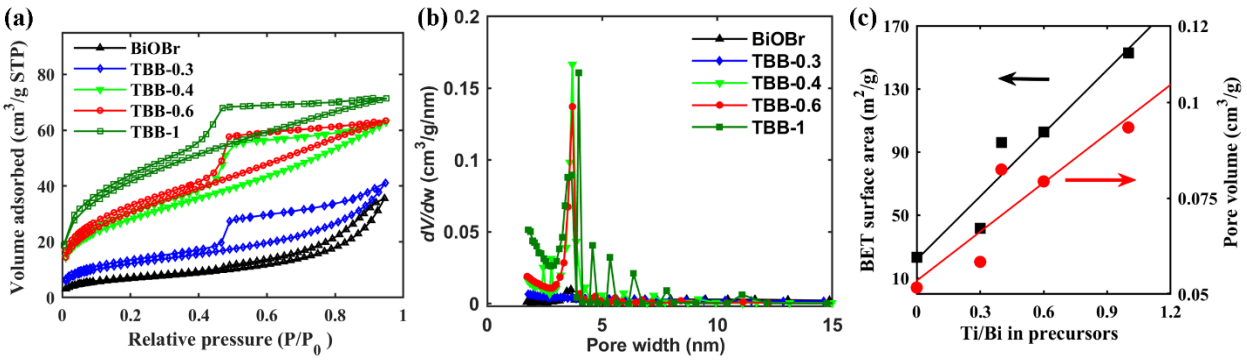

Figure 23. (a) Nitrogen adsorption-desorption isotherms at 77 K, (b) pore size distributions of the samples, and (c) effect of precursor Ti/Bi on specific BET surface areas and pore volumes of the samples.

The optical properties of the samples were characterized by UV-vis diffuse reflectance (Figure 24a). The light absorption of TiO_2-BiOBr and pure BiOBr is mainly located in UV range. TBB-0.3, 0.4 and 0.6 have stronger UV absorbance than BiOBr while TBB-1 has almost the same absorbance with BiOBr, which is possibly caused by the change of morphology and crystallinity. The corresponding tauc plots (Figure 24b) indicate that TiO_2-BiOBr microspheres have slightly large band gaps than pure BiOBr. This should be ascribed to the introduction of amorphous TiO_2. The photoluminescence spectra shown in Figure 24c offer insights on the recombination and lifespan of photo-induced electrons and holes in the samples. The spectra were obtained at an excitation wavelength of 300 nm. All the samples show similar spectra patterns with broad emission peaks at around 470 nm and 550 nm, but the emission intensities vary significantly. TiO_2-BiOBr samples have much weaker emission intensities than BiOBr. This is probably because the composites have smaller BiOBr crystallites that facilitate the diffusion of photoinduced electron-hole pairs to crystallite surfaces and have intimate TiO_2-BiOBr heterojunctions, resulting in higher

separation efficiency of the pairs. Meanwhile, the significantly decreased crystallinity of TBB-0.6 and TBB-1 could retard the electron-hole separation, consequently, TBB-0.6 and TBB-1 have slightly stronger emission intensities than TBB-0.3 and TBB-0.4.

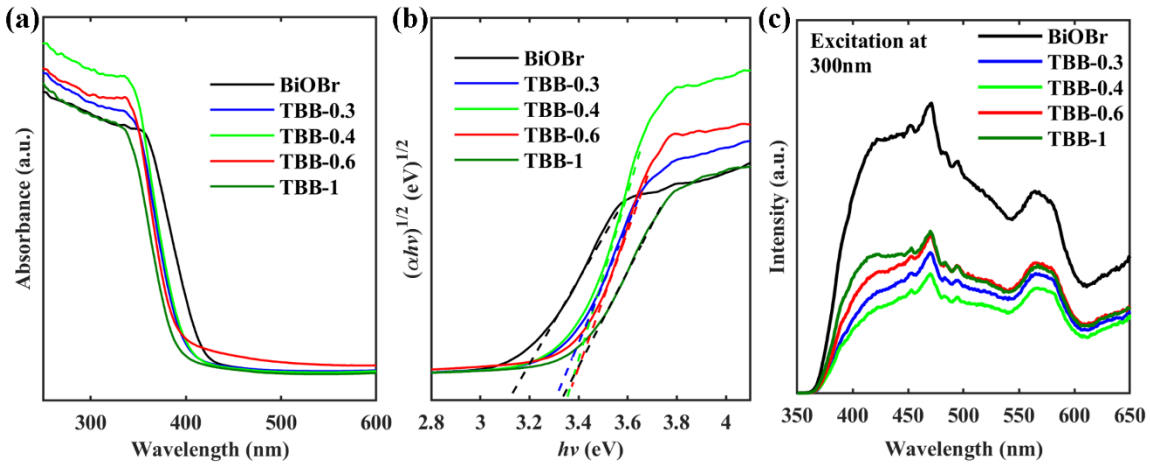

Figure 24. (a) UV-vis diffuse reflectance spectra, (b) corresponding tauc plots, and (c) photoluminescence spectra of the samples.

Based on the characterization results and discussions, the synthesis process of TiO_2-BiOBr microspheres is proposed and illustrated in Figure 25. Upon heating, bismuth precursor (Bi^{3+}) and bromine source (CTAB) start reactions to produce BiOBr crystallites in ethylene glycol. Titanium precursor (TBOT) does not change the formation route of BiOBr microspheres (self-assembly of microplates to microspheres), but TOBT molecules are dispersed among initially produced BiOBr crystallites and inhibit the further growth and connection of the small BiOBr crytallites to produce large crystallites. As heating continues, TBOT molecules are decomposed, consequently, amorphous TiO_2 and mesopores are formed between small BiOBr crystallites. Therefore,

amorphous TiO_2 tailors the size of BiOBr crystallite, pore volume and surface area of TiO_2-BiOBr composites but does not change the microplates-assembled microsphere structure.

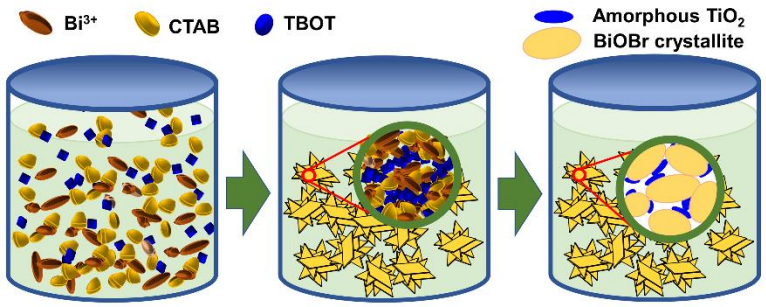

Figure 25. Schematic illustration of the synthesis process for TiO_2-BiOBr microspheres.

4.4 Adsorption Kinetics and Isotherms

The adsorption kinetics of MO on the samples are shown in Figure 26a, where both BiOBr and TiO_2-BiOBr samples exhibit fast adsorption, since over 95% of the equilibrium adsorption occurs in less than 10 min. However, amorphous TiO_2 shows negligible adsorption of MO and TiO_2-BiOBr samples show much higher adsorption capacity than BiOBr. Concentration of the adsorbed phase at equilibrium on TBB-0.6 and TBB-1 is about 54 mg/g, which is around 3.4 times than that on BiOBr. The correlation between equilibrium adsorption amounts and surface areas of the samples reveals that the enhanced adsorption capacity of the composites can be mainly attributed to the surface area improvement (Figure 26b). It can be concluded that adsorption sites are on the surface of BiOBr, because amorphous TiO_2 alone does not adsorb MO, but the introduction of TiO_2 reduces the crystallite size of BiOBr and consequently results in larger surface area and higher adsorption. The adsorption isotherm of MO on TBB-0.6 is presented in Figure 26c and was fitted using both the Langmuir model and the Freundlich model. The Freundlich model

uses an empirical equation to describe the relation between the concentration of a solute in the adsorbed-phase (q_e) to the concentration of the solute in the fluid (C): $q_e = KC^n$, where K (mg^{1-n}L^n/g) and n (0<n<1) are the Freundlich constants. Compared to the Langmuir model, the Freundlich model fitted the data better. The parameters of the Freundlich model are listed in Figure 26c and will be used in the kinetic modeling to be developed.

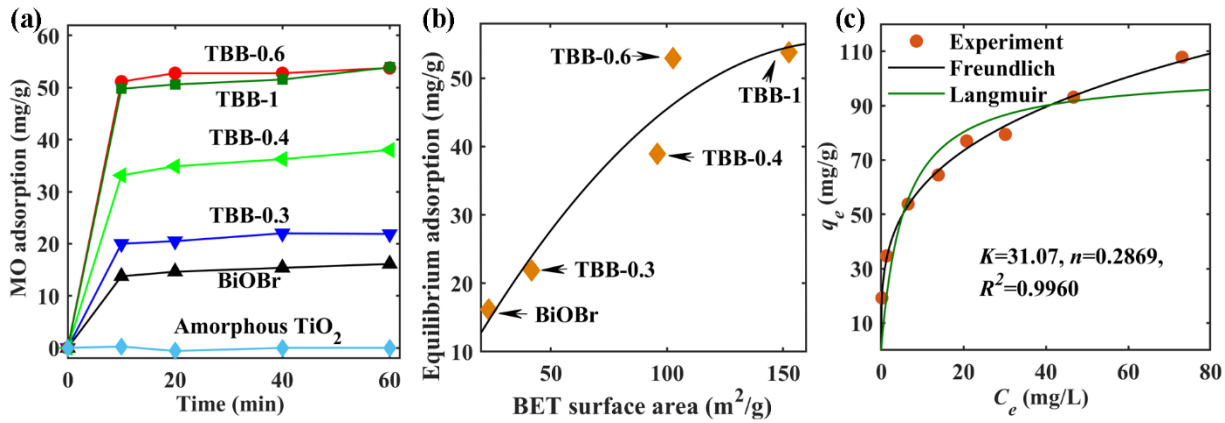

Figure 26. (a) Time-resolved adsorption kinetics of MO on the samples and (b) the correlation between equilibrium adsorption amount and surface area of the samples; (c) adsorption isotherms of MO on TBB-0.6. The parameters of the Freundlich model are listed.

4.5 Kinetic Modeling of Combined Adsorption with Photocatalytic Reactions

The single-phase, batch, pseudo-first-order model ($\ln(C/C_0) = -k_{pfo}t$) is often used;[95, 96, 98-100] however, this simple model is not appropriate for systems where strong adsorption occurs and the amount of contaminant in the adsorbed phase is substantial relative to the total amount in the system. When this is the case, the material balance for the system must consider how reaction changes the concentrations in all phases. This is true regardless of what form of rate

equation is used.[101-106] In such a system, the amount of contaminant in the adsorbed phase must be considered in the material balance, regardless of what form of rate equation is used. Such an approach will be taken here. First, assume that the rate of reaction per unit mass of photocatalyst (r_m) is proportional to the surface concentration of adsorbed target compound (q), that is $r_m = k_s q$, where k_s is the intrinsic reactivity of the photocatalyst. The rate of removal per unit volume of solution (*r*) can be obtained by multiplying by the photocatalyst concentration solid loading (D), i.e. $r = k_s D q$. If the rate of mass transport from the bulk solution to the surface of the photocatalyst and the rate of adsorption onto the photocatalyst from the adjacent solution are rapid compared to the rate of surface reaction, then the surface concentration can be assumed to be in equilibrium with the bulk solution concentration. Adsorption kinetic data indicate that adsorption of MO onto the photocatalysts was complete within a few minutes, while MO degradation took tens of minutes. Therefore, the assumption of adsorption equilibrium is not unreasonable. However, additional kinetic data may show that transport kinetics play some role in the observed removal kinetics. When substantial adsorption occurs, the material balance needs to consider that the target compound exists in both the solid and solution phases: *d*(mass of target in system/volume of solution)/*dt* = rate of removal:

$$\frac{d}{dt}(C + Dq) = -r \tag{4}$$

Differentiation, application of the chain rule ($\frac{dq}{dt} = \frac{dq}{dC} \cdot \frac{dC}{dt}$) and rearrangement give:

$$\frac{dC}{dt} = -r / (1 + D\frac{dq}{dC}) \tag{5}$$

If a linear isotherm applies ($q = K_p C$), this would provide a result that appears to be like that in a system with first-order removal rate without considering adsorption ($dC/dt = k_{app} C$), but the apparent first-order reaction coefficient would include effects of adsorption ($k_{app} = k_s K_p D/(1+DK_p)$).

Since the Freundlich adsorption isotherm ($q = KC^n$) well fits data for equilibrium adsorption on TBB-0.6, it is used to describe adsorption equilibria: $r = k_s DKC^n = k_f DC^n$, where k_f is the overall rate constant ($k_f = Kk_s$). Combining this rate equation with the material balance equation for a batch system when adsorption is important gives:

$$\frac{dC}{dt} = -\frac{k_f DC^n}{1+KnDC^{n-1}} \tag{6}$$

Note that the derivative of the solution concentration is not equal to the rate of MO degradation per volume of solution ($k_f DC^n$). The denominator on the right side makes the derivative of solution concentration (dC/dt) to be less than the rate of MO degradation, because MO is being removed both from the surface of the solid and from the solution. Simulations of photodegradation kinetics with equilibrium adsorption were then performed by solving Eq.(6) numerically employing MATLAB function ode45. The overall rate constants were also obtained by nonlinear fitting of the experimental data via MATLAB function nlinfit.

To study the effects of the adsorption capacity (K) and rate constants (k_f and k_s) on photodegradation kinetics, simulations were conducted at various values of (K , k_s , k_f) and the results are presented in Figure 27a for solution phase concentrations and in Figure 27b for total

concentrations. The total concentration of MO can be defined as the amount in the solution and on the photocatalyst surface per volume of solution and it was calculated assuming adsorption equilibrium ($C_{total} = C + DKC^n$). It is important to remember in examining Figure 27a, that the slopes of the concentration-time plots are not equal to the rate of degradation. However, the slopes in Figure 27b are equal to rate of degradation. When K is kept constant at 5, the concentrations in the adsorbed and the solution phases after the dark period (t = 0) are not affected by different values of k_s, but increasing values of k_s (0.1, 0.12, 0.2) do result in more rapid degradation. This should be expected because k_s represents the intrinsic reactivity of the photocatalyst. When k_s is held constant at 0.2, the higher value of K (10 vs 5) yields not only higher removal due to adsorption (lower solution concentration at t =0 in Figure 27a), but also more rapid photodegradation kinetics (greater slope in Figure 27b). This unambiguously demonstrates the benefits of the adsorption-photocatalysis synergy. When the overall rate constant ($k_f = K\ k_s$) is held at 0.5 and K and k_s vary, it is seen that the adsorption plays a more significant role than photocatalysis in removing pollutants from solution but not in total removal. For example, the purple line (K =20, k_s =0.025) shows lower MO concentrations in solution (Figure 27a) but higher total concentrations in solution and on solid (Figure 8b) than the dashed black line (K =5, k_s =0.1).

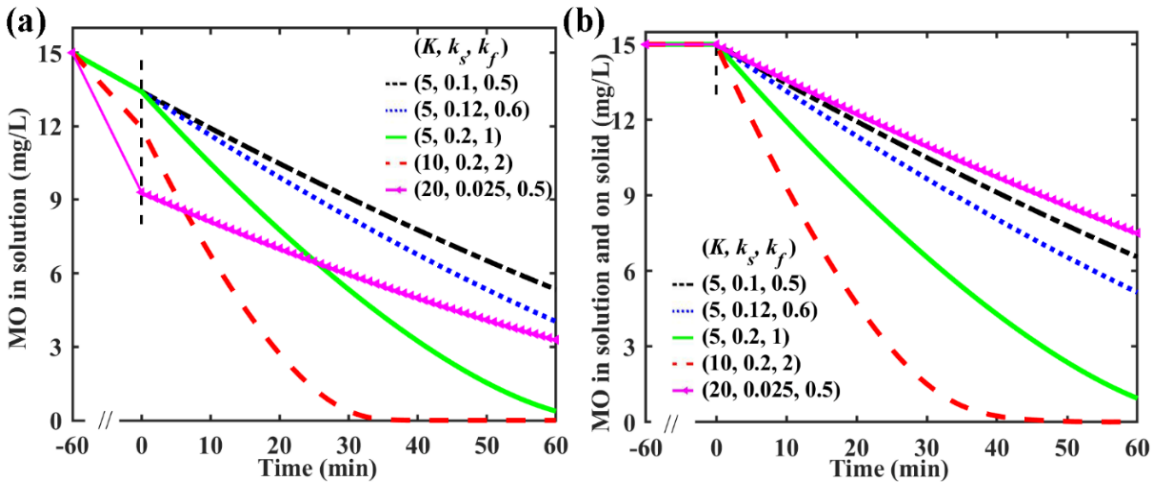

Figure 27. Parametric simulation results: (a) change of MO concentration in solution and (b) change of the total MO concentration in solution and on photocatalyst surface with varied adsorption constant (K), intrinsic reactivity constant (k_s) and overall rate constant (k_f). MO dose (C_{in}), catalyst loading (D), and Freundlich adsorption coefficient (n) used in the simulations were 15 mg/L, 0.15 g/L and 0.287, respectively.

4.6 Photodegradation Kinetics of Experiments and Simulations

Pseudo-first-order rate constants (k_{pfo}) are often calculated to quantitatively assess degradation kinetics. When a compound exists in only one phase and is removed by a first-order reaction in a completely mixed, batch reactor, the decay model can be expressed as $\ln(C/C_0) = -k_{pfo}t$. These rate constants were calculated in order to compare the photoactivity of BiOBr and TBB-0.6 for degradation of RhB and phenol (Figure 28). It is worthy to note that although both BiOBr and TBB-0.6 have negligible adsorption capacity for phenol, TBB-0.6 still outperforms BiOBr in the degradation of this pollutant, with the rate constant for TBB-0.6 being about 2.1 times that for BiOBr. This implies TBB-0.6 might have more active sites on its surface,

because of its larger surface area and it might have more efficient electron-hole separation due to smaller crystallite size.

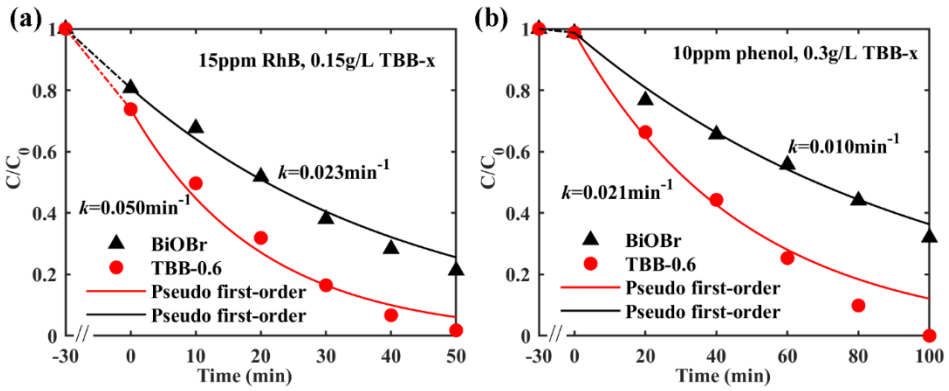

Figure 28. Experimental and fitted photodegradation kinetics of (a) RhB and (b) phenol using BiOBr and TBB-0.6. The rate constants and fittings were derived using the pseudo first-order model. The dose of RhB was 15 mg/L and the concentration of photocatalyst was 0.15 g/L. The dose of phenol was 10 mg/L and the concentration of photocatalyst was 0.3 g/L.

Photodegradation kinetics of MO with the samples are shown in Figure 29. The loading of photocatalysts (0.15 g/L) and MO dose (15 ppm) were carefully chosen to show removal by both adsorption and photocatalytic reaction. As expected, amorphous TiO_2 yielded negligible removal of MO neither by adsorption nor photodegradation. This demonstrates that both adsorption sites and photocatalysis sites are located on BiOBr crystals in the composites, while amorphous TiO_2 serves the role of tailoring BiOBr crystallite size, surface area, and adsorption capacity. TBB-0.6 and TBB-1 removed about 50% of MO from the solution solely by adsorption. After simulated solar irradiation was applied, MO was degraded, and concentrations declined in both the solution phase and the adsorbed phase. Although TiO_2-BiOBr composites achieved higher removals of MO

from the solution phase than BiOBr did, it is difficult to evaluate the extent of MO degradation based on the data presented in Figure 29, because it shows only the MO concentration change in solution and but not the changes of MO in the adsorbed phase.

The kinetic model was also used to describe experimental results of photodegradation of MO. A complete adsorption isotherm was determined only for TBB-0.6 (Figure 26c); however, one data point for adsorption equilibrium for each photocatalyst were obtained in experiments (t = 0 in Figure 29). These data points were used to calculate the values of K for all photocatalysts, assuming that the value of n is the same as for TBB-0.6:

$$K = (C_{in} - C_{t=0}) / (DC_{t=0}^{n}) \tag{7}$$

Values for the rate constants for each photocatalyst were then obtained from nonlinear fitting of the experimental data (shown in Figure 29) using Eq. (6) as the model function and k_f as the coefficient to be estimated. Values of these coefficients are summarized in Table 1. The calculated values of K for TBB-0.6 obtained from Eq. (7) are slightly different from the one obtained from adsorption isotherm (Figure 26c). This is reasonable because the adsorption isotherm gave a value of K that is averaged over a series of MO doses. Numerical simulations were performed with these rate constants and the simulation results were compared with experimental data. Figure 29 shows that experimental data are reasonably well fitted by simulation results, which indicates the suitability of the kinetic model and its rate constants. The overall rate constants (k_f) for TiO_2-BiOBr samples increase with adsorption capacities and are much higher than those for BiOBr, which provides evidence for the adsorption-photocatalysis synergy. The demonstration of the correlation between adsorption and photodegradation indicates the benefits of designing model photocatalysts with tailorable adsorption capacities and comprehensive kinetic modeling. The

calculated intrinsic reactivities (k_s) of TBB-0.4 and TBB-0.6 are slightly smaller than that of BiOBr, possibly because the high levels of MO adsorption block light from illuminating the photocatalysts and some recalcitrant degradation intermediates take up surface active sites. In this circumstance, the calculated intrinsic reactivity depends not only on the activity of the photocatalyst itself but also on the amount of light striking the surface and the availability of surface sites for MO.

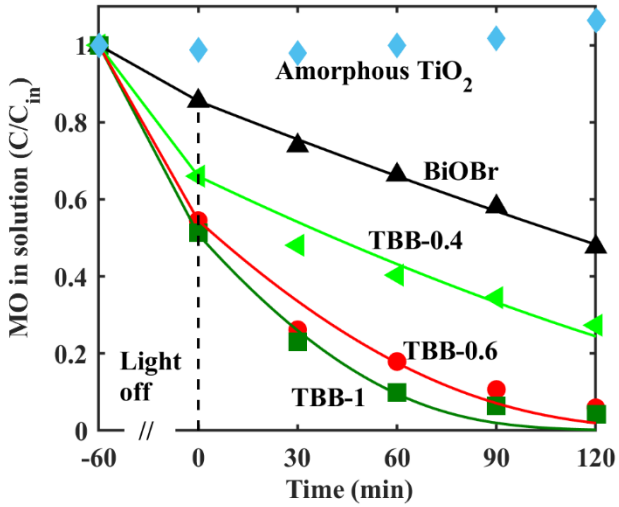

Figure 29. Experimental photodegradation kinetics of different samples and fitted simulation curves. The data of amorphous TO_2 are not fitted.

Table 1. Values of K, k_f, k_s for different photocatalysts that were obtained from nonlinear fitting of experimental data (Figure 29). The value of *n* is 0.287.

Samples	BiOBr	TBB-0.4	TBB-0.6	TBB-1
C_{in} (mg/L)	15	15	15	15
K ($mg^{1-n}L^n/g$)	7.2	16.9	24.9	27.4
k_s (min^{-1})	0.024	0.014	0.021	0.025
k_f ($mg^{1-n}L^n/g/min$)	0.17	0.24	0.52	0.68

4.7 Cycling tests

Cycling performance of TBB-0.6 for the removal of MO, RhB and phenol, as well as BiOBr for the removal of MO were tested. The illumination time for the cycling tests was carefully chosen to enable more than 95% total removal of the target pollutants at the end of the first cycle. As shown in Figure 30b, the adsorption capacity and photoactivity of TBB-0.6 decreased substantially after the first cycle and only 23% overall removal was achieved in the fourth cycles. Though the adsorption capacity of BiOBr also decreased after the first cycle, the photoactivity did not have significant change. The overall removal of MO in the fourth cycle remained more than 95%. This was expected since BiOBr had much lower adsorption capacity than TBB-0.6, thus the effect of intermediates accumulation on BiOBr was not significant. However, the performance drop of TBB-0.6 did not occur with the degradation of RhB and phenol, which indicated that the photoactivity of TBB-0.6 itself was stable under simulated sunlight irradiation. Therefore, high levels of adsorption on TiO_2-BiOBr composites did have pollutants-dependent adverse effects on the recyclability of the photocatalysts that may be caused by the accumulation of MO degradation intermediates on the photocatalyst surface. Since TBB-0.6 has large surface area and high

adsorption for MO, it is possible that it also has high adsorption for the degradation intermediates of MO.

FITR spectra of pristine TBB-0.6, spent TBB-0.6 (after one cycle photodegradation test) and MO were measured to investigate possible MO photodegradation intermediates that were adsorbed on the surface of TBB-0.6. As shown in Figure 31, pristine and spent TBB-0.6 had an absorption band at 1620 cm^{-1} for O–H bending vibrations of chemically adsorbed water and a band at 460 cm^{-1} for Bi-O vibrations. The bands at 1427 and 1369 cm^{-1} of the N=N bond in MO (Figure 30a) were not observed on spent TBB-0.6, indicating that the adsorbed intermediates might not have the azo bond. The bands at 1119 cm^{-1} for S=O stretching vibrations and at 1037 cm^{-1} for C–H stretching vibrations of the benzene ring were observed on spent TBB-0.6. In addition, spent TBB-0.6 had a broad absorption band near 600 cm^{-1} that possibly incorporated C–S stretching vibrations (624 and 563 cm^{-1}) and C–H stretching vibrations (698 cm^{-1}).[110] This FTIR analysis suggests that the adsorbed intermediates probably had sulfonated aromatic rings that are widely regarded as MO photodegradation intermediates in literature.[37, 38, 111] Since considerable studies have shown that aromatic sulfonates have high adsorption at mineral oxide–water interfaces,[112, 113] we think aromatic sulfonates from the photodegradation of MO may have high adsorption on TiO_2-BiOBr composites, which impedes the adsorption and photodegradation of MO on the photocatalyst surface. However, to gain clear understanding of the adverse effects brought by the intermediates, the sorption affinities of the intermediates need further investigation. The photodegradation of RhB is reported to follow the N-deethylation, chromophore cleavage, ring opening and mineralization paths, producing more types of possible intermediates.[114, 115] Aromatic carboxylic acids, like benzoic, salicylic and phthalic acids, are a major type of RhB degradation intermediates and have varied adsorption affinities on metal oxides,[114, 116] but it

has been revealed that BiOBr has unique ability for decarboxylation.[117] This may explain that TBB-0.6 showed good recyclability for RhB degradation, but further study is required.

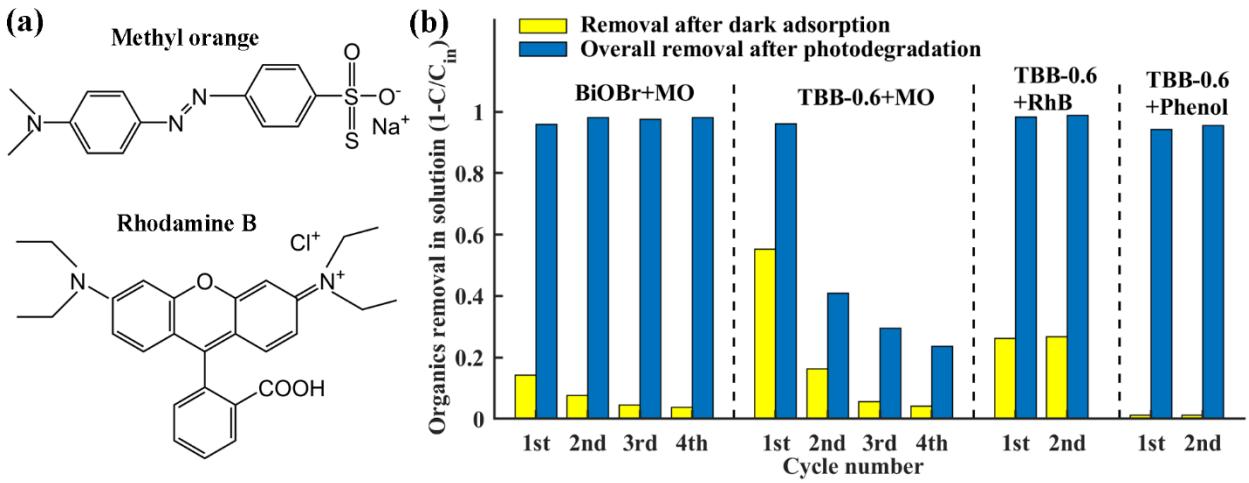

Figure 30. (a) The molecular structures of methyl orange and rhodamine B; (b) cycling performance of TBB-0.6 for the removal of MO (15 mg/L, 150 min illumination), RhB (15 mg/L, 180 min) and phenol (10 mg/L, 90min), as well as BiOBr for the removal of MO (15 mg/L, 300 min) were tested. The illumination time for the cycling tests were carefully chosen to enable more than 95% total removal of the target pollutants at the end of the first cycle.

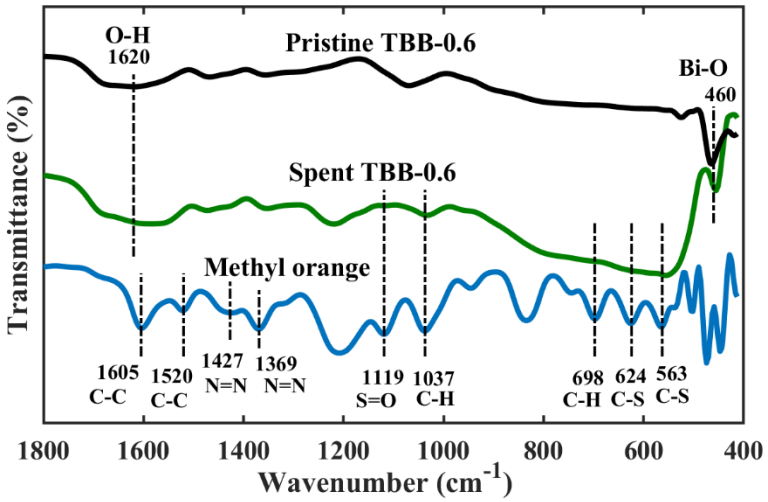

Figure 31. FTIR spectra of MO, pristine TBB-0.6 and spent TBB-0.6 (after one cycle photodegradation test).

4.8 Conclusion

This study synthesized TiO_2(amorphous)-BiOBr microspheres through a one-pot solvothermal process. BiOBr provided adsorption sites and photocatalysis sites, while amorphous TiO_2 was uniformly distributed in BiOBr microplates and tailored the size of BiOBr crystallites, surface area and adsorption capacity for MO. The composites with varied adsorption capacities were used to investigate the adsorption-photocatalysis synergy. Furthermore, kinetic modeling that combines adsorption with photocatalysis was developed to aid this investigation and to evaluate photocatalysts with high levels of adsorption. Both experiments and kinetic modeling proved that adsorption promoted photodegradation, however, it was also found that high levels of adsorption might have pollutant-dependent adverse effects on recyclability of TiO_2-BiOBr composites. In summary, this study has 1) designed model photocatalysts with tailorable adsorption capacities to study the adsorption-photocatalysis synergy; 2) combined experiments and kinetic modeling to

provide a useful approach to elucidate the synergy and quantitatively evaluate the photocatalysts; 3) implicated the necessity of examing the recyclability of photocatalysts that have high levels of adsorption.

CHAPTER 5

EFFICIENT OIL/WATER SEPARATION BY A DURABLE UNDERWATER SUPEROLEOPHOBIC MESH MEMBRANE WITH TIO_2 COATING VIA BIOMINERALIZATION[4]

5.1 Background and Hypothesis

Oil/water separation is important in treating industrial oily wastewater and rapidly responding to oil spills. Membrane technology is attractive for oil/water separation because it works without chemicals addition, with undemanding operations, and it can achieve high separation efficiency and speed if the surface wettability of the membranes is well designed.[40] Typically, surface wettability of membranes for oil/water separation can be categorized to two types: hydrophilic/oleophobic surfaces that are permeable to water but impermeable to oils, and oleophilic/hydrophobic surfaces that are permeable to oils but impermeable to water. By achieving an appropriate combination of surface energy and surface roughness, desirable surface wettability can be procured.[41] Therefore, surface modification of membranes is deemed a fundamental but powerful approach to engineer surface wettability.[42]

Applying coatings on membranes is widely used to modify membrane surface wettability. Stainless steel mesh (SSM) is a type of low-cost and chemically stable porous membrane. It has better thermal durability than polymer membrane and superior mechanical properties comparing to ceramic membranes, but pristine SSM cannot separate oil/water mixtures because its surface is both hydrophobic and underwater oleophobic. Therefore, suitable surface coatings are necessary

[4] Part of this chapter is reprinted with permission from "Efficient Oil/Water Separation by A Durable Underwater Superoleophobic Mesh Membrane with TiO2 Coating Via Biomineralization" by Deng, Wei, Chao Li, Fuping Pan, and Ying Li, 2019. Separation and Purification Technology, 222, 35-44. Copyright [2019] by Elsevier B.V.

to prepare SSM for oil/water separation. A wide range of materials have been studied as coating materials on SSM to engineer surface wettability. Polymers have been extensively researched as coating materials on SSM as polymers have good chemical stability and are easy to construct microstructures.[45-50, 118-120] Inorganic materials, with good thermal and mechanical properties, are deemed promising candidate coating materials. Stainless steel meshes coated with boron nitride nanotubes,[121] ZnO nanowires,[61, 62] silica nanoparticles,[57, 58] zeolite films,[59, 60] Cu microflakes,[122] and graphene oxide[123] have been developed for oil/water separation. TiO_2 has also attracted specific research interest as a coating material to equip substrates with hydrophilicity and oleophobicity, because it is inexpensive, nontoxic, and has good thermal, chemical and mechanical stability. Various TiO_2 nanostructures, such as nanoparticles, nanotubes, nanofibers, and nanowires, have been used to construct coatings on meshes and membranes for oil/water separation purpose and the factors governing the separation process have been investigated.[52-55, 124] However, these reported surface coatings require complex coating procedures or precursor preparation processes, such as long-time hydrothermal process and spray/dip-coating followed by calcination, that are often chemically, energetically and operationally intensive. For example, reported coating methods for TiO_2 are limited to spray or dip coating using sols made from either TiO_2 nanostructures or titanium precursors. In these methods, preparation of the stable sols is usually time-consuming and post-annealing at high temperatures is required. Moreover, some of these coatings are not chemically and mechanically durable. For example, ZnO is naturally not stable in acidic or basic environment (pH less than 5 or greater than 11);[125] Cu is readily oxidized in air; and resistance to mechanical wear, such as abrasion, of these prepared meshes and membranes was rarely studied. Therefore, research on

coating materials and methods is still in great need to facilely prepare durable superwetting membranes.

Biomineralization is a biomimetic synthesis process that has emerged as a promising method to synthesize metal oxides such as TiO_2 as it generally attains a high-yield mineral product in a cost-effective, energy-efficient, and environmentally benign manner.[126, 127] This process makes use of the hydrolysis and condensation of water-soluble titanium precursor to produce TiO_2, catalyzed by amino group-rich chemicals.[126] The process involves only two precursors reacting in aqueous solutions at environmentally benign conditions: neutral pH, ambient temperature and pressure, and no hazardous materials, like concentrated acids and explosive chemicals, are involved. These features make the approach a facile and scalable synthesis approach. A large number of TiO_2 and TiO_2-based materials have been synthesized by biomineralization and applied for photocatalytic,[126-130] electrochemical,[131-134] and sensing applications.[135, 136] However, no study has been reported on applying this biomineralization approach in preparing TiO_2 coatings on meshes or membranes for engineering surface wettability and for oily wastewater treatment.

Because of these eminent advantages, biomineralization may be a suitable process for coating TiO_2 on SSM to endow the surface with hydrophilicity and oleophobicity. In this work, we prepared TiO_2-coated SSM (TSSM) via a biomineralization approach and studied its surface wettability, separation capacity (flux and efficiency), anti-fouling capability, and durability under chemically, thermally and mechanically harsh conditions. We also extended the developed coating route to apply TiO_2 coatings on other substrates, including nonwoven SSM, cellulose filter paper, and PVDF membrane for oil/water separation. The proof-of concept studies in this work suggest

the potential applicability of the biomineralization-enabled TiO_2-coating method and the facilely fabricated durable TSSM for oil/water separation and oil-spill cleanup.

5.2 Experimental Details

Typically, 5 pieces of SSM (30 mm × 30 mm) were precleaned by sonication in ethanol for 10 min and UV/Ozone treatment for 15 min (UV/Ozone ProCleaner, Nanosciences). The precleaned meshes were put in a 15 mL PEI solution (20g/L, pH=7) for 5 min to allow the adsorption of PEI molecules on SSM surface. The meshes were then rinsed with deionized water and put in a 15 mL Ti-BALDH solution (20 g/L) for another 5 min, during which PEI molecules reacted with Ti-BALDH molecules through nucleophilic substitution initiated polycondensation and produced TiO_2 on the surface of SSM. The PEI and Ti-BALDH solutions were shaken at 300 RPM (Mini Shaker, VWR International) while the meshes were immersed in the solutions to make uniform reactions on the mesh surface. The TiO_2-coated meshes were then rinsed with deionized water and dried. The coating process was repeated by desired cycles and the TiO_2-coated SSM was labelled as TSSM. TiO_2-coating on nonwoven SSM and filter paper were carried out using the same approach, while the coating process for PVDF membrane was modified. Since the PVDF membrane is hydrophobic, isopropanol (IPA) was used to prepare the solutions of PEI and Ti-BALDH, and the two solutions were sonicated during the biomineralization process.

Oil content in permeate was obtained by measuring the total organic carbon (TOC) level on a TOC analyzer (TOC5000A, Shimadzu). Microscopic images of water droplets (3 μL) and oil droplets (3 μL, dyed as red using oil red) on meshes and membranes were obtained by a USB digital microscope (200 × magnification, Jiusion). Water contact angles (WCA) and underwater

oil contact angles (OCA) were then calculated from the images using ImageJ (National Institutes of Health, USA) with a drop analysis plugin, LB-ADSA.[137] Each measurement was repeated by three times. Separation experiments of oil/water mixtures: the coated-mesh/membranes with a diameter of 20 mm were fixed between two plastic tubes using a 3D printed fixture. 40 mL immiscible oil/water mixtures (50 v/v%) were poured onto the mesh and separation was achieved by the force of gravity. The TiO_2-coated PVDF membrane was used for the separation of oil/emulsions (2000 ppm petroleum in water, prepared by a mechanical blender) assisted by vacuum filtration. During separation, the bottom plastic tube of the setup was connected to a vacuum port.

The anti-fouling capability was explored via cycling test. In each cycle, 40 mL petroleum/water mixture (v:v=1:1) was used as the feed solution. The cycling test was carried out continuously and no cleaning treatment of TSSM was employed between cycles.

Calcined TSSM was obtained by calcining TSSM at 450 ºC for 2 h and sonicated TSSM was obtained by sonicating TSSM in deionized water for 1 h (Ultrasonic Bath, Branson). Crumpled TSSM was obtained by folding TSSM and unfolding it using hand. Abrasion test of TSSM was performed on an 800-grit sandpaper (silicon carbide, McMaster-Carr) as illustrated in Figure 32. The load was 350 g on a 30 mm × 30 mm TSSM, which equals to a pressure of 3.8 kPa. The abrasion length was 2 m in total: 1) 0.1 m along longitudinal direction; 0.1 m along the direction opposite to that in 1); 3) 0.1 m along transverse direction; and 4) 0.1 m along the direction opposite to that in 3); these 4 steps were repeated by 5 times. To test the chemical resistance, 4 pieces of TSSM were immersed in solutions of 0.1 M HCl, 0.1 M NaOH, 1 M NaCl, and ethanol for 24 h, respectively. Then the TSSMs were washed, dried and compared with pristine TSSM in terms of hydrophilicity and oleophobicity. In addition, to demonstrate the potential of TSSM for separation

oil/water mixtures of high salinity, acidity, and alkalinity, the oleophobicity of TSSM in solutions with varied NaCl concentrations and in solutions with varied pH was measured.

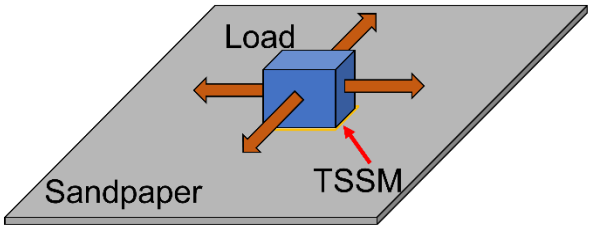

Figure 32. Schematic diagram of the abrasion test.

5.3 Characterization Results

The surface compositions and chemical states of SSM and four-cycle-coated TSSM were investigated by XPS. The survey spectra (Figure 33a) prove the existence of Fe in SSM and Ti in TSSM. The Ti 2p spectra of TSSM (Figure 33b) are well resolved into two spin orbit components at binding energies at 458.4 eV and 464.1 eV that are attributed to Ti $2p_{3/2}$ and Ti $2p_{1/2}$, respectively. XRD testing shows that SSM and TSSM have almost identical spectra and no characteristic peaks of crystalline TiO_2 were detected (Figure 34). Therefore, it is affirmed that titanium exists in the samples as Ti^{4+} and the formed TiO_2 is in amorphous phase as generally reported from the biomineralization approach.[128, 129, 133] N was also detected in TSSM and two splitting peaks at 399.0 eV and 401.5 eV could be assigned to secondary amino and tertiary amino groups that are from PEI.[129, 138, 139] Fe spectra of SSM are deconvoluted to two major peaks at 710.4 eV and 724.1 eV for Fe $2p_{3/2}$ and Fe $2p_{1/2}$ from Fe_2O_3, one small peak at 706.4 eV for Fe $2p_{3/2}$ from iron metal, and another small peak at 719.1 eV that is probably a satellite peak

of the main $2p_{3/2}$ peak.[140] Fe was not detected in TSSM because the detection depth of XPS is just few nanometers, which confirms that the mesh surface was fully covered by TiO_2-coating.

It is clearly shown in Figure 35a and b that the pristine SSM is woven by smooth-surface wires with a diameter of 25 μm using the Twill Dutch weave style and the opening diameter is about 5 μm. As seen in the high magnification images (Figure 35c), densely aggregated particles with size around 20 nm are observed and are possibly Fe_2O_3 particles as indicated by XPS analysis. Interestingly, four cycles of TiO_2 coating did not lead to distinguishable morphology change even in high magnification SEM image (Figure 35d-f), indicating the roughness change caused by TiO_2 coating is not evident. The surface of the stainless steel wires kept smooth both before and after TiO_2-coating. EDS element mappings (Figure 35g-i) indicate the uniform distribution of Ti on the mesh surface, while Ti was not detected on pristine SSM (Figure 36). The weight ratio of Ti derived from EDS spectra is 0.29 wt%; however, considering that the detection depth of EDS is just few micrometers, the weight ratio of TiO_2 in the mesh should be much lower than 0.29 %. Approximate calculations were carried out to estimate the thickness, based on the measured relative content of Ti (or Ti/Fe ratio) from top-view EDX analysis and the geometrical relations between the TiO_2 layer and mesh wire. The following equation was used:

$$\frac{[(d_{ssm}+2t_{TiO_2})^2-d_{ssm}^2]\rho_{TiO_2}}{[d_{ssm}{}^2-(d_{ssm}-2t_{detection})^2]\rho_{ssm}}=\frac{m_{TiO_2}}{m_{ssm}}.$$

Where $d_{ssm}=25\mu m$ is the diameter of SSM wire, t_{TiO_2} is the thickness of TiO_2 layer, $\rho_{TiO_2}=4200\,kg/m^3$ is the density of TiO_2, $t_{depth}=2\mu m$ is the estimated detection depth of EDS at 20 kV,[141] $\rho_{ssm}=7700\,kg/m^3$ is the density of stainless steel, and

$\frac{m_{TiO_2}}{m_{ssm}} = \frac{0.29 \times (47.9 + 32) / 47.9}{100} = 0.0048$. The thickness of four cycles of TiO_2-coating was estimated to be around 16 nm, which is very thin compared to the size of SSM wire. Fe was detected in TSSM by EDX since the detection depth of EDS is bout several micrometers. In addition, TSSM has lightly darker color than SSM but no other visible change was observed. C, Cr, and Mn of high contents were also detected, and they may also affect surface wettability of SSM, which however will not change the conclusion of study that focuses on the difference between SSM and TSSM. It is concluded that a uniform, thin and smooth TiO_2 layer was conformally coated on SSM via the biomineralization approach.

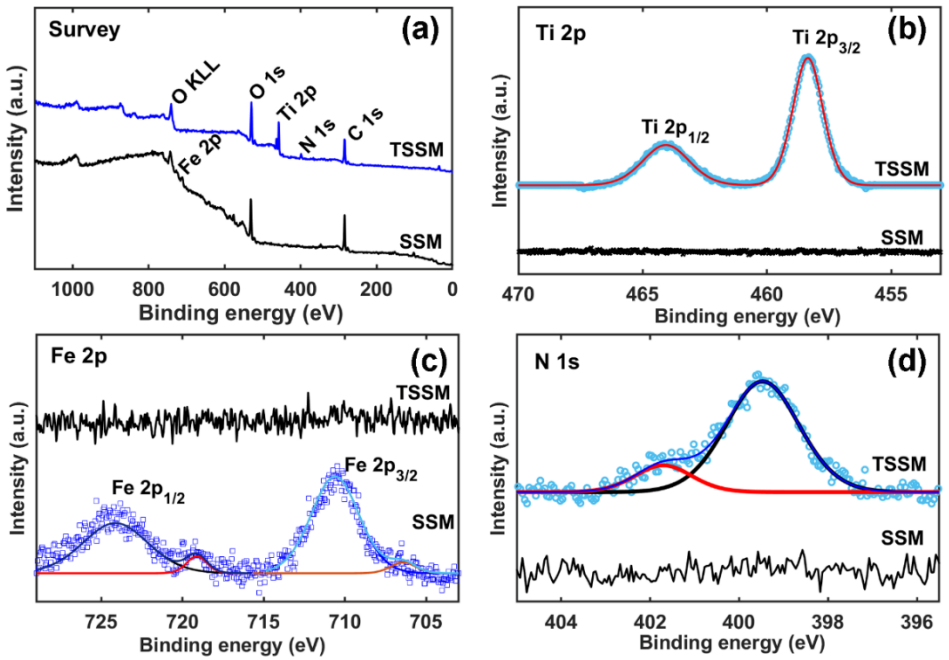

Figure 33. XPS spectra of SSM and TSSM with four coating cycles: (a) survey, (b) Fe 2p, (c) Ti 2p and (d) N 1s.

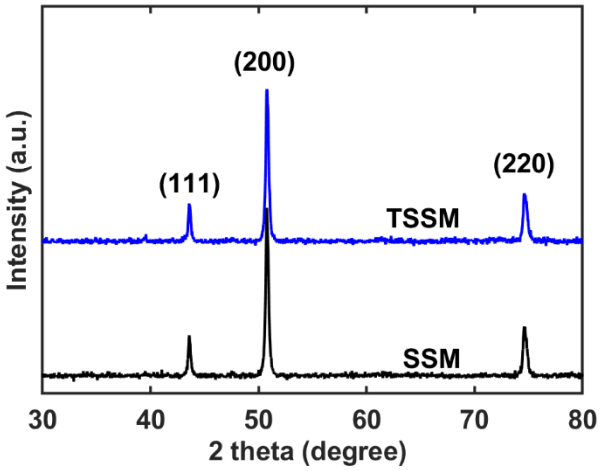

Figure 34**.** XRD spectra of SSM and four-cycle-coated TSSM.

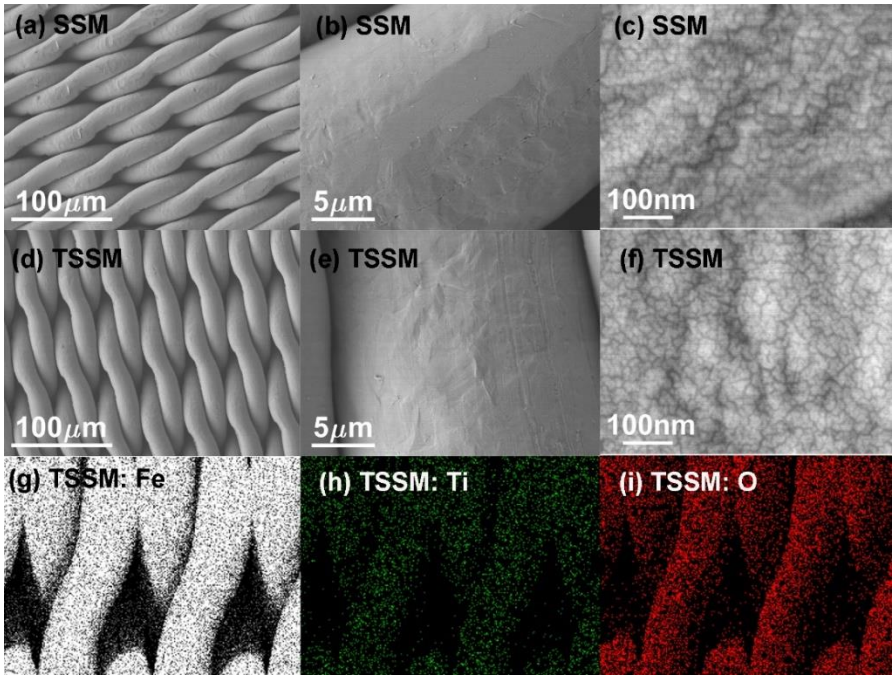

Figure 35. SEM images of (a, b, c) SSM and (d, e, f) four-cycle-coated TSSM, as well as (g, h, i) EDX mapping of the TSSM.

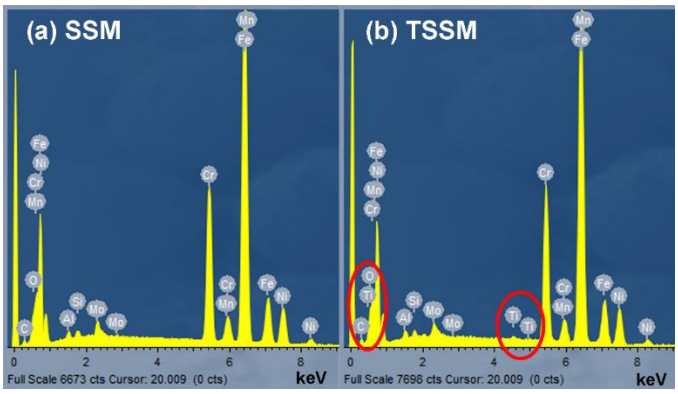

Figure 36. EDS spectra of (a) SSM and (b) TSSM.

5.4 Proposed coating process

Reviewing the reported mechanism of biomineralization,[126, 133, 142, 143] we propose that the biomineralization-enabled TiO_2-coating on SSM follows a layer-by-layer manner and the coating process is illustrated in Figure 37. First, PEI molecules are adsorbed on the surface of SSM; then the positively charged PEI molecules on the SSM surface adsorb and concentrate negatively charged titanium precursor (Ti-BALDH molecules) via electrostatic and hydrogen bonding interactions; when PEI molecules and Ti-BALDH molecules are in close proximity, hydrogen bonding between Ti-OH of Ti-BALDH molecules and N-H of PEI molecules initiates nucleophilic substitution of a Ti-O oxygen atom on another adjacent titanium atom; as the process proceeds, polycondensation reaction occurs subsequently to produce TiO_2. Since the pristine SSM is hydrophobic and has smooth surface and relatively simple porous structure, TiO_2 is coated on the surface as a uniform and thin layer, with no aggregated nanoparticles observed. This approach needs only two simple steps, i.e., dipping the substrate in PEI solution and dipping PEI-adsorbed substrate in Ti-BALDH solution, and the process proceeds at environmentally benign conditions, making it a facile and scalable approach for uniform and thin TiO_2 coating on SSM.

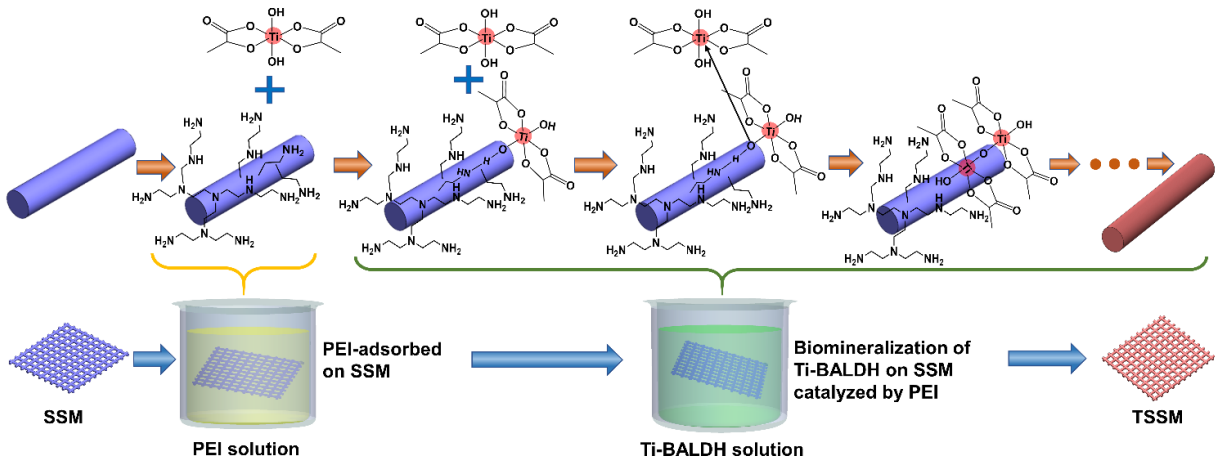

Figure 37. Schematic illustration of the biomineralization process of Ti-BALDH catalyzed by PEI for TiO_2-coating on stainless steel mesh. The representative reactions were illustrated on one single mesh wire and the typical experimental coating process was shown at the bottom.

5.5 Surface Wettability testing

Hydrophilicity and oleophobicity, representing the affinity to water and repellence to oil, are essential for a mesh to be applicable for oil/water separation. These two properties were characterized by water contact angle (WCA) in air and underwater oil contact angle (OCA). As indicated in Figure 38a and Figure 39a, the pristine mesh was hydrophobic with a WCA of 120º and oleophobic with an OCA of 115º. This suggests that the pristine mesh could not separate oil/water mixture since it would retain both water and oil. Nevertheless, the surface wettability was effectively remedied by TiO_2 coating that improved both surface hydrophilicity and underwater oleophobicity. With two or more coating cycles, WCA was reduced to 0º (Figure 39) and OCA was increased to around 160º, which proved that a few coating cycles of TiO_2 could make the mesh surface superhydrophilic and underwater superoleophobic. Therefore, TiO_2-

coating by the biomineralization approach built up the required surface wettability for oil/water separation. We also noted that the coated meshes with three, four and five cycles of coating have almost the same water fluxes during oil/water separation (Figure 39c). To reduce the experimental uncertainties caused by undercoating or overcoating, TSSM with four coating cycles was used for followed experiments. Besides dichloroethane, TiO_2 coating also enhanced the repellence to other types of oil, including hexadecane, paraffin oil, petroleum oil, and soybean oil (Figure 40). Compared with the pristine mesh that has OCAs ranging from 40º to 115º for the tested oils, TSSM is superoleophobic to all these oils since the OCAs are around 160º. As the biomineralization approach gives smooth, uniform, and conformal TiO_2 coating on the mesh, the change of surface wettability brought by TiO2 coating should mainly be attributed to the altered surface energy, instead of surface roughness change. Benefiting from the superhydrophilic and superoleophobic properties, it is feasible to use TSSM for the separation of various oil/water mixtures.

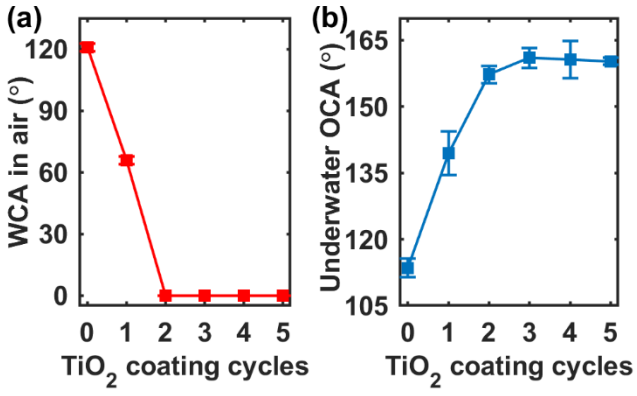

Figure 38. (a) water contact angles (WCA) in air and (b) underwater oil contact angles (OCA) of SSM and TSSM with different cycles of TiO_2 coating. The oil droplets used in the measurements were 3.0 µL dichloroethane droplets.

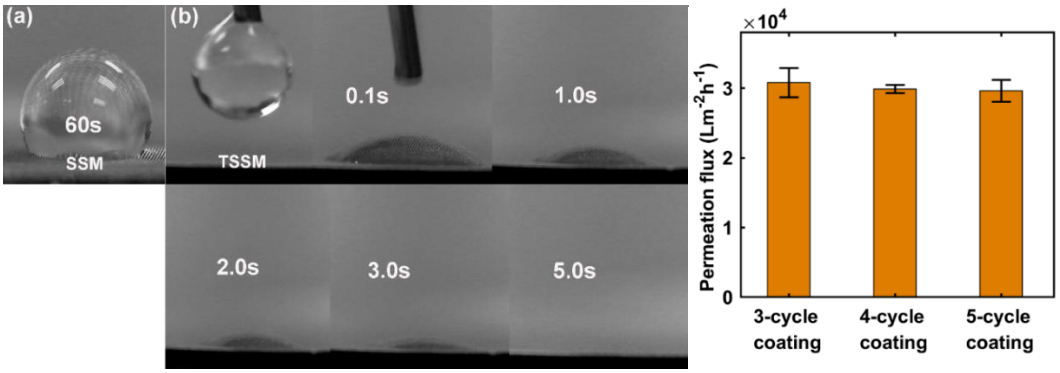

Figure 39**.** Wetting behavior of water on (a) SSM, (b) four-cycle-coated TSSM, and (c) water fluxes in the separation of petroleum/water mixtures (v:v=1:1) using the meshes with three, four and five cycles of TiO_2 coating.

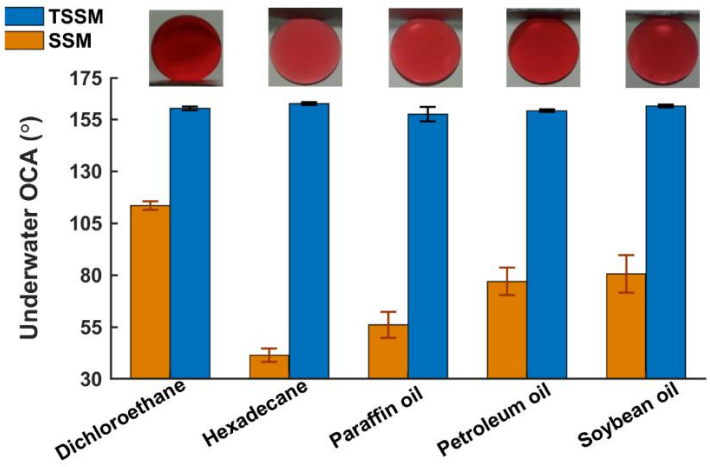

Figure 40. Underwater oil contact angles (OCA) of different types of oil on four-cycle-coated TSSM. The insert pictures are microscopic images of corresponding oil droplets (3.0 μL) on the TSSM.

5.6 Separation of immiscible oil/water mixtures

The separation capability of TSSM for immiscible oil/water mixtures was evaluated using the apparatus where a piece of TSSM (diameter: 20 mm) was fixed between the two tubes (Figure 41). A 40 ml oil/water mixture (v:v=1:1) was poured onto the top tube. Water quickly passed through the coated mesh solely driven by gravity while oil stayed on top of it (Figure 41a-c). Therefore, the mixture was efficiently separated without external energy input. To quantitatively evaluate the separation performance, separation flux and oil content in permeate for three types of oil/water mixtures were measured and are presented in Figure 41d. A flux around 3×10^4 L m^{-2} h^{-1} was achieved for separation of petroleum/water mixture and fluxes about 2.5×10^4 L m^{-2} h^{-1} were also achieved for hexadecane/water and paraffin oil/water mixtures. The high fluxes on TSSM are mainly attributed to the large pores and surface superhydrophilicity/superoleophobicity of TSSM. Oil content in the permeates was below 8 ppm, corresponding to an oil rejection rate that is about 99.999%. This excellent oil rejection capability manifests the benefits of surface superwettability of TSSM.

In addition, to demonstrate the anti-fouling capability and feasibility for long-term use, cycling tests of TSSM were performed. In each cycle, a 40 ml petroleum/water mixture (v:v=1:1) was used as the feed. After one cycle of separation was done, oil was poured out and the second cycle begun with another 40 ml mixture. This process was repeated for 36 times and no cleaning action on TSSM was taken between the cycles. The flux of each cycle and oil content in permeate of every 6 cycles were recorded and displayed in Figure 41e. It's clearly shown that the separation flux and separation efficiency did not decline over the cycles. The flux stayed around 3×10^4 L m^{-2} h^{-1} and the oil content in permeate fluctuated slightly but kept below 8 ppm. Moreover, TSSM

maintained its separation capability after being stored in water for four months, as shown in Figure 41e. This demonstrates that TSSM has prominent resistance to oil-fouling and long-term stability and it can be attributed to the excellent underwater superoleophobicity of TSSM that has low affinity to oils, good durability of TiO_2 coating, as well as the smooth surface of TSSM that may be less likely to mechanically trap oils, comparing to rough surfaces that have micro/nanostructures, such as nanorods and nanofibers.[47, 61, 62] [6, 14, 15]. These results emphasize the advantages of smooth and uniform coating via the biomineralization approach where superwettability is solely engineered by surface energy modification while surface roughness is not altered. Therefore, TSSM is suitable for long-term use in oil/water separation.

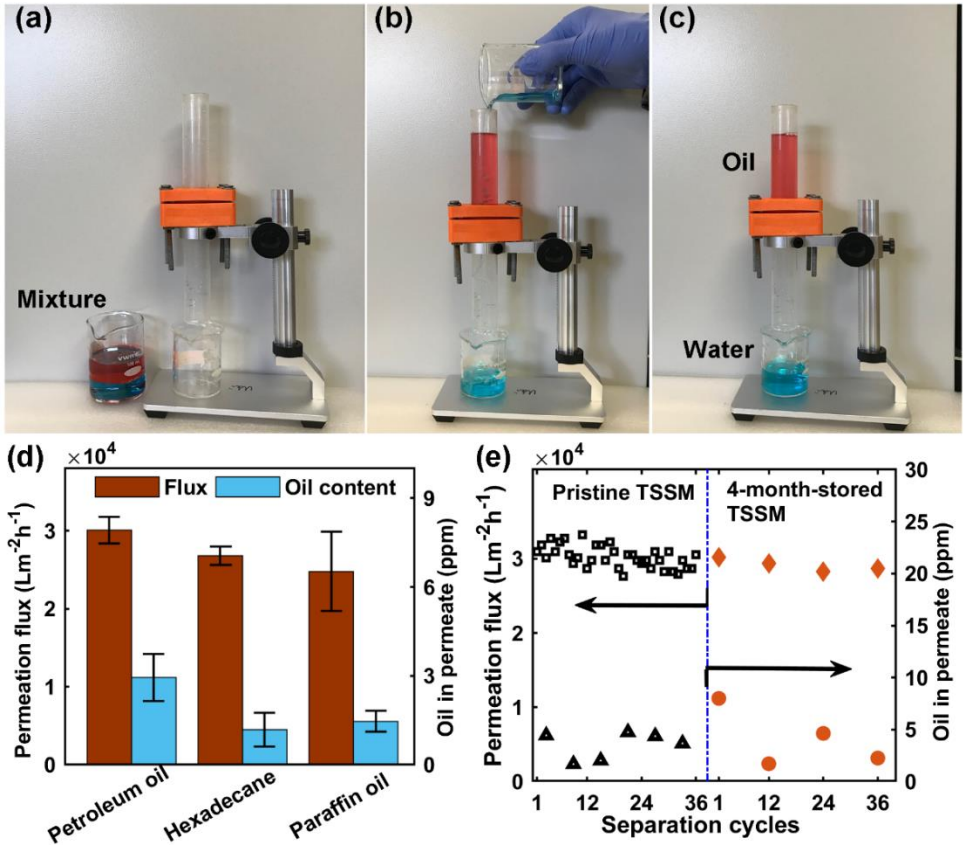

Figure 41. Photographs of the separation apparatus and gravity-driven separation process of petroleum/water (v:v=1:1) mixture: (a) before separation, (b) during separation and (c) after separation; oil was dyed as red and water was dyed as blue; (d) permeation fluxes and oil contents in permeates for the separation of the three mixtures , and (e) anti-fouling and long-term stability tests using petroleum-water mixtures (v:v=1:1). The 4-month-stored TSSM was prepared by immersing a piece of TSSM in water for four months.

5.7 Durability test

Oily wastewaters from industry and oil spills in ocean usually have complex compositions and chemical properties, like high salinity, strong acidity and alkalinity, which may modify the

interfacial energies of mesh–water and oil-water interfaces, and hence modify oil repellence of the meshes. To investigate this potential effect, the OCA of TSSM was measured under water of varied NaCl concentrations and pH. Results in Figure 42a show that pH did not affect OCA notably and high salinity increased OCA, possibly via modifying the interfacial energies. These results indicate that the high salinity, acidity and alkalinity have no adverse effects on the surface oleophobicity and separation functionality of TSSM. In addition, to understand whether the surface wettability is stable in chemical solutions, TSSM was immersed in different solutions, including 0.1 M HCl, 0.1 M NaOH, 1 M NaCl solutions, and absolute ethanol, for 24 h and then washed and dried. Surface wettability of the treated TSSM was tested. The results are displayed in Figure 42b, where no significant change of OCA occurred. This sturdy oil repellent capability of TSSM demonstrates that TSSM is stable in chemically harsh conditions in terms of surface wettability. In addition, electrochemical Tafel analyses shown in Figure 43 indicate that TSSM may have improved corrosion resistance than SSM, because the corrosion potential (Ecorr) of TSSM (−0.23 V) is higher than that of SSM (−0.25 V). Though the corrosion current (Icorr) of TSSM, 97.9 nA, is slightly larger than that of SSM, 83.1 nA, it is possibly because TSSM is much more hydrophilic than SSM and has a larger surface area in contact with the corrosion solution. Thus, uniform and conformal TiO2-coating not only is not stable in chemically harsh conditions but also improves the stability of the mesh. In summary, TSSM has good stability in chemically harsh conditions and stable oleophobicity under water with high salinity, acidity and alkalinity, which is beneficial for the long-term operation in chemically harsh conditions.

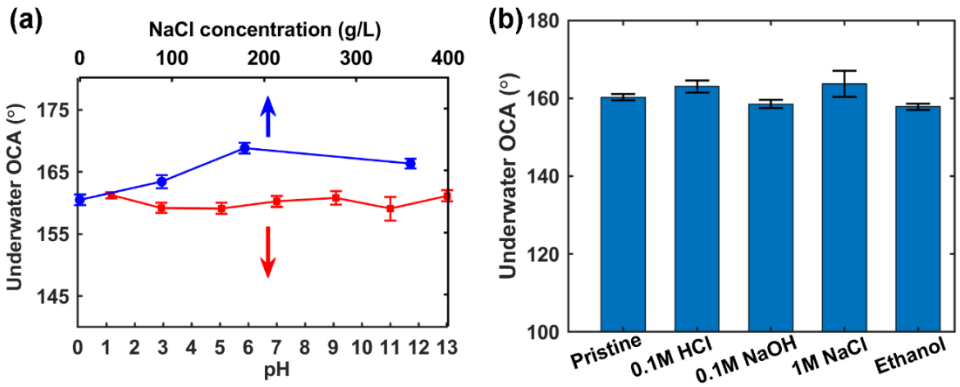

Figure 42. (a) Underwater oil contact angles (OCA) of TSSM measured under water of different pH and salinity; (b) underwater OCA of TSSM after immersion in different solutions for 24 h; TSSM was immersed in the solutions and then washed and dried before measuring OCA in deionized water. Dichloroethane was used as the oil.

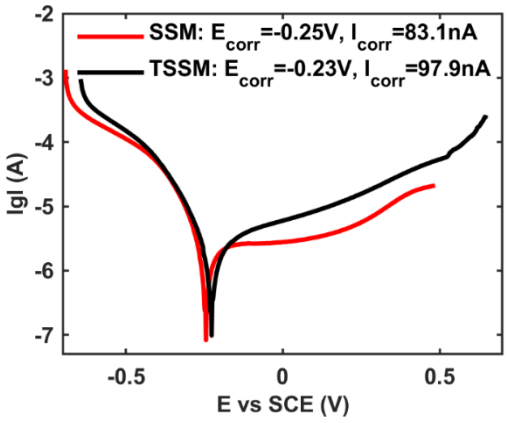

Figure 43. Tafel polarization plots of uncoated stainless steel mesh (SSM) and TiO_2-coated stainless steel mesh (TSSM).

Thermal stability and resistance to mechanical wear are other aspects to evaluate the durability of meshes with surface coatings. To explore the durability of our TSSM prepared via the biomineralization approach, calcination, sonication, abrasion and crumpling tests, were carried

out. The oleophobicity and oil/water separation capability of the worn TSSM were then characterized, and the results are shown in Figure 44. Calcination at 450 °C for 2 h and sonication for 1 h did not undermine the oleophobicity and separation capability of TSSM, suggesting that TiO_2 was firmly coated on the mesh. As exhibited in Figure 45d–f, calcination at 450 °C for 2 h did not cause any crack or peeling-off on the surface, and the surface morphology of calcined TSSM was similar to that of calcined SSM (Figure 45a-c). Abrasion at a load of 350 g for 2 m severely damaged the surface structure of the mesh (Figure 46) and consequently, OCA dropped down about 17°. Nevertheless, the abraded TSSM still had good oil rejection capability. The oil content in the permeate was 2.7 ppm, close to that achieved on the pristine TSSM. This is possibly because abrasion only damaged the top surface of TSSM while the pore structure and TiO_2-coating on the inner pores are still intact after abrasion. The decrease of separation flux should be caused by the increased resistance for water passing through the mesh because the TSSM with reduced oleophobicity tended to have an oil film barrier formed on the surface. Crumpled TSSM (Figure 47) maintained good oleophobicity and separation flux, but oil rejection ability was impaired. This can be explained as follows. During crumpling, TiO_2 on the surface was not damaged, but the pore structure in the crumpled area might be altered. The size of some pores became larger and some smaller. The enlarged pores could allow a certain amount of oils to pass through the mesh and therefore increased the oil content in permeate. But it should be noted that even TSSM was crumpled the oil content was still at a low level (10.7 ppm). Therefore, the biomineralization approach derived TSSM, in terms of both the mesh itself and TiO_2-coating, is durable and has good thermal stability, as well as good stability in chemically and mechanical harsh conditions. This implies the as-prepared TSSM is a promising candidate for oil/water separation applications under harsh conditions.

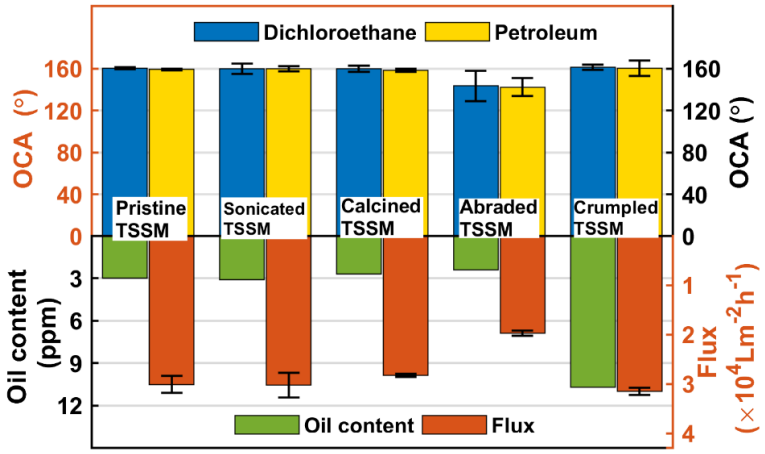

Figure 44. Underwater oleophobicity and oil/water separation capability of pristine TSSM and TSSM after thermal treatment and mechanical wear tests. Oleophobicity was characterized by underwater contact angles of dichloroethane and petroleum droplets on the meshes. Petroleum-water mixtures (v:v=1:1) were used for the separation experiments.

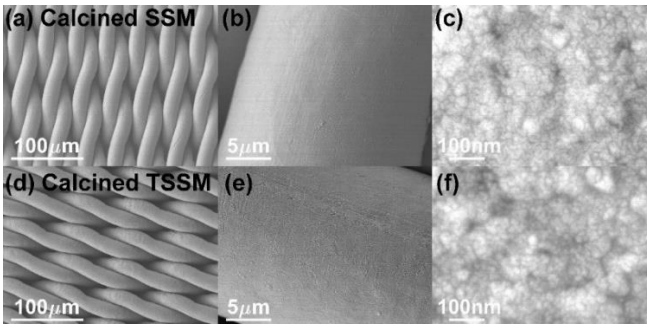

Figure 45. SEM images of (a, b, c) calcined SSM and (d, e, f) calcined TSSM.

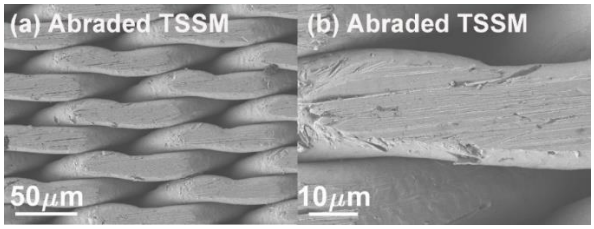

Figure 46. SEM images of abraded TSSM.

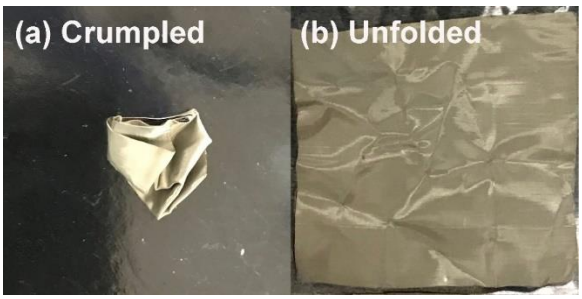

Figure 47. Photographs of the crumpled TSSM and unfolded TSSM after crumpling.

5.8 Biomineralization-enabled TiO_2 coating on other substrates

We have also applied the biomineralization approach to other substrates: nonwoven stainless steel mesh, cellulose filter paper, and PVDF membrane. We found that after TiO_2-coaitng, all these mesh/membranes possessed superhydrophilicity and underwater superoleophobicity (Table 2). Specifically, both TiO_2-coated nonwoven stainless steel mesh (Nonwoven TSSM) and TiO_2-coated filter paper had underwater OCAs of about 160° for dichloroethane and petroleum, and good oil rejection capability. Oil content in permeate was lower than 10 ppm. The separation flux of coated filter paper was much smaller than that of TSSM and nonwoven TSSM because the filter paper had more complicated multiple-layer porous structure (Figure 48c and d). As the separation of oil/water emulsions is more challenging than separation of immiscible oil/water mixtures, stainless steel meshes with relatively large pore size and simple porous structure are not suitable for treating oil/water emulsions. Instead, we used TiO_2-coated PVDF membrane for vacuum-assisted separation of 2000 ppm petroleum in water emulsions because TiO_2-PVDF membranes have finer porous structure and smaller pore size than stainless steel mesh,[144] as well as nanoparticles-constructed rough surface and underwater

superoleophobicity obtained from TiO_2 coating (Figure 49a–c). As displayed in Figure 49 d, the original emulsion was white and opaque, while the permeate was transparent and clear. According to TOC test, only 0.7 ppm oil was left in the permeated water after separation and the corresponding separation efficiency was about 99.97%, suggesting that the TiO_2-coated PVDF membrane possessed prominent oil rejection ability for oil/water emulsion. Therefore, the biomineralization approach is versatile to enable TiO_2 coating on various mesh/membranes for oily wastewater treatment. It is interesting to note that for substrates that are hydrophilic and have rough surface and complex pore structures, like cellulose filter paper (Figure 48c and d) and PVDF membrane (Figure 49a), the TiO_2 coatings are not so smooth as formed on SSM but rough with observable nanoparticles aggregation. We think that the coating morphology is mainly determined by the porous structure, surface wettability and roughness of the substrates that are to be coated.

Table 2. Oleophobicity and oil/water (immiscible petroleum/water mixtures) separation capability of Pristine TSSM, TiO_2-coated nonwoven stainless steel mesh (Nonwoven TSSM) and TiO_2-coated filter paper. TiO_2 coating was prepared by the developed biomineralization approach.

	OCA of dichloroethane (°)	OCA of petroleum (°)	Oil content (ppm)	Flux ($\times 10^4 \cdot Lm^{-2} h^{-1}$)
Pristine TSSM	160.3±0.9	159.2± 0.6	3.0	3.01±0.17
Nonwoven TSSM	161.7±4.9	158.5±3.5	0.8	6.89±0.31
TiO_2-filter paper	163.0±1.7	167.9±1.1	9.7	0.07±0.01

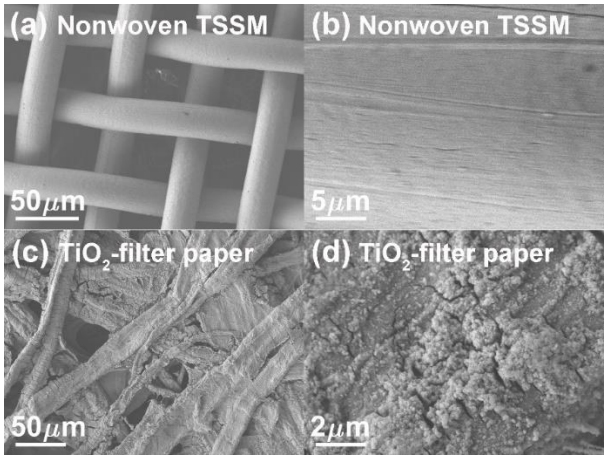

Figure 48. SEM images of (a, b) TiO_2-coated nonwoven stainless steel mesh (Nonwoven TSSM) and (c, d) TiO_2-coated cellulose filter paper.

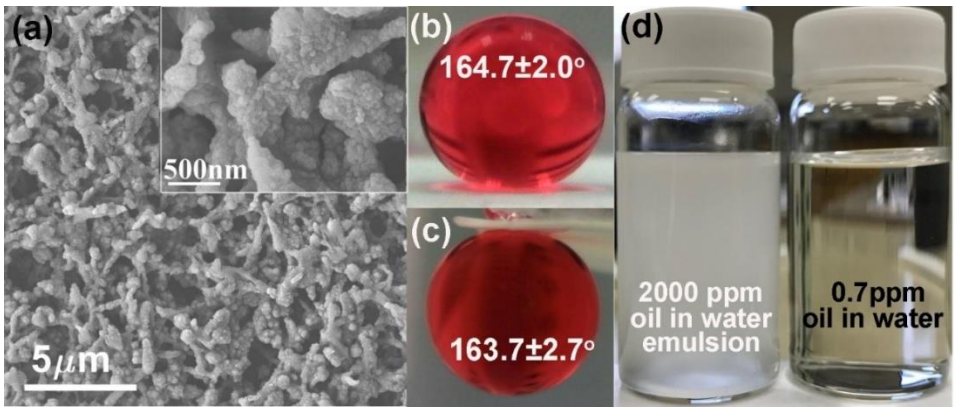

Figure 49**.** (a) SEM image of the TiO_2-coated PVDF membrane prepared by biomineralization for vacuum-assisted separation of oil/water emulsion; images of oil red dyed (b) dichloroethane and (c) petroleum oil droplets on the TiO_2-coated PVDF membranes, submerged in water; (d) photographs of 2000 ppm petroleum in water emulsion and collected water after separation using the TiO_2-coated PVDF membrane.

To highlight the advantages of the biomineralization-enabled coating approach and coated meshes developed in this work, we compared our developed TSSM with other reported TiO_2-based membranes and coated stainless steel meshes for oil/water separation. As shown in Table 3, the fabrication methods of most reported meshes and membranes require the preparation of precursor sols or seeds and post-annealing at high temperature, making these methods time and energy-consuming. The biomineralization-enabled coating approach developed in this work, however, is facile and carried out at ambient conditions. In addition, our developed TSSM has good mechanical durability and higher oil rejection efficiency than those reported meshes and membranes. Therefore, we believe the coating approach and coated meshes we developed in this work are promising for oil/water separation.

Table 3. Comparison of the TiO_2-coated meshes developed in this work with other reported TiO_2-based membranes and coated stainless steel meshes for oil/water separation.

Membrane Materials	**Fabrication Method**	**Oil Rejection Rate**	**Flux ($Lm^{-2}h^{-1}$)**	**Mechanical Stability**
TiO_2 nanoparticles on SSM [55]	Preparation of TiO_2 sol; dip-coating; annealing at 500 °C	99.5% for petroleum ether	1780	Could stand sonication and tape striping test
TiO_2 nanoparticles on SSM [53]	Spray coating of TiO_2 nanoparticles	95.5% for petroleum ether	Not reported.	Not reported
Various TiO_2 nanostructures on glass fiber filter [124]	Hydrothermal synthesis of TiO_2 nanostructures; Filtration	99.89% for crude oil	Not reported.	Not reported
TiO_2 nanowires on Ti mesh [145]	Anodization; annealing at 350 °C	99.5% for petroleum ether	16954	Could stand flowing sands impact and tape adhering
Zeolite on SSM [146]	Hydrothermal synthesis of zeolite seeds; seeding; annealing at 550 °C	99.7% for hexane	80000	Not reported
Polydimethylsiloxane (PDMS) on SSM [120]	Vapor deposition at 550 °C	99.0 % for petroleum ether	80000	Not reported
Graphene oxide on SSM [123]	Graphene oxide via a modified Hummers method; sonication	99 % for hexane	36000	Not reported
TiO_2 thin film on SSM in this work	Dip-coating assisted biomineralization at ambient conditions	99.999 % for petroleum oil	30000	Could stand abrasion, sonication and crumpling

5.9 Mechanism of oil/water separation using TSSM

To illustrate the oil/water separation process enabled by TSSM, a model is provided to compare the wetting behavior of oil and water on SSM and TSSM. The cross-section views of the systems are shown in Figure 50, where two adjacent mesh wires are used as a unit in the model. It is noted that the woven structure of the mesh requires more complex structural representation but the approximation in the model should be able to provide insights into the oil/water separation process. SSM is hydrophobic and oleophobic in air and the formed menisci of water and oil are stable on SSM as shown in Figure 50a and b.[52, 62, 120] Consequently, oil and water cannot

spontaneously pass through SSM, unless the required intrusion pressure, ΔP, is overcome by externally applied pressure. The intrusion pressure is calculated as $\Delta P = -2\gamma\cos(\theta)/d$,[147, 148] where γ is the interfacial tension between liquid and air or liquid and liquid, θ is the contact angle, and d is the distance between two adjacent wires, as shown in a. After TiO_2 coating, the surface energy is changed and TSSM becomes superhydrophilic. Thus, TSSM is readily wetted by water and the intrusion pressure is negative, indicating that water is able to pass through TSSM spontaneously (Figure 50c). Upon being wetted in water, the TSSM surface adsorbs water and a water film is formed. This continuous water film prevents the formation of air pockets and repels oil. As a result, the intrusion pressure of oil penetrating the water-wetted TSSM is positive and oil is blocked but water is allowed to pass through the mesh to implement efficient oil/water separation (Figure 50d).

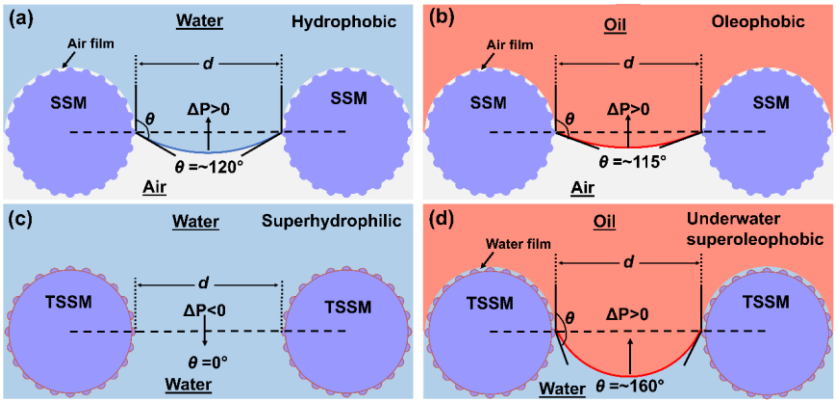

Figure 50. Schematic diagrams of oil and water wetting models on SSM and TSSM. (a, b) SSM is hydrophobic and oleophobic. Intrusion pressures are positive, i.e., $\theta > 90$ º and $\Delta P > 0$. (c) TSSM is superhydrophilic and is readily wetted by water, i.e., $\theta = \sim 0$ º and $\Delta P < 0$. (d) TSSM is superoleophobic under water and the intrusion pressure of oil penetrating a water-wetted TSSM is positive.

5.10 Conclusion

In conclusion, TiO_2-coated stainless steel meshes were facilely fabricated via the biomineralization approach in an environmentally benign manner. The uniform, smooth, thin and conformal coating of TiO_2 endowed the mesh with superhydrophilicity and underwater superoleophobicity. It could selectively separate water from various oil/water mixtures driven by gravity with a high separation flux (~3×10^4 L m^{-2} h^{-1}), high oil rejection efficiency (~ 99.999%), and excellent resistance to oil fouling. In addition, this coated mesh possessed excellent durability to use under chemically, thermally and mechanically harsh conditions. The biomineralization approach also found success in applying TiO_2 coating on other mesh/membranes for the application in oil/water separation. Thus, we envision that this biomineralization-enabled TiO_2-coated mesh has potentials for applications in the removal of oil from water.

CHAPTER 6

PHOTOCATALYTIC AND SUPERWETTING MEMBRANES FOR OIL/WATER EMULSIONS TREATMENT[5]

6.1 Background and Hypothesis

As presented in Chapter 5, the TiO_2-coated stainless steel mesh was capable of efficiently separating immiscible oil in water mixtures, however the coated mesh cannot treat emulsified oil in water mixtures, i.e., oil/water emulsions. This is mainly because the oil droplets in emulsions are of hundreds of nanometers to tens of micrometers, while the pore size of the mesh is around 5 micrometers. Inherently, polymeric membranes are competent to separate the emulsions because of the ease to obtain small pore size and fine porous structure. PVDF membranes are particularly attractive due to their good mechanical and chemical durability, which enables wide applications in filtration techniques. Generally, pristine e PVDF membranes are hydrophobic and oleophilic, and not suitable for treating oil in water emulsions. To solve this problem, several methods have been developed, including post surface coating, adding inorganic particles and modifying the phase-inversion process. Shi et al. reported binding TiO_2 nanoparticles to the surface of PVDF membrane via silane coupling turned the membrane into superhydrophilic and Yuan et al. obtained superhydrophilic and superoleophobic surface by interfacial polymerization-constructed hydrogel.[149, 150] Composite PVDF membranes with improved hydrophilicity could be fabricated by facilely direct compounding nanoparticles with PVDF precursor solutions followed by the phase-inversion process, but these prepared composite membranes could not achieve

[5] This chapter includes unpublished results.

superhydrophilicity (water contact angles were larger than 50 º).[151-153] By modifying the phase-inversion process, Zhang et al. developed a salt-induced phase-inversion approach for fabricating poly(acrylic acid)-grafted PVDF membranes with superwettability. These works advanced the development of superwetting membranes and their applications for oil/water separation.

Though superoleophobic surfaces have low oil-adhesion, oil-fouling and subsequent flux decline are still a major barrier that hinders the applicability of superwetting membranes. In addition, surfactant stabilization prevents the oil droplets from coalescence, exacerbating the fouling problem and furthering flux decline. A tentative solution is using photocatalytic reactions to degrade adsorbed oils on the membrane surface and thus achieve self-cleaning. Li et al. prepared photocatalytic porous membrane based on hierarchical TiO_2 nanotubes for oil/water separation and the photocatalytic effect was used degrade organic pollutants (such methylene blue) but not mitigate oil-fouling.[154] Zhang et al. prepared a TiO_2-coated mesh for oil-water separation and demonstrated the self-cleaning capability by recovering the surface wettability from oleic-acid-contamination using light irradiation but didn't study oil-fouling mitigation.[54] More recently, Liu et al. reported GO/g-C_3N_4@TiO_2 membrane that could recover the permeate flux of DI-water assisted by simulated sunlight, however, for every 10-min separation of the oil/water emulsion, 20 min rinsing by DI-water and 60 min irradiation were required to recover the fouled membrane. Moreover, the preparation of the precursor materials for this reported membrane is relatively complex.[155] Therefore, it is still necessary to develop photocatalytic superwetting membranes from facile approaches that can employ photocatalytic effect to efficiently mitigate oil-fouling.

In this work, we fabricated photocatalytic-superhydrophilic PVDF-BiOBr composite membrane from the phase -inversion approach, which is the most common, cost-effective and

scalable method for the fabrication of polymeric membranes. The as-prepared PVDF-BiOBr membrane showed great capability for oil rejection and oil-fouling mitigation.

6.2 Preliminary Results

Three membranes samples were prepared and compared in this section for preliminary testing. The pristine PVDF membrane was fabricated by the facile phase-inversion approach. The approach was modified to fabricate the PVDF-BiOBr and PVDF-BiOBr(microsphere) membranes. The fabrication of these two membranes, bismuth nitrate and potassium bromide or synthesized BiOBr microspheres were added into the PVDF dope solution. Then the hydrophilicity, morphology and emulsion separation capability were examined.

As shown in Figure 51, the prepared PVDF-75C membrane has a water contact angle of about 80º and it is stable in air, indicating that the membrane is not superhydrophilic and cannot be completely wetted by water. Interestingly, adding bismuth and bromide precursors into the dope solution made the membrane become superhydrophilic and this trended increased with the temperature of the water bath, while directly adding BiOBr microspheres into the dope solution did not help improve the hydrophilicity. This is probably because adding bismuth and bromide precursors could produce BiOBr nanocrystals uniformly distributed inside the PVDF matrix.

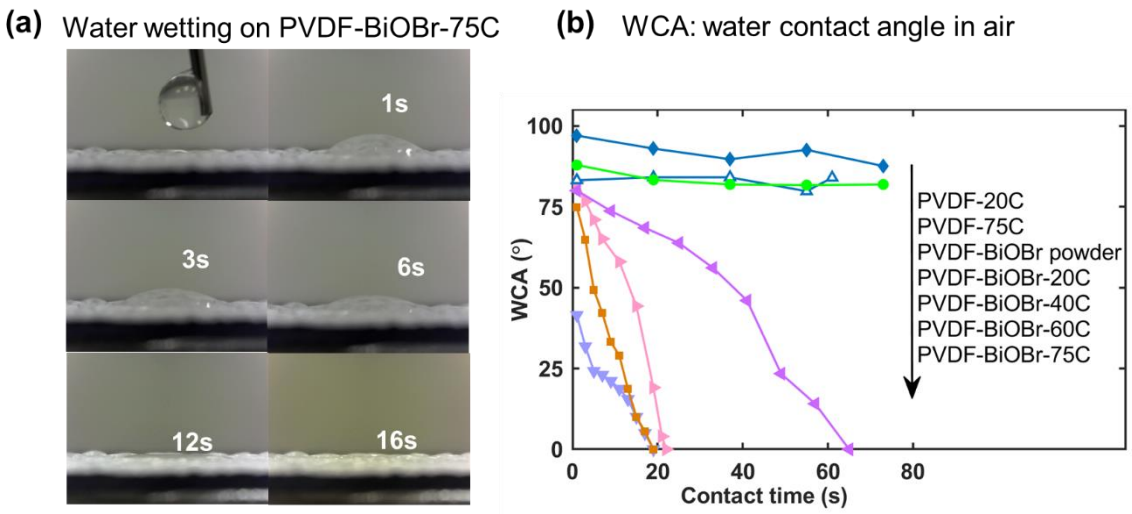

Figure 51. Time-resolved change of (a) water droplet on the PVDF-BiOBr-75C membrane and (b) water contact angles on different membranes.

The oleophobicity of the PVDF-BiOBr membrane was evaluated by measuring the underwater oil contact angle (Figure 52). The PVDF-75C membrane is superoleophobic but the PVDF-BiOBr-75C membranes has an oil contact angle of ~ 140 º. The prepared membranes were used to tentatively separate emulsified 200 ppm hexadecane in water mixtures with and without irradiation under a pressure of 3 kPa. The results in Figure 53 indicate that irradiation and hydrophilicity helped improve the permeate flux. It is interesting the PVDF-BiOBr-75C membrane showed much slower flux decline under dark than under light, though had a lower initial flux. There are two possible reasons. One is that photocatalytic reactions may break oil droplets into smaller droplets that can penetrate into the membrane and block the membrane. The second is that photocatalytic reactions may produce some intermediates and alter the surface wettability. Further study will be followed to investigate this.

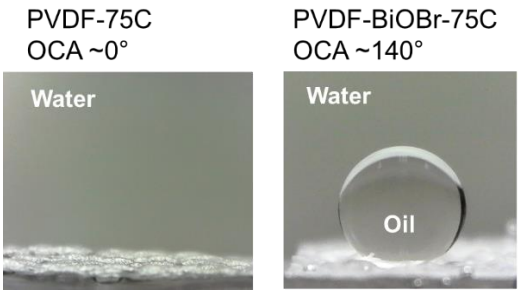

Figure 52. Photographs of oil droplets (3 µL dichloroethane) on the PVDF-75C and PVDF-BiOBr-75C membranes.

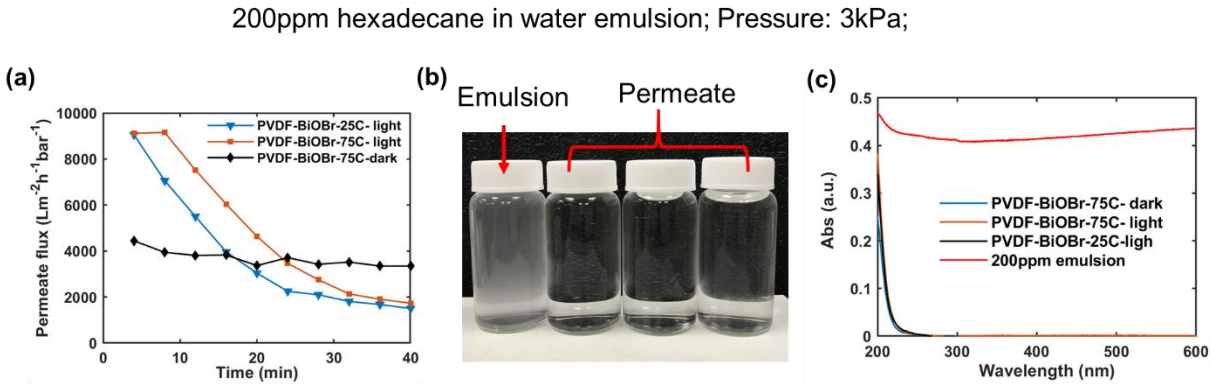

Figure 53. (a) time-resolved change of the permeate fluxes of separating oil/water emulsions using the membranes with or without irradiation; (b) photographs of the emulsion and permeates; (c) UV-vis absorbance of the permeates.

6.3 Future Work

In next step, the PVDF-BiOBr membranes will be optimized to further improve the surface oleophobicity. The effects of photocatalysis on fouling mitigation will be systematically investigated to demonstrate the beneficial synergy of endowing the membrane with superwettability and photoactivity.

CHAPTER 7

CONCLUSION AND FUTURE WORK

In this dissertation, I investigated approaches for improving photodegradation efficiency and novel membranes for oil/water separation. I demonstrated that by manipulating the reactive species using sulfite, the generated sulfite radicals could promote photocatalytic degradation of organic pollutants. I also studied the adsorption-photocatalysis using well-designed model photocatalysts to further the understanding of this synergy and help develop high-adsorption photocatalysts. To prepare durable superwetting membranes for separating immiscible oil/water mixtures, I developed a facile biomineralization-enabled TiO_2-coating approach and the coated membranes showed great capability for oil/water separation. I also fabricated novel photocatalytic-superhydrophilic polymeric composite membranes to treat oil/water emulsions and the photocatalytic effects helped mitigate oil-fouling.

Photocatalysis for water treatment has been studied for decades and researchers have explored enormous number of new photocatalysts that are claimed to outperform P25 TiO_2 (a commercially available benchmark photocatalyst), however, studies and applications of this technique are still limited to lab-scale or small-scale validation. Novel photocatalytic membranes that can address the post-separation/mass-transfer-limitation dilemma are believed to help photocatalysis advance toward practical applications, however, the reported photocatalytic membranes are not satisfactory so far, leaving great opportunities in this direction. Since polymeric membranes offer suitable matrices for hosting nanosized and microsized photocatalysts, I believe photocatalytic polymeric membranes could be a promising design to apply photocatalysis for practical water treatment. Since the photocatalysts should be compatible with the polymer

matrices, the structures, morphologies and preparation methods of the photocatalysts and the polymer membranes should be considered simultaneously.

Adding filler materials into polymer membrane could also help develop novel membranes to treat wastewater. Depending on the added materials, multi-functioned composite membranes can be prepared. Photocatalytic, electrocatalytic, photothermal, and superwetting properties are readily to be incorporated into membranes by adding one to several different filler materials through appropriate fabrication process. Different filler materials can be either mixed in one membrane layer or added to different layers in a laminar structure. It is also possible to apply post-coating to further modify these composite membranes. Making these composite membranes is a great way to integrate multiple treating methods into one module seamlessly at low cost and compact size. Meanwhile, the integration of different techniques is able to overcome some inherent limitations of certain techniques. In addition, these modules with multiple functions should help the decentralization of water treatment.

Based on these discussions, my future work will focus on the following directions.

1) Improve the mineralization efficiency of the sulfite-promoted photodegradation approach; improve the utilization efficiency of sulfite (or other added chemicals) by innovative reactor design or photocatalytic membrane development.

2) Combine adding filler materials and surface coating to fabricate photocatalytic-superwetting membranes for treating oil/water emulsions with anti-fouling capability.

3) Develop multi-functioned laminar membranes that have photocatalytic, photothermal and superwetting properties for hybrid membrane distillation.

4) Study electrocatalytic membranes and couple electrocatalysis with other techniques for water treatment.

In summary, my future work will emphasize on using sunlight and electricity as energy sources for water treatment with the assistance of membrane technology.

REFERENCES

[1] W.E. Forum, Global Risks 2015–10th Edition, (2015).

[2] W.H. Organization, UNICEF, Progress on drinking water, sanitation and hygiene: 2017 update and SDG baselines, (2017).

[3] M.A. Shannon, P.W. Bohn, M. Elimelech, J.G. Georgiadis, B.J. Marinas, A.M. Mayes, Science and technology for water purification in the coming decades, in: Nanoscience And Technology: A Collection of Reviews from Nature Journals, World Scientific, 2010, pp. 337-346.

[4] M.A. Montgomery, M. Elimelech, Water and sanitation in developing countries: including health in the equation, in, ACS Publications, 2007.

[5] B.C. Hodges, E.L. Cates, J.-H. Kim, Challenges and prospects of advanced oxidation water treatment processes using catalytic nanomaterials, Nature nanotechnology, 13 (2018) 642.

[6] D. Jassby, T.Y. Cath, H. Buisson, The role of nanotechnology in industrial water treatment, Nature nanotechnology, 13 (2018) 670.

[7] P.J. Alvarez, C.K. Chan, M. Elimelech, N.J. Halas, D. Villagrán, Emerging opportunities for nanotechnology to enhance water security, Nature nanotechnology, 13 (2018) 634.

[8] N. Puvaneswari, J. Muthukrishnan, P. Gunasekaran, Toxicity assessment and microbial degradation of azo dyes, (2006).

[9] I. Ali, M. Asim, T.A. Khan, Low cost adsorbents for the removal of organic pollutants from wastewater, Journal of environmental management, 113 (2012) 170-183.

[10] M. Megharaj, B. Ramakrishnan, K. Venkateswarlu, N. Sethunathan, R. Naidu, Bioremediation approaches for organic pollutants: a critical perspective, Environment International, 37 (2011) 1362-1375.

[11] Y.M. Slokar, A.M. Le Marechal, Methods of decoloration of textile wastewaters, Dyes and pigments, 37 (1998) 335-356.

[12] J.J. Pignatello, E. Oliveros, A. MacKay, Advanced oxidation processes for organic contaminant destruction based on the Fenton reaction and related chemistry, Critical reviews in environmental science and technology, 36 (2006) 1-84.

[13] K. Ikehata, M. Gamal El-Din, S.A. Snyder, Ozonation and advanced oxidation treatment of emerging organic pollutants in water and wastewater, Ozone: Science and Engineering, 30 (2008) 21-26.

[14] S.S. Moghaddam, M.A. Moghaddam, M. Arami, Coagulation/flocculation process for dye removal using sludge from water treatment plant: optimization through response surface methodology, J. Hazard. Mater., 175 (2010) 651-657.

[15] C.A. Martínez-Huitle, E. Brillas, Decontamination of wastewaters containing synthetic organic dyes by electrochemical methods: a general review, Appl. Catal., B, 87 (2009) 105-145.

[16] H. Lachheb, E. Puzenat, A. Houas, M. Ksibi, E. Elaloui, C. Guillard, J.-M. Herrmann, Photocatalytic degradation of various types of dyes (Alizarin S, Crocein Orange G, Methyl Red, Congo Red, Methylene Blue) in water by UV-irradiated titania, Appl. Catal., B, 39 (2002) 75-90.

[17] M. Pelaez, N.T. Nolan, S.C. Pillai, M.K. Seery, P. Falaras, A.G. Kontos, P.S. Dunlop, J.W. Hamilton, J.A. Byrne, K. O'shea, A review on the visible light active titanium dioxide photocatalysts for environmental applications, Appl. Catal., B, 125 (2012) 331-349.

[18] H. Wang, L. Zhang, Z. Chen, J. Hu, S. Li, Z. Wang, J. Liu, X. Wang, Semiconductor heterojunction photocatalysts: design, construction, and photocatalytic performances, Chem. Soc. Rev., 43 (2014) 5234-5244.

[19] H. Cheng, B. Huang, Y. Dai, Engineering BiOX (X= Cl, Br, I) nanostructures for highly efficient photocatalytic applications, Nanoscale, 6 (2014) 2009-2026.

[20] Q. Xiang, D. Lang, T. Shen, F. Liu, Graphene-modified nanosized Ag3PO4 photocatalysts for enhanced visible-light photocatalytic activity and stability, Appl. Catal., B, 162 (2015) 196-203.

[21] W. Zhao, Y. Liu, Z. Wei, S. Yang, H. He, C. Sun, Fabrication of a novel p–n heterojunction photocatalyst n-BiVO4@ p-MoS2 with core–shell structure and its excellent visible-light photocatalytic reduction and oxidation activities, Appl. Catal., B, 185 (2016) 242-252.

[22] A.N. Soon, B. Hameed, Heterogeneous catalytic treatment of synthetic dyes in aqueous media using Fenton and photo-assisted Fenton process, Desalination, 269 (2011) 1-16.

[23] M. Zlamal, J.M. Macak, P. Schmuki, J. Krýsa, Electrochemically assisted photocatalysis on self-organized TiO2 nanotubes, Electrochem. Commun., 9 (2007) 2822-2826.

[24] S. Mozia, A.W. Morawski, M. Toyoda, T. Tsumura, Integration of photocatalysis and membrane distillation for removal of mono-and poly-azo dyes from water, Desalination, 250 (2010) 666-672.

[25] M.J. Farré, M.I. Franch, S. Malato, J.A. Ayllón, J. Peral, X. Doménech, Degradation of some biorecalcitrant pesticides by homogeneous and heterogeneous photocatalytic ozonation, Chemosphere, 58 (2005) 1127-1133.

[26] R. Molinari, L. Palmisano, E. Drioli, M. Schiavello, Studies on various reactor configurations for coupling photocatalysis and membrane processes in water purification, Journal of Membrane Science, 206 (2002) 399-415.

[27] S. Mozia, Photocatalytic membrane reactors (PMRs) in water and wastewater treatment. A review, Sep. Purif. Technol., 73 (2010) 71-91.

[28] L. Prieto-Rodriguez, S. Miralles-Cuevas, I. Oller, A. Agüera, G.L. Puma, S. Malato, Treatment of emerging contaminants in wastewater treatment plants (WWTP) effluents by solar photocatalysis using low TiO2 concentrations, J. Hazard. Mater., 211 (2012) 131-137.

[29] N. Miranda-García, S. Suárez, B. Sánchez, J. Coronado, S. Malato, M.I. Maldonado, Photocatalytic degradation of emerging contaminants in municipal wastewater treatment plant effluents using immobilized TiO2 in a solar pilot plant, Appl. Catal., B, 103 (2011) 294-301.

[30] A. Bernabeu, R. Vercher, L. Santos-Juanes, P. Simón, C. Lardín, M. Martínez, J. Vicente, R. González, C. Llosá, A. Arques, Solar photocatalysis as a tertiary treatment to remove emerging pollutants from wastewater treatment plant effluents, Catal. Today, 161 (2011) 235-240.

[31] E.S. Elmolla, M. Chaudhuri, Photocatalytic degradation of amoxicillin, ampicillin and cloxacillin antibiotics in aqueous solution using UV/TiO2 and UV/H2O2/TiO2 photocatalysis, Desalination, 252 (2010) 46-52.

[32] R. Hazime, Q.H. Nguyen, C. Ferronato, A. Salvador, F. Jaber, J.M. Chovelon, Comparative study of imazalil degradation in three systems: UV/TiO2, UV/K2S2O8 and UV/TiO2/K2S2O8, Appl. Catal., B, 144 (2014) 286-291.

[33] H.-Y. Jing, T. Wen, C.-M. Fan, G.-Q. Gao, S.-L. Zhong, A.-W. Xu, Efficient adsorption/photodegradation of organic pollutants from aqueous systems using Cu 2 O nanocrystals as a novel integrated photocatalytic adsorbent, J. Mater. Chem. A, 2 (2014) 14563-14570.

[34] F. Chen, W. An, L. Liu, Y. Liang, W. Cui, Highly efficient removal of bisphenol A by a three-dimensional graphene hydrogel-AgBr@ rGO exhibiting adsorption/photocatalysis synergy, Appl. Catal., B, 217 (2017) 65-80.

[35] J. Sun, L. Qiao, S. Sun, G. Wang, Photocatalytic degradation of Orange G on nitrogen-doped TiO2 catalysts under visible light and sunlight irradiation, J. Hazard. Mater., 155 (2008) 312-319.

[36] Y. Yu, C. Cao, H. Liu, P. Li, F. Wei, Y. Jiang, W. Song, A Bi/BiOCl heterojunction photocatalyst with enhanced electron–hole separation and excellent visible light photodegrading activity, J. Mater. Chem. A, 2 (2014) 1677-1681.

[37] T. Chen, Y. Zheng, J.-M. Lin, G. Chen, Study on the Photocatalytic Degradation of Methyl Orange in Water Using Ag/ZnO as Catalyst by Liquid Chromatography Electrospray Ionization Ion-Trap Mass Spectrometry, J. Am. Soc. Mass. Spectrom., 19 (2008) 997-1003.

[38] J. Kaur, S. Singhal, Facile synthesis of ZnO and transition metal doped ZnO nanoparticles for the photocatalytic degradation of Methyl Orange, Ceram. Int., 40 (2014) 7417-7424.

[39] U.G. Akpan, B.H. Hameed, Parameters affecting the photocatalytic degradation of dyes using TiO2-based photocatalysts: a review, J. Hazard. Mater., 170 (2009) 520-529.

[40] M. Padaki, R.S. Murali, M.S. Abdullah, N. Misdan, A. Moslehyani, M. Kassim, N. Hilal, A. Ismail, Membrane technology enhancement in oil–water separation. A review, Desalination, 357 (2015) 197-207.

[41] Z. Chu, Y. Feng, S. Seeger, Oil/water separation with selective superantiwetting/superwetting surface materials, Angew. Chem. Int. Ed., 54 (2015) 2328-2338.

[42] Z. Xue, Y. Cao, N. Liu, L. Feng, L. Jiang, Special wettable materials for oil/water separation, J. Mater. Chem. A, 2 (2014) 2445-2460.

[43] Y. Cai, D. Chen, N. Li, Q. Xu, H. Li, J. He, J. Lu, A facile method to fabricate a double-layer stainless steel mesh for effective separation of water-in-oil emulsions with high flux, J. Mater. Chem. A, 4 (2016) 18815-18821.

[44] G. Kwon, A.K. Kota, Y. Li, A. Sohani, J.M. Mabry, A. Tuteja, On‐demand separation of oil‐water mixtures, Adv. Mater., 24 (2012) 3666-3671.

[45] A.K. Kota, G. Kwon, W. Choi, J.M. Mabry, A. Tuteja, Hygro-responsive membranes for effective oil–water separation, Nature communications, 3 (2012) 1025.

[46] B. Xue, L. Gao, Y. Hou, Z. Liu, L. Jiang, Temperature controlled water/oil wettability of a surface fabricated by a block copolymer: application as a dual water/oil on–off switch, Adv. Mater., 25 (2013) 273-277.

[47] M.W. Lee, S. An, S.S. Latthe, C. Lee, S. Hong, S.S. Yoon, Electrospun polystyrene nanofiber membrane with superhydrophobicity and superoleophilicity for selective separation of water and low viscous oil, ACS Appl. Mater. Interfaces, 5 (2013) 10597-10604.

[48] Y. Cao, N. Liu, C. Fu, K. Li, L. Tao, L. Feng, Y. Wei, Thermo and pH dual-responsive materials for controllable oil/water separation, ACS Appl. Mater. Interfaces, 6 (2014) 2026-2030.

[49] W. Zhang, N. Liu, Y. Cao, Y. Chen, L. Xu, X. Lin, L. Feng, A solvothermal route decorated on different substrates: controllable separation of an oil/water mixture to a stabilized nanoscale emulsion, Adv. Mater., 27 (2015) 7349-7355.

[50] Y. Cao, X. Zhang, L. Tao, K. Li, Z. Xue, L. Feng, Y. Wei, Mussel-inspired chemistry and michael addition reaction for efficient oil/water separation, ACS Appl. Mater. Interfaces, 5 (2013) 4438-4442.

[51] L. Feng, Z. Zhang, Z. Mai, Y. Ma, B. Liu, L. Jiang, D. Zhu, A super‐hydrophobic and super‐oleophilic coating mesh film for the separation of oil and water, Angew. Chem., 116 (2004) 2046-2048.

[52] M.A. Gondal, M.S. Sadullah, M.A. Dastageer, G.H. McKinley, D. Panchanathan, K.K. Varanasi, Study of factors governing oil–water separation process using TiO2 films prepared by spray deposition of nanoparticle dispersions, ACS Appl. Mater. Interfaces, 6 (2014) 13422-13429.

[53] J. Li, L. Yan, W. Hu, D. Li, F. Zha, Z. Lei, Facile fabrication of underwater superoleophobic TiO2 coated mesh for highly efficient oil/water separation, Colloids and Surfaces A: Physicochemical and Engineering Aspects, 489 (2016) 441-446.

[54] L. Zhang, Y. Zhong, D. Cha, P. Wang, A self-cleaning underwater superoleophobic mesh for oil-water separation, Scientific reports, 3 (2013) 2326.

[55] Z.-Q. Dong, B.-J. Wang, M. Liu, X.-h. Ma, Z.-L. Xu, A self-cleaning TiO 2 coated mesh with robust underwater superoleophobicity for oil/water separation in a complex environment, RSC Advances, 6 (2016) 65171-65178.

[56] Z. Xue, S. Wang, L. Lin, L. Chen, M. Liu, L. Feng, L. Jiang, A novel superhydrophilic and underwater superoleophobic hydrogel‐coated mesh for oil/water separation, Adv. Mater., 23 (2011) 4270-4273.

[57] H. Yang, P. Pi, Z.-Q. Cai, X. Wen, X. Wang, J. Cheng, Z.-r. Yang, Facile preparation of super-hydrophobic and super-oleophilic silica film on stainless steel mesh via sol–gel process, Appl. Surf. Sci., 256 (2010) 4095-4102.

[58] J. Li, R. Kang, X. Tang, H. She, Y. Yang, F. Zha, Superhydrophobic meshes that can repel hot water and strong corrosive liquids used for efficient gravity-driven oil/water separation, Nanoscale, 8 (2016) 7638-7645.

[59] J. Zeng, Z. Guo, Superhydrophilic and underwater superoleophobic MFI zeolite-coated film for oil/water separation, Colloids and Surfaces A: Physicochemical and Engineering Aspects, 444 (2014) 283-288.

[60] Q. Wen, J. Di, L. Jiang, J. Yu, R. Xu, Zeolite-coated mesh film for efficient oil–water separation, Chemical Science, 4 (2013) 591-595.

[61] D. Tian, X. Zhang, Y. Tian, Y. Wu, X. Wang, J. Zhai, L. Jiang, Photo-induced water–oil separation based on switchable superhydrophobicity–superhydrophilicity and underwater superoleophobicity of the aligned ZnO nanorod array-coated mesh films, J. Mater. Chem., 22 (2012) 19652-19657.

[62] D. Tian, X. Zhang, X. Wang, J. Zhai, L. Jiang, Micro/nanoscale hierarchical structured ZnO mesh film for separation of water and oil, PCCP, 13 (2011) 14606-14610.

[63] E.S. Elmolla, M. Chaudhuri, Photocatalytic degradation of amoxicillin, ampicillin and cloxacillin antibiotics in aqueous solution using UV/TiO2 and UV/H2O2/TiO2 photocatalysis, Desalination, 252 (2010) 46-52.

[64] R.E. Huie, P. Neta, Chemical behavior of sulfur trioxide (1-)(SO3-) and sulfur pentoxide (1-)(SO5-) radicals in aqueous solutions, J. Phys. Chem., 88 (1984) 5665-5669.

[65] R. Norman, P. Storey, Electron spin resonance studies. Part XXXI. The generation, and some reactions, of the radicals SO 3–·, S 2 O 3–·, S–·, and SH in aqueous solution, Journal of the Chemical Society B: Physical Organic, (1971) 1009-1013.

[66] T. Ozawa, T. Kwan, Esr evidence for the formation of new vinyl radicals in solution, J. Chem. Soc., Chem. Commun., (1983) 80-81.

[67] T. Ozawa, T. Kwan, Esr studies on the reactive character of the radical anions, so− 2, so− 3 and so− 4 in aqueous solution, Polyhedron, 2 (1983) 1019-1023.

[68] M. Erben-Russ, W. Bors, R. Winter, M. Saran, The reaction of sulfite anion radical (SO.-3) with polyunsaturated fatty acids, International Journal of Radiation Applications and Instrumentation. Part C. Radiation Physics and Chemistry, 27 (1986) 419-424.

[69] B.P. Vellanki, B. Batchelor, A. Abdel-Wahab, Advanced reduction processes: a new class of treatment processes, Environmental engineering science, 30 (2013) 264-271.

[70] X. Li, J. Ma, G. Liu, J. Fang, S. Yue, Y. Guan, L. Chen, X. Liu, Efficient reductive dechlorination of monochloroacetic acid by sulfite/UV process, Environmental science & technology, 46 (2012) 7342-7349.

[71] X. Liu, B.P. Vellanki, B. Batchelor, A. Abdel-Wahab, Degradation of 1, 2-dichloroethane with advanced reduction processes (ARPs): Effects of process variables and mechanisms, Chem. Eng. J., 237 (2014) 300-307.

[72] B. Jung, H. Farzaneh, A. Khodary, A. Abdel-Wahab, Photochemical degradation of trichloroethylene by sulfite-mediated UV irradiation, Journal of Environmental Chemical Engineering, 3 (2015) 2194-2202.

[73] W. Deng, H. Zhao, F. Pan, X. Feng, B. Jung, A. Abdel-Wahab, B. Batchelor, Y. Li, Visible-Light-Driven Photocatalytic Degradation of Organic Water Pollutants Promoted by Sulfite Addition, Environmental Science & Technology, 51 (2017) 13372-13379.

[74] W. Deng, H. Zhao, F. Pan, X. Feng, B. Jung, A. Abdel-Wahab, B. Batchelor, Y. Li, Response to Comment on “Visible-Light-Driven Photocatalytic Degradation of Organic Water Pollutants Promoted by Sulfite Addition”, Environmental science & technology, 52 (2018) 1677-1678.

[75] H. Gnayem, Y. Sasson, Hierarchical nanostructured 3D flowerlike BiOCl x Br1–x semiconductors with exceptional visible light photocatalytic activity, ACS Catal., 3 (2013) 186-191.

[76] H. Cheng, B. Huang, P. Wang, Z. Wang, Z. Lou, J. Wang, X. Qin, X. Zhang, Y. Dai, In situ ion exchange synthesis of the novel Ag/AgBr/BiOBr hybrid with highly efficient decontamination of pollutants, Chem. Commun., 47 (2011) 7054-7056.

[77] D. Zhang, M. Wen, B. Jiang, G. Li, C.Y. Jimmy, Ionothermal synthesis of hierarchical BiOBr microspheres for water treatment, J. Hazard. Mater., 211 (2012) 104-111.

[78] M. Thommes, K. Kaneko, A.V. Neimark, J.P. Olivier, F. Rodriguez-Reinoso, J. Rouquerol, K.S. Sing, Physisorption of gases, with special reference to the evaluation of surface area and pore size distribution (IUPAC Technical Report), Pure Appl. Chem., 87 (2015) 1051-1069.

[79] H. Journal of Physical Chemistry BFu, C. Pan, W. Yao, Y. Zhu, Visible-light-induced degradation of rhodamine B by nanosized Bi2WO6, The Journal of Physical Chemistry B, 109 (2005) 22432-22439.

[80] T. Hirakawa, Y. Nosaka, Properties of O2•-and OH• formed in TiO2 aqueous suspensions by photocatalytic reaction and the influence of H2O2 and some ions, Langmuir, 18 (2002) 3247-3254.

[81] A. Khataee, P. Gholami, B. Vahid, S.W. Joo, Heterogeneous sono-Fenton process using pyrite nanorods prepared by non-thermal plasma for degradation of an anthraquinone dye, Ultrason. Sonochem., 32 (2016) 357-370.

[82] J. Li, S.K. Cushing, P. Zheng, T. Senty, F. Meng, A.D. Bristow, A. Manivannan, N. Wu, Solar hydrogen generation by a CdS-Au-TiO2 sandwich nanorod array enhanced with Au

nanoparticle as electron relay and plasmonic photosensitizer, J. Am. Chem. Soc., 136 (2014) 8438-8449.

[83] E. Hayon, A. Treinin, J. Wilf, Electronic spectra, photochemistry, and autoxidation mechanism of the sulfite-bisulfite-pyrosulfite systems. SO2-, SO3-, SO4-, and SO5-radicals, J. Am. Chem. Soc., 94 (1972) 47-57.

[84] T.N. Das, R.E. Huie, P. Neta, Reduction potentials of SO3•-, SO5•-, and S4O6• 3-radicals in aqueous solution, J. Phys. Chem. A, 103 (1999) 3581-3588.

[85] P. Neta, R.E. Huie, Free-radical chemistry of sulfite, Environ. Health Perspect., 64 (1985) 209.

[86] W. Koppenol, J. Butler, Energetics of interconversion reactions of oxyradicals, Advances in Free Radical Biology & Medicine, 1 (1985) 91-131.

[87] F. Chen, Q. Yang, F. Yao, Y. Ma, Y. Wang, X. Li, D. Wang, L. Wang, H. Yu, Synergetic transformations of multiple pollutants driven by BiVO4-catalyzed sulfite under visible light irradiation: Reaction kinetics and intrinsic mechanism, Chem. Eng. J., 355 (2019) 624-636.

[88] J. Cao, W. Nie, L. Huang, Y. Ding, K. Lv, H. Tang, Photocatalytic activation of sulfite by nitrogen vacancy modified graphitic carbon nitride for efficient degradation of carbamazepine, Appl. Catal., B, 241 (2019) 18-27.

[89] H. Cheng, J. Han, I. Nabi, K. Li, T. Wang, Y. Yang, S. Ajmal, Y. Liu, L. Zhang, Significantly accelerated PEC degradation of organic pollutant with addition of sulfite and mechanism study, Appl. Catal., B, 248 (2019) 441-449.

[90] A.L. Linsebigler, G. Lu, J.T. Yates Jr, Photocatalysis on TiO2 surfaces: principles, mechanisms, and selected results, Chem. Rev., 95 (1995) 735-758.

[91] H. Zhang, X. Lv, Y. Li, Y. Wang, J. Li, P25-graphene composite as a high performance photocatalyst, ACS Nano, 4 (2009) 380-386.

[92] M. Li, B. Lu, Q.-F. Ke, Y.-J. Guo, Y.-P. Guo, Synergetic effect between adsorption and photodegradation on nanostructured TiO2/activated carbon fiber felt porous composites for toluene removal, J. Hazard. Mater., 333 (2017) 88-98.

[93] M. Zhang, W. Jiang, D. Liu, J. Wang, Y. Liu, Y. Zhu, Y. Zhu, Photodegradation of phenol via C3N4-agar hybrid hydrogel 3D photocatalysts with free separation, Appl. Catal., B, 183 (2016) 263-268.

[94] H. Anwer, J.-W. Park, Synthesis and characterization of a heterojunction rGO/ZrO2/Ag3PO4 nanocomposite for degradation of organic contaminants, J. Hazard. Mater., 358 (2018) 416-426.

[95] T. Qian, X. Yin, J. Li, H. Xu, Y. Deng, X. Wang, Nano-TiO2 Decorated Radial-Like Mesoporous Silica: Preparation, Characterization, and Adsorption-Photodegradation Behavior, Journal of materials science & technology, 33 (2017) 1314-1322.

[96] X.-X. Wei, H. Cui, S. Guo, L. Zhao, W. Li, Hybrid BiOBr–TiO 2 nanocomposites with high visible light photocatalytic activity for water treatment, J. Hazard. Mater., 263 (2013) 650-658.

[97] X. Liu, A. Jin, Y. Jia, T. Xia, C. Deng, M. Zhu, C. Chen, X. Chen, Synergy of adsorption and visible-light photocatalytic degradation of methylene blue by a bifunctional Z-scheme heterojunction of WO3/g-C3N4, Appl. Surf. Sci., 405 (2017) 359-371.

[98] J. Liu, Z.-Y. Hu, Y. Peng, H.-W. Huang, Y. Li, M. Wu, X.-X. Ke, G. Van Tendeloo, B.-L. Su, 2D ZnO mesoporous single-crystal nanosheets with exposed {0001} polar facets for the depollution of cationic dye molecules by highly selective adsorption and photocatalytic decomposition, Appl. Catal., B, 181 (2016) 138-145.

[99] Y. Wu, M. Xu, X. Chen, S. Yang, H. Wu, J. Pan, X. Xiong, CTAB-assisted synthesis of novel ultrathin MoSe 2 nanosheets perpendicular to graphene for the adsorption and photodegradation of organic dyes under visible light, Nanoscale, 8 (2016) 440-450.
[100] H.-Y. Zhu, R. Jiang, Y.-Q. Fu, R.-R. Li, J. Yao, S.-T. Jiang, Novel multifunctional NiFe2O4/ZnO hybrids for dye removal by adsorption, photocatalysis and magnetic separation, Appl. Surf. Sci., 369 (2016) 1-10.
[101] V. Augugliaro, S. Yurdakal, V. Loddo, G. Palmisano, L. Palmisano, Determination of Photoadsorption Capacity of Polychrystalline TiO2 Catalyst in Irradiated Slurry, Advances in Chemical Engineering, 36 (2009) 1-35.
[102] H.I. De Lasa, B. Serrano, M. Salaices, Photocatalytic reaction engineering, Springer, 2005.
[103] A. Khataee, M. Fathinia, S. Aber, Kinetic modeling of liquid phase photocatalysis on supported TiO2 nanoparticles in a rectangular flat-plate photoreactor, Ind. Eng. Chem. Res., 49 (2010) 12358-12364.
[104] M.A. Abdullah, F.K. Chong, Dual-effects of adsorption and photodegradation of methylene blue by tungsten-loaded titanium dioxide, Chem. Eng. J., 158 (2010) 418-425.
[105] Y. Li, S. Sun, M. Ma, Y. Ouyang, W. Yan, Kinetic study and model of the photocatalytic degradation of rhodamine B (RhB) by a TiO2-coated activated carbon catalyst: Effects of initial RhB content, light intensity and TiO2 content in the catalyst, Chem. Eng. J., 142 (2008) 147-155.
[106] N. Daneshvar, M. Rabbani, N. Modirshahla, M. Behnajady, Kinetic modeling of photocatalytic degradation of Acid Red 27 in UV/TiO2 process, J. Photochem. Photobiol., A, 168 (2004) 39-45.
[107] W. Deng, F. Pan, B. Batchelor, B. Jung, P. Zhang, A. Abdel-Wahab, H. Zhou, Y. Li, Mesoporous TiO2-BiOBr Microspheres with Tailorable Adsorption Capacities for

Photodegradation of Organic Water Pollutants: Probing Adsorption-Photocatalysis Synergy by Combining Experiments and Kinetic Modeling, in, 2018, pp. Under review.

[108] X.-j. Wang, W.-y. Yang, F.-t. Li, J. Zhao, R.-h. Liu, S.-j. Liu, B. Li, Construction of amorphous TiO2/BiOBr heterojunctions via facets coupling for enhanced photocatalytic activity, J. Hazard. Mater., 292 (2015) 126-136.

[109] Y. Chen, M. Wen, Q. Wu, Stepwise blossoming of BiOBr nanoplate-assembled microflowers and their visible-light photocatalytic activities, CrystEngComm, 13 (2011) 3035-3039.

[110] T. Shen, C. Jiang, C. Wang, J. Sun, X. Wang, X. Li, A TiO 2 modified abiotic–biotic process for the degradation of the azo dye methyl orange, RSC Advances, 5 (2015) 58704-58712.

[111] K. Dai, H. Chen, T. Peng, D. Ke, H. Yi, Photocatalytic degradation of methyl orange in aqueous suspension of mesoporous titania nanoparticles, Chemosphere, 69 (2007) 1361-1367.

[112] T. Healy, P. Somasundaran, D. Fuerstenau, The adsorption of alkyl and alkylbenzene sulfonates at mineral oxide–water interfaces, Int. J. Miner. Process., 72 (2003) 3-10.

[113] S. Paria, K.C. Khilar, A review on experimental studies of surfactant adsorption at the hydrophilic solid–water interface, Adv. Colloid Interface Sci., 110 (2004) 75-95.

[114] T.S. Natarajan, M. Thomas, K. Natarajan, H.C. Bajaj, R.J. Tayade, Study on UV-LED/TiO2 process for degradation of Rhodamine B dye, Chem. Eng. J., 169 (2011) 126-134.

[115] K. Yu, S. Yang, H. He, C. Sun, C. Gu, Y. Ju, Visible light-driven photocatalytic degradation of rhodamine B over NaBiO3: pathways and mechanism, J. Phys. Chem. A, 113 (2009) 10024-10032.

[116] K.D. Dobson, A.J. McQuillan, In situ infrared spectroscopic analysis of the adsorption of aromatic carboxylic acids to TiO2, ZrO2, Al2O3, and Ta2O5 from aqueous solutions, Spectrochimica Acta Part A: Molecular and Biomolecular Spectroscopy, 56 (2000) 557-565.

[117] F. Yanfen, H. Yingping, Y. Jing, W. Pan, C. Genwei, Unique ability of BiOBr to decarboxylate D-Glu and D-MeAsp in the photocatalytic degradation of microcystin-LR in water, Environmental science & technology, 45 (2011) 1593-1600.

[118] L. Feng, Z. Zhang, Z. Mai, Y. Ma, B. Liu, L. Jiang, D. Zhu, A super‐hydrophobic and super‐oleophilic coating mesh film for the separation of oil and water, Angew. Chem. Int. Ed., 43 (2004) 2012-2014.

[119] L. Jiang, Z. Tang, K.J. Park-Lee, D.W. Hess, V. Breedveld, Fabrication of non-fluorinated hydrophilic-oleophobic stainless steel mesh for oil-water separation, Sep. Purif. Technol., 184 (2017) 394-403.

[120] N. Wen, X. Miao, X. Yang, M. Long, W. Deng, Q. Zhou, W. Deng, An alternative fabrication of underoil superhydrophobic or underwater superoleophobic stainless steel meshes for oil-water separation: Originating from one-step vapor deposition of polydimethylsiloxane, Sep. Purif. Technol., 204 (2018) 116-126.

[121] Y. Yu, H. Chen, Y. Liu, V. Craig, L.H. Li, Y. Chen, Superhydrophobic and Superoleophilic Boron Nitride Nanotube‐Coated Stainless Steel Meshes for Oil and Water Separation, Advanced Materials Interfaces, 1 (2014) 1300002.

[122] J. Song, S. Huang, Y. Lu, X. Bu, J.E. Mates, A. Ghosh, R. Ganguly, C.J. Carmalt, I.P. Parkin, W. Xu, Self-driven one-step oil removal from oil spill on water via selective-wettability steel mesh, ACS Appl. Mater. Interfaces, 6 (2014) 19858-19865.

[123] Y. Dong, J. Li, L. Shi, X. Wang, Z. Guo, W. Liu, Underwater superoleophobic graphene oxide coated meshes for the separation of oil and water, Chem. Commun., 50 (2014) 5586-5589.

[124] B.Y.L. Tan, M.H. Tai, J. Juay, Z. Liu, D. Sun, A study on the performance of self-cleaning oil–water separation membrane formed by various TiO2 nanostructures, Sep. Purif. Technol., 156 (2015) 942-951.

[125] J. Han, W. Qiu, W. Gao, Potential dissolution and photo-dissolution of ZnO thin films, J. Hazard. Mater., 178 (2010) 115-122.

[126] T. Nonoyama, T. Kinoshita, M. Higuchi, K. Nagata, M. Tanaka, K. Sato, K. Kato, TiO2 synthesis inspired by biomineralization: control of morphology, crystal phase, and light-use efficiency in a single process, J. Am. Chem. Soc., 134 (2012) 8841-8847.

[127] W.J. Lee, J.M. Lee, S.T. Kochuveedu, T.H. Han, H.Y. Jeong, M. Park, J.M. Yun, J. Kwon, K. No, D.H. Kim, S.O. Kim, Biomineralized N-Doped CNT/TiO2 Core/Shell Nanowires for Visible Light Photocatalysis, ACS Nano, 6 (2012) 935-943.

[128] C. Liu, D. Yang, Y. Jiao, Y. Tian, Y. Wang, Z. Jiang, Biomimetic Synthesis of TiO2–SiO2–Ag Nanocomposites with Enhanced Visible-Light Photocatalytic Activity, ACS Appl. Mater. Interfaces, 5 (2013) 3824-3832.

[129] Z. Tong, D. Yang, T. Xiao, Y. Tian, Z. Jiang, Biomimetic fabrication of g-C3N4/TiO2 nanosheets with enhanced photocatalytic activity toward organic pollutant degradation, Chem. Eng. J., 260 (2015) 117-125.

[130] Y. Jiang, D. Yang, L. Zhang, Q. Sun, X. Sun, J. Li, Z. Jiang, Preparation of Protamine–Titania Microcapsules Through Synergy Between Layer‐by‐Layer Assembly and Biomimetic Mineralization, Adv. Funct. Mater., 19 (2009) 150-156.

[131] X. Wang, Y. Yan, B. Hao, G. Chen, Protein-mediated layer-by-layer synthesis of TiO2 (B)/anatase/carbon coating on nickel foam as negative electrode material for lithium-ion battery, ACS Appl. Mater. Interfaces, 5 (2013) 3631-3637.

[132] J.D. Berrigan, T.S. Kang, Y. Cai, J.R. Deneault, M.F. Durstock, K.H. Sandhage, Protein‐Enabled Layer‐by‐Layer Syntheses of Aligned, Porous‐Wall, High‐Aspect‐Ratio TiO2 Nanotube Arrays, Adv. Funct. Mater., 21 (2011) 1693-1700.

[133] B. Hao, Y. Yan, X. Wang, G. Chen, Biomimetic layer-by-layer Co-mineralization approach towards TiO 2/Au nanosheets with high rate performance for lithium ion batteries, Nanoscale, 5 (2013) 10472-10480.

[134] G. Chen, M. Li, F. Li, S. Sun, D. Xia, Protein‐Mediated Synthesis of Nanostructured Titania with Different Polymorphs at Room Temperature, Adv. Mater., 22 (2010) 1258-1262.

[135] Y. Fang, Q. Wu, M.B. Dickerson, Y. Cai, S. Shian, J.D. Berrigan, N. Poulsen, N. Kroger, K.H. Sandhage, Protein-mediated layer-by-layer syntheses of freestanding microscale titania structures with biologically assembled 3-D morphologies, Chem. Mater., 21 (2009) 5704-5710.

[136] N.R. Haase, S. Shian, K.H. Sandhage, N. Kröger, Biocatalytic nanoscale coatings through biomimetic layer‐by‐layer mineralization, Adv. Funct. Mater., 21 (2011) 4243-4251.

[137] A.F. Stalder, T. Melchior, M. Müller, D. Sage, T. Blu, M. Unser, Low-bond axisymmetric drop shape analysis for surface tension and contact angle measurements of sessile drops, Colloids and Surfaces A: Physicochemical and Engineering Aspects, 364 (2010) 72-81.

[138] F. Zhao, E. Repo, Y. Song, D. Yin, S.B. Hammouda, L. Chen, S. Kalliola, J. Tang, K.C. Tam, M. Sillanpää, Polyethylenimine-cross-linked cellulose nanocrystals for highly efficient

recovery of rare earth elements from water and a mechanism study, Green Chemistry, 19 (2017) 4816-4828.

[139] M. Min, L. Shen, G. Hong, M. Zhu, Y. Zhang, X. Wang, Y. Chen, B.S. Hsiao, Micro-nano structure poly (ether sulfones)/poly (ethyleneimine) nanofibrous affinity membranes for adsorption of anionic dyes and heavy metal ions in aqueous solution, Chem. Eng. J., 197 (2012) 88-100.

[140] N. McIntyre, D. Zetaruk, X-ray photoelectron spectroscopic studies of iron oxides, Anal. Chem., 49 (1977) 1521-1529.

[141] A. Wassilkowska, A. Czaplicka-Kotas, A. Bielski, M. Zielina, An analysis of the elemental composition of micro-samples using EDS technique, Czasopismo Techniczne, 2014 (2015) 133-148.

[142] Y. Jiang, D. Yang, L. Zhang, L. Li, Q. Sun, Y. Zhang, J. Li, Z. Jiang, Biomimetic synthesis of titania nanoparticles induced by protamine, Dalton Transactions, (2008) 4165-4171.

[143] Z. Tong, Y. Jiang, D. Yang, J. Shi, S. Zhang, C. Liu, Z. Jiang, Biomimetic and bioinspired synthesis of titania and titania-based materials, RSC Advances, 4 (2014) 12388-12403.

[144] A. Hai, A.A. Durrani, M. Selvaraj, F. Banat, M.A. Haija, Oil-water emulsion separation using intrinsically superoleophilic and superhydrophobic PVDF membrane, Sep. Purif. Technol., 212 (2019) 388-395.

[145] H. Kang, Z. Cheng, H. Lai, H. Ma, Y. Liu, X. Mai, Y. Wang, Q. Shao, L. Xiang, X. Guo, Z. Guo, Superlyophobic anti-corrosive and self-cleaning titania robust mesh membrane with enhanced oil/water separation, Sep. Purif. Technol., 201 (2018) 193-204.

[146] R. Liu, S. Dangwal, I. Shaik, C. Aichele, S.-J. Kim, Hydrophilicity-controlled MFI-type zeolite-coated mesh for oil/water separation, Sep. Purif. Technol., 195 (2018) 163-169.

[147] R.N. Wenzel, Resistance of solid surfaces to wetting by water, Industrial & Engineering Chemistry, 28 (1936) 988-994.

[148] A. Cassie, S. Baxter, Wettability of porous surfaces, Transactions of the Faraday society, 40 (1944) 546-551.

[149] T. Yuan, J. Meng, T. Hao, Z. Wang, Y. Zhang, A scalable method toward superhydrophilic and underwater superoleophobic PVDF membranes for effective oil/water emulsion separation, ACS Appl. Mater. Interfaces, 7 (2015) 14896-14904.

[150] H. Shi, Y. He, Y. Pan, H. Di, G. Zeng, L. Zhang, C. Zhang, A modified mussel-inspired method to fabricate TiO2 decorated superhydrophilic PVDF membrane for oil/water separation, Journal of membrane science, 506 (2016) 60-70.

[151] R.A. Damodar, S.-J. You, H.-H. Chou, Study the self cleaning, antibacterial and photocatalytic properties of TiO2 entrapped PVDF membranes, J. Hazard. Mater., 172 (2009) 1321-1328.

[152] A. Rahimpour, M. Jahanshahi, B. Rajaeian, M. Rahimnejad, TiO2 entrapped nano-composite PVDF/SPES membranes: Preparation, characterization, antifouling and antibacterial properties, Desalination, 278 (2011) 343-353.

[153] S.J. Oh, N. Kim, Y.T. Lee, Preparation and characterization of PVDF/TiO2 organic–inorganic composite membranes for fouling resistance improvement, Journal of Membrane Science, 345 (2009) 13-20.

[154] L. Li, Z. Liu, Q. Zhang, C. Meng, T. Zhang, J. Zhai, Underwater superoleophobic porous membrane based on hierarchical TiO 2 nanotubes: multifunctional integration of oil–water separation, flow-through photocatalysis and self-cleaning, J. Mater. Chem. A, 3 (2015) 1279-1286.

[155] Y. Liu, Y. Su, J. Guan, J. Cao, R. Zhang, M. He, K. Gao, L. Zhou, Z. Jiang, 2D Heterostructure Membranes with Sunlight‐Driven Self‐Cleaning Ability for Highly Efficient Oil–Water Separation, Adv. Funct. Mater., 28 (2018) 1706545.